ALL-FIBER MODE-LOCKED ULTRAFAST THULIUM-DOPED FIBER LASERS AT $2\mu m$

by

QingQing Wang

B.S., Physics, University of Science and Technology of China, 2005

M.S., Physics, University of Pittsburgh, 2008

Submitted to the Graduate Faculty of

the Department of Electrical and Computer Engineering

Swanson School of Engineering in partial fulfillment

of the requirements for the degree of

Doctor of Philosophy

University of Pittsburgh

2014

UNIVERSITY OF PITTSBURGH

SWANSON SCHOOL OF ENGINEERING

This dissertation was presented

by

QingQing Wang

It was defended on

July 16 2014

and approved by

Kevin P. Chen, Ph.D., Associate Professor,

Department of Electrical and Computer Engineering

William Stanchina, Ph.D., Professor,

Department of Electrical and Computer Engineering

Mahmoud El Nokali, Ph.D., Associate Professor,

Department of Electrical and Computer Engineering

Guangyong Li, Ph.D., Associate Professor,

Department of Electrical and Computer Engineering

Karl Harris, Ph.D.,

Penn State Electro-Optics Center

Dissertation Director: Kevin P. Chen, Ph.D., Associate Professor,

Department of Electrical and Computer Engineering

ALL-FIBER MODE-LOCKED ULTRAFAST THULIUM-DOPED FIBER LASERS AT $2\mu m$

QingQing Wang, PhD

University of Pittsburgh, 2014

In this work, we demonstrate three original all-fiber ring configurations of passively mode-locked Thulium-doped fiber(TDF) lasers operated around $2\mu m$ wavelength for which the usage of free-space optics components is minimized. Different mode-locking techniques/materials e.g. nonlinear polarization evolution (NPE), graphene-based saturable asbsorbers(GSAs) and single-wall carbon nanotubes (SWCNTs) are developed and used to passively mode lock TDF laser and produce ultrashort pulses at $2\mu m$. Also to achieve higher pulse energy directly from a fiber oscillator, the net intra-cavity dispersion is managed by the introducing of normal dispersion fiber(NDF) at $2\mu m$ into the fiber cavity. Both the sign and amount of the net cavity dispersion can be controlled without compromising the merits of all-fiber configuration. Distinctive ultrashort pulses of different pulse shapes and per-pulse energies e.g. solitons, noise-like pulses and dissipative solitons are produced from these fiber lasers for which the generated pulses' features and dynamics are experimentally investigated and characterized. A computational model is built to simulate these mode-locked TDF lasers by numerically solving the Nonlinear Schrődinger Equations(NLSE).

TABLE OF CONTENTS

LIST OF TABLES

LIST OF FIGURES

PREFACE

I am very grateful to all the people who had given me supports and inspirations during my PhD study. Without the help and support from them, this dissertation would not have be possible.

First and foremost, I want to express my sincere gratitude to my PhD advisor, Professor Kevin P. Chen for his continuous support, insightful advisory and inspirational motivation. All the time, efforts, ideas, and fund he has spent to make my PhD experience fruitful are highly appreciated.

I also want to thank my family, especially my wife, Wenting. Her years' support, encouragement and sacrifice help me conquer challenges in the study and the life.

I want to thank my lab mates and all the friends I had made in Pittsburgh, for all the happy and tough times we spent together. Please forgive me as I cannot list all their names here.

Finally, thanks to my committee members, Prof. William Stanchina, Prof. Mahmoud El Nokali, Prof.Guangyong Li, and Dr Karl Harris for being kind inquisitors, thorough readers and all the suggestions and outputs about thesis writing and organization.

1.0 INTRODUCTION

Shortly after Th. Maiman invented the first working laser in 1960s[5], scientists demonstrated that very short optical pulses ($< 1ns$) could be generated using laser cavity mode locking processes. Since then this research field of ultrafast lasers has drawn extensive interests. So far various mode locking techniques have been developed over the years, such as Kerr Lens Mode-locking(KLM), NPE and different saturable absorbers(SAs) that enable the generation of ultrashort pulse laser systems with various outputs. Meanwhile ultrafast pulse lasers have also allowed us a powerful tool to directly observe some of the fastest processes in nature and closely study matters under extreme physical conditions. Upto now two Nobel prizes have been rewarded to ultrafast optics related researches: the observation of molecules' transition states[6]and optical frequency combs for metrology[7]. Nevertheless, ultrafast lasers and techniques do not only stay in laboratory but also have also found their roles in many industrial areas, for example precision laser machining [8, 9, 10], optical sensing [11, 12] and medical surgeries[12, 13].

Of various forms of mode-locked laser systems, mode-locked fiber laser has a place and shows many exclusive advantages over the other forms of lasers. The use of optical fiber as the laser medium enables laser system designs that are compact, more rugged and of lower cost as compared with mode-locked dye laser and solid state laser systems. With the advent of optical fiber, mode-locking of laser light within fiber promised compact, low cost ultrashort pulse laser laser system designs and as a result, been the subject of much research over the last 15 years. As new specialty optical fiber becomes available, research and development to apply that fiber for new wavelengths is required to develop new ultrafast fiber laser with wavelength outputs capable for new or improved industrial and medical applications e.g. TDF laser with emission at $1.93\mu m$.

1.1 MODE-LOCKED FIBER LASERS

Solid-state and dye lasers with continuous wave(CW), Q-switched or mode-locked pulsed output have been widely used in industrial and research areas. Nowadays solid-state and dye lasers are still the preferred choice and dominating in many applications in term of their merits such as maturity, long-term stability and high output power. However these lasers also have shown their limitations, for example most of solid-state and dye lasers are bulky in size, need precise alignment/realignment and require stable operational environments which strictly limit their use for occasions where more-compact, user-friendly, and field-rugged laser system are needed.

Optical fiber systems rely on the principal of total internal reflection for which light is confined and propagated in the fiber's core area where the refractive index is slightly higher than that of the surrounding cladding layer. Motivated by the needs from the communication industry, low loss silica-hosted and other specialty fibers have been available and the fabrication of these fibers has become a mature technology[14], which significantly extends fiber's applications for which fiber laser is one of them. Fiber laser is a laser system that deploys an optical fiber doped with rare-earth elements as the active gain medium. For different dopants and host materials, fiber laser amplifiers can operate at various wavelengths, for example $1.06\mu m$ from ytterbium in silica, $1.3\mu m$ from praseodymium in silicon fluoride, $1.5\mu m$ from erbium in silica and $1.95\mu m$ from thulium in silica. Usually the amplification bandwidth of these rare earth doped fibers is broad, varying from tens of nanometers to several hundred nanometers, which makes them great gain media for broad bandwidth ultrashort pulse generation via mode locking at various wavelengths. So far different mode-locking techniques like NPE, semiconductor saturable absorber mirrors(SESAMs), GSAs and SWCNTs have been successfully applied and passively mode-locked fiber lasers for short pulse generation[15, 3]. These fiber systems offer many desired advantages that the bulk solid-state systems and other forms of lasers do not take, as they are more compact, economical in cost and require minimal maintenance. Moreover, the guiding property of fiber systems allows us to easily integrate fiber lasers with many in-fiber devices e.g. fiber gratings and fiber couplers and minimize the usage of bulk optic components which makes them more

attractive. Also fiber lasers can deliver excellent beam quality, and it has been shown that based on single-mode fibers, the output beam quality can closely approach that value of a diffraction-limited Gaussian beam($M^2 = 1$).

However common mode-locked fiber laser systems still trail behind the solid-state systems if taking a look at some key performance parameters e.g. pulse energy, pulse duration, pulse jittering and peak power, which are mainly due to the excessive unwanted nonlinearity accumulated as light propagates in fiber. Very recently, combining with the progress of high power pump diodes, the development of large mode area(LMA) and photonic crystal fibers(PCFs) and the involvement of intra-cavity dispersion and nonlinearity control technology, mode-locked fiber lasers are able to produce short pulses with pulse energy on par with that of those solid-state lasers [16, 17]. Thus for the fist time, high power mode-locked fiber lasers draw more-than-ever practical interests from both research and industrial fields.

1.2 $2\mu m$ LIGHT SOURCES

Different applications need different lasers operated with different output wavelength. Partiularly, laser lights with wavelength around $2\mu m$ are of great practical importance for many applications. For example, $2\mu m$ wavelength is within the "eye-safe" windows. Light around $2\mu m$ will be strongly absorbed in the vitreous humor and can hardly reach and harm the retina. So these $2\mu m$ laser systems are ideal for applications in Light Detection and Ranging(LIDAR) systems where eye safety is of much concern. Also many atmospheric gasses (e.g. CO_2,H_2O,NH_3,N_2O) exhibit characteristic absorption lines around $2\mu m$, so $2\mu m$ lasers are valuable for high-resolution chemical sensing and gas detection. Moreover, $2\mu m$ lasers also find their roles in many medical applications. For example, due to $2\mu m$'s high absorption in water and the resulted minimal penetration in human tissues, $2\mu m$ lasers have been widely employed for precise laser surgery and cell ablation [18, 19].

Various forms of lasers exist with radiation wavelength around $2\mu m$. The most commonly used lasing media at $2\mu m$ are GsSb-based semiconductors, Tm^{3+} and/or Ho^{3+} doped crystals(e.g. Ho:YLF, Tm:YAG), and Tm^{3+} and/or Ho^{3+} doped silica fibers. Pulsed out-

puts by mode-locking and Q-switching have also been produced and reported from these laser systems[20, 21, 22, 23, 24]. In addition, ultrashort pulsed light around $2\mu m$ can also be indirectly produced via nonlinear conversions from optical parametric oscillator and supercontinuum generation with mode-locked high power Ti:Sapphire or Erbium-doped fiber laser as the pump light. If a comparison is made between these $2\mu m$lasers as listed above, we might easily find TDF lasers have many advantages over the others. For example, the Tm^{3+} ions in hosts like silica can be directly excited with the maturely developed EDFAs at $1.55\mu m$ in order to preserve an all-fiber configuration. The fiber lasers also yield a better beam quality than the crystal ones and the gain bandwidth is smooth and broad ($\sim 200nm$ Tm in silica), which makes TDF even more attractive for mode-locked short pulse generation.

1.3 ORGANIZATION OF THESIS

The rest of the thesis is organized as follows. Chapter 2 is to introduce some main properties of optical fibers like dispersion and nonlinearity; and the methods and results we used for fiber dispersion measurement are also going to be shown in this chapter. Chapter 3 is the computational modeling and numerical simulation of mode-locked fiber laser. Chapters 4, 5 and 6 include the experimental realizations and results of mode-locked TDF lasers by NPE, optically deposited GSA and SWCNTs SA, which are divided into several sections. Comparison with the numerical simulation is also going to be included. Chapter 7 is the conclusion and the overlook for future work. The last part of this thesis lists the appendices.

2.0 PROPERTIES OF OPTICAL FIBERS

Optical fibers function as light waveguide. Based on the total internal reflection principal, light wave is tightly confined in the fiber's core area and transmitted between fiber's two ends whose refractive index is slightly greater than that of the surrounding cladding medium. In 1965, Charles K. Kao and George A. Hockham firstly proposed the idea that the attenuation in optical fibers could be reduced below $20dB/km$, and made fibers a practical medium for long distance communication and many other applications[25]. Today optical fibers with low transmittance loss e.g. $< 0.2dB/km$ can be mass-produced by using maturely developed manufacturing processes and these fibers have been widely applied into communication and many other related fields.

This chapter talks about the behaviors of $2\mu m$ light when traveling in single mode silica fiber. As light is confined and propagating in fiber, some characteristic properties of the fibers at $2\mu m$ such as dispersion and nonlinearity, need to be addressed with priority as for $2\mu m$ thulium fiber laser building. The upcoming sections are going to introduce some characteristic parameters of optical fibers e.g. dispersion, nonlinearity, birefringence, etc and demonstrate the methods we utilized to characterize and evaluate these parameters at $2\mu m$. The absorption and emission properties of different rare-earth doped active gain fibers are also going to be covered.

2.1 PASSIVE SINGLE MODE FIBER

Optical fibers are the fundamental elements for the building of fiber lasers. Figure 2.1 is the scheme of step-index fiber, which consists of fiber core at the center surrounded by the

cladding layer. The refractive index of the fiber core is normally slightly higher than that of the surrounding cladding, so based on the principal of total internal reflection, light can be majorly confined in the core area and propagate along the fiber. Two important parameters are commonly used to characterize the step-index fiber: one is numerical aperture(NA) as defined in Equation 2.1

$$\mathrm{NA} \equiv \sqrt{n_{core}^2 - n_{clad}^2} \tag{2.1}$$

where n_{core} and n_{clad} are the refractive indices of the core and cladding respectively; the other parameter is called V number defined as

$$\mathrm{V} \equiv k_0 a \sqrt{n_{core}^2 - n_{clad}^2} = k_0 a \mathrm{NA} \tag{2.2}$$

where $k_0 = 2\pi/\lambda$, λ is the wavelength and a is the core radius. When $\mathrm{V} < 2.405$, the single mode condition is satisfied and only one transverse mode(LP_{01} mode) can be supported in fiber, and the fiber is called single mode fiber. We might notice the single mode condition actually depends on the light's wavelength as the expression of V number contains wavelength λ in the denominator. For a specifically designed step-index fiber whose NA and core radius are decided, there is a wavelength λ_{cutoff} for which $\mathrm{V} = 2.405$, and this wavelength λ_{cutoff} is so-called cutoff wavelength. Above this wavelength($\lambda > \lambda_{cutoff}$), only one transverse mode can be supported in fiber while a few transverse modes exist if the transmitted light's wavelength is smaller than the cutoff wavelength. The effective index n_{eff} that the confined light experiences when traveling in the fiber is in between n_{core} and n_{clad}($n_{clad} < n_{eff} < n_{core}$), which depends the used materials for fiber fabrication and the index profile of the fiber.

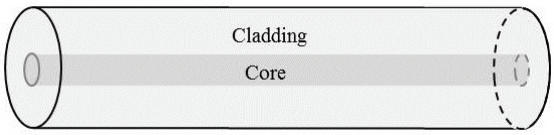

Figure 2.1: Schematic illustration of step-index fiber(false scale).

Motivated by the needs from the modern communication industry, nowadays low loss silica-hosted and other specialty fibers have been commercially available and the fabrication of these fibers has become a mature technology, for example the loss of the most common single mode fiber today is $\sim 0.2 dB/km$ at the widely used $1.55\mu m$ telecommunication band and the OH-ion absorption and Rayleigh scattering resulted from the fabrication impurity and glass density fluctuation are considered as two major contributors to this loss[26].

Besides transmittance loss, dispersions and nonlinearity of the constructing fibers also play important roles in the operation of mode-locked fiber lasers. These dispersions include chromatic dispersion and polarization-mode dispersion. For the design of mode-locked fiber lasers, knowledge and information about the dispersions and nonlinearity of the constructing fibers are very necessary. However at TDF fiber laser $2\mu m$ emission band, these important parameters for most commercially available fibers are either unknown or not released by the manufacturers because $2\mu m$ band is yet relatively new compared with other bands like $1.06\mu m$, $1.3\mu m$ and $1.55\mu m$. So there is a need to address methods and set up experiments to measure and characterize these parameters at $2\mu m$.

2.1.1 Chromatic dispersion of single-mode fiber

When light travels in single-mode fibers or actually any other kind of waveguide, light components of different frequencies might interact differently with the surrounding optical medium. This property is referred as the medium's chromatic dispersion and manifests through the fact that medium's effective refractive index n_{eff} varies as a function $n(\omega)$ about light frequency ω. Or simple to say, light of different wavelengths travels with different velocity $c/n(\lambda)$ and c is the speed of light in vacuum. Mathematically for a wavelength dispersive single-mode fiber, the propagation constant β can be approximated by expanding in Tayler series about the center frequency ω_0 as the following:

$$\beta(\omega) \equiv n_{eff}(\omega)\frac{\omega}{c} = \beta_0 + \beta_1(\omega-\omega_0) + \frac{1}{2}\beta_2(\omega-\omega_0)^2 + \frac{1}{6}\beta_3(\omega-\omega_0)^3 + \cdots \tag{2.3}$$

where

$$\beta_m = (\frac{\mathrm{d}^m\beta}{\mathrm{d}\omega^m})_{\omega=\omega_0} \quad (m = 0, 1, 2, \ldots) \tag{2.4}$$

Particularly, the first three coefficients of the Taylor expansion can be expressed in terms of the fiber's effective refractive index and its derivatives about frequency ω as

$$\beta_1 = \frac{1}{v_g} = \frac{n_g}{c} = \frac{1}{c}(n + \omega\frac{\mathrm{d}n}{\mathrm{d}\omega})_{\omega=\omega_0} \tag{2.5}$$

$$\beta_2 = \frac{1}{c}(2\frac{\mathrm{d}n}{\mathrm{d}\omega} + \omega\frac{\mathrm{d}^2n}{\mathrm{d}\omega^2})_{\omega=\omega_0} \tag{2.6}$$

$$\beta_3 = \frac{1}{c}(3\frac{\mathrm{d}^2n}{\mathrm{d}\omega^2} + \omega\frac{\mathrm{d}^3n}{\mathrm{d}\omega^3})_{\omega=\omega_0} \tag{2.7}$$

Like demonstrated, β_1 is the inverse of the group velocity that is the speed the pulse or wave pocket moves with in the fiber and n_g is called group index. β_2 as the derivative of β_1 about frequency ω is termed as the ground velocity dispersion(GVD) or second order dispersion which is responsible for the pulse broadening in time domain while light propagates in fiber and β_3 is called third order dispersion(TOD). The GVD parameter β_2 is usually given in unit of ps^2/km. Conventionally the second order dispersion is simply called dispersion for short. In this thesis, dispersion means second order dispresion/GVD if no order is specified. Another commonly used measure of GVD parameter D is defined as $\mathrm{d}\beta_1/\mathrm{d}\lambda$, of unit $ps/nm/km$ and the relation of these two different measures of β_2 are

$$\mathrm{D} = \frac{\mathrm{d}\beta_1}{\mathrm{d}\lambda} = -\frac{2\pi c}{\lambda^2}\beta_2 = -\frac{\lambda}{c}\frac{\mathrm{d}^2n}{\mathrm{d}\lambda^2} \tag{2.8}$$

For a single-mode fiber, if its chromatic dispersion GVD β_2 is greater than zero (D is negative), we say this fiber takes normal dispersion, for which light of longer wavelength travels faster than light of shorter wavelength in the fiber(e.g. red light travels faster than the blue light). If β_2 is negative (D is positive), the fiber takes anomalous dispersion. Fiber's dispersion is very important for the design of mode-locked fiber laser, as it decides pulse's evolution and broadening during its propagation even under circumstances when the pulse intensity is small and the nonlinear effects are not significant.

For single-mode fiber, its effective refractive index n_{eff} mainly depends the used fabrication materials and fiber's geometry which includes fiber's index profile and contrast. As

a result, fiber's chromatic GVD can be deduced and considered as the sum of two terms: material's chromatic dispersion and designed waveguide chromatic dispersion [27].

For the material GVD part, the refractive index $n(\omega)$ can be well approximated by the *Sellmeier equation* [28]

$$n^2(\omega) = 1 + \sum_{j=1}^{m} \frac{B_j \lambda^2}{\lambda^2 - C_j^2} \approx 1 + \frac{B_1 \lambda^2}{\lambda^2 - C_1^2} + \frac{B_2 \lambda^2}{\lambda^2 - C_2^2} + \frac{B_3 \lambda^2}{\lambda^2 - C_3^2} \tag{2.9}$$

For un-doped fused bulk silica, $B_1 = 0.6961663$, $B_2 = 0.4079426$, $B_3 = 0.8974794$, $C_1 = 0.0684043$, $C_2 = 0.1162414$ and $C_3 = 9.896161$, where the wavelength λ is in micrometers.

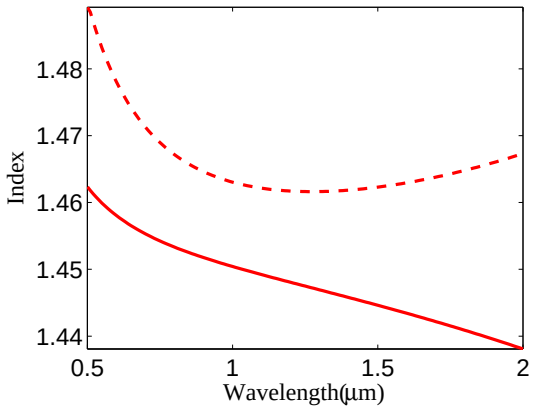

Figure 2.2: Refractive index n(solid) and group index n_g(dashed) versus wavelength for fused silica.

Figure 2.2 shows refractive index and group index of un-doped fused silica versus wavelength from 0.5 to $2\mu m$. Figure 2.3 is the plot of the material GVD versus wavelength from 1.1 to $2\mu m$ for un-doped fused silica. The material's zero dispersion is located around $1.27\mu m$, and at $1.9\mu m$ the material's dispersion is anomalous and its value is about -87ps^2/km. During the process of fabrication, fiber core area is added with dopant ions like Germanium in order to increase its refractive index, and this results the fiber's material chromatic GVD curve to slightly shift toward the longer wavelength and alters its zero dispersion wavelength(ZDW) to $1.3\mu m$.

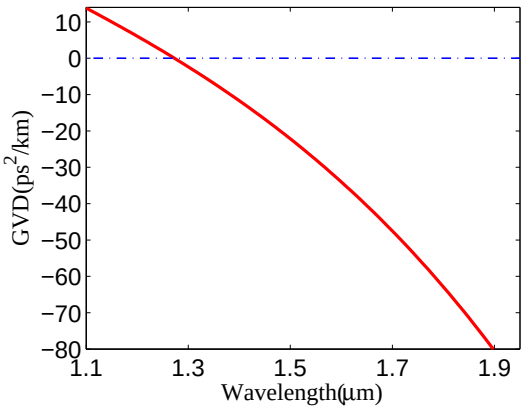

Figure 2.3: Material dispersion(GVD) versus wavelength for fused silica.

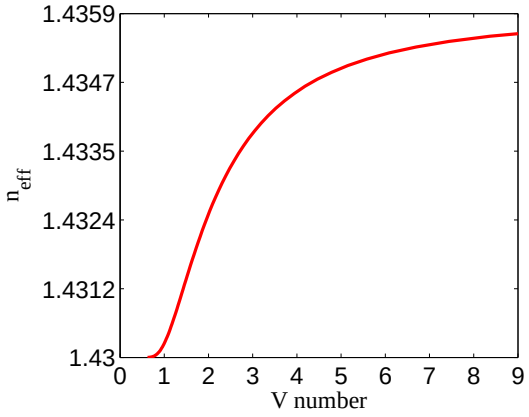

Figure 2.4: Effective refractive index as function of V number at the LP_{01} mode. The fiber parameters are $a = 4.1\mu m, \text{NA} = 0.13$.

Besides material dispersion, another major contributor to fiber's chromatic GVD is waveguide dispersion. For step index single mode fiber, waveguide dispersion becomes significant if fiber has small core size (e.g. $a < 3\mu m$) and large index contrast between the core and cladding(e.g. $\triangle n > 0.01$). Figure 2.4 shows the waveguide effective index versus the V number for a standard step-index single mode fiber with core size $a = 4.1\mu m$ and NA $= 0.13$ at the fundamental LP_{01} mode by solving the field equations[29], where we assume the fiber is

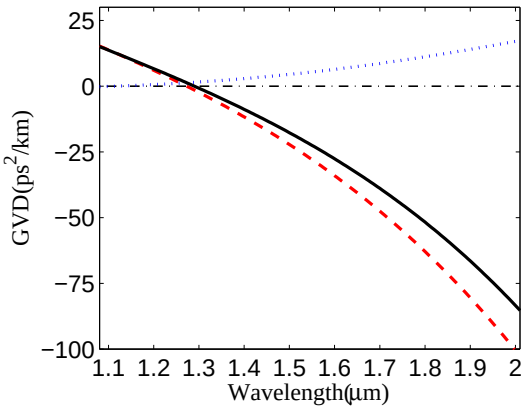

Figure 2.5: Fiber total GVD(solid) as the sum of material GVD(dashed) and waveguide GVD(dotted) at the LP_{01} mode. The fiber parameters are $a = 4.1\mu m, \mathrm{NA} = 0.13$.

transmittance loss free at all wavelength. The material dispersion, waveguide dispersion and the total chromatic dispersion as the sum of these two are demonstrated in Figure 2.5. Note the waveguide dispersion is always normal, and it can thus be used to cancel the anomalous GVD from material's one at certain wavelength range. Also it has been reported that by dramatically reducing fiber's core size, increasing the index contrast between fiber's core and cladding areas while preserving the single-mode condition, large normal waveguide dispersion can be generated. By using this fiber design method, the fiber's total chromatic GVD can be engineered and compensated at wavelength where fiber's material GVD is anomalous [30]. In comparison, Figure 2.6 and Figure 2.7 show the waveguide dispersion for two fibers with different diameters and NA and both of them have the single mode cutoff around $1.35\mu m$. It can be seen that by reducing fiber core diameter from $8.2\mu m$ to $2.2\mu m$ and increasing the NA from 0.13 to 0.48, ten times normal dispersion is generated. Discussion will be given in the following chapters that fibers of normal dispersion are of great importance for mode-locked fiber laser, especially for mode-locked fiber laser of large pulse energy.

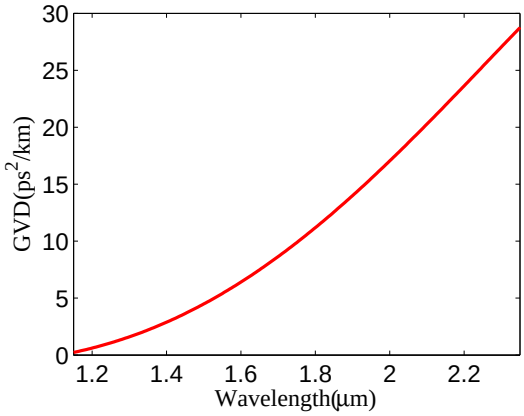

Figure 2.6: Fiber waveguide GVD at the LP_{01} mode. The fiber parameters are $a = 4.1\mu m, \text{NA} = 0.13$.

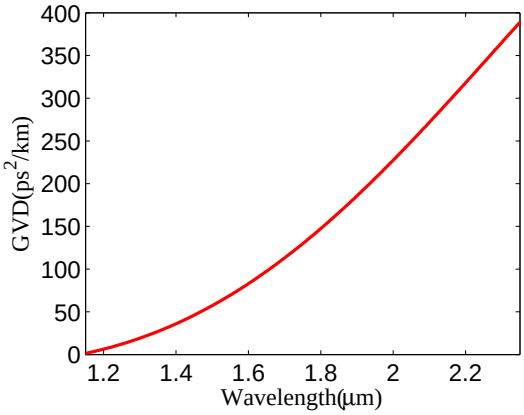

Figure 2.7: Fiber waveguide GVD at the LP_{01} mode. The fiber parameters are $a = 1.1\mu m, \text{NA} = 0.48$.

2.1.2 Chromatic dispersion measurement

Various methods and techniques have been developed for waveguide and fiber GVD measurement that include time-of-flight method, deferential phase shift measurement, white-light interferometry and mode-field-diameter measurement[31]. However, some of these methods are not practically applicable for fiber GVD measurement at $2\mu m$ wavelength, which is ei-

ther because the desired light source is not available or the cost of the required optical characterization components are still prohibitive for most research groups.

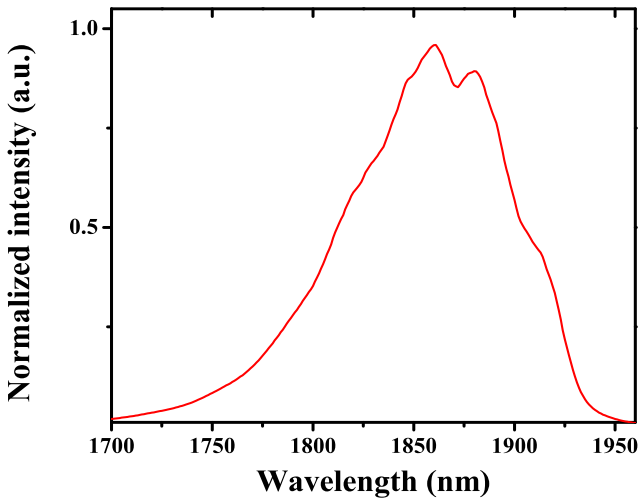

Figure 2.8: Broadband spontaneous emission of TDF.

To effectively measure fiber GVD around $2\mu m$ wavelength with adequate accuracy, we employ a white-light interferometric method for which the broadband spontaneous emission from TDF pumped by $1550nm$ EDFA is used as the white-light source. Figure 2.8 shows the wide spontaneous emission spectrum from TDF, which starts from $1.7\mu m$ and ends around $2\mu m$.

Figure 2.9 schemes the measurement setup. A 3-dB 2×2 fiber coupler of equal-length pigtails serves as a beam splitter which evenly split the incident light into two arms. One arm of the interferometer is free space while the other is the fiber under test (FUT). And both arms are terminated with broadband end mirrors. FUT can be either butt coupled or fusion spliced to the coupler's FUT arm. When white light is launched into the interferometer through one port of the coupler, various wavelength components of the light will experience different time delays as they propagate through the FUT due to the chromatic dispersion of the FUT, and interference fringes are produced as they come back and recombine with the reflected light from the free space arm at the coupler again. The caused interference

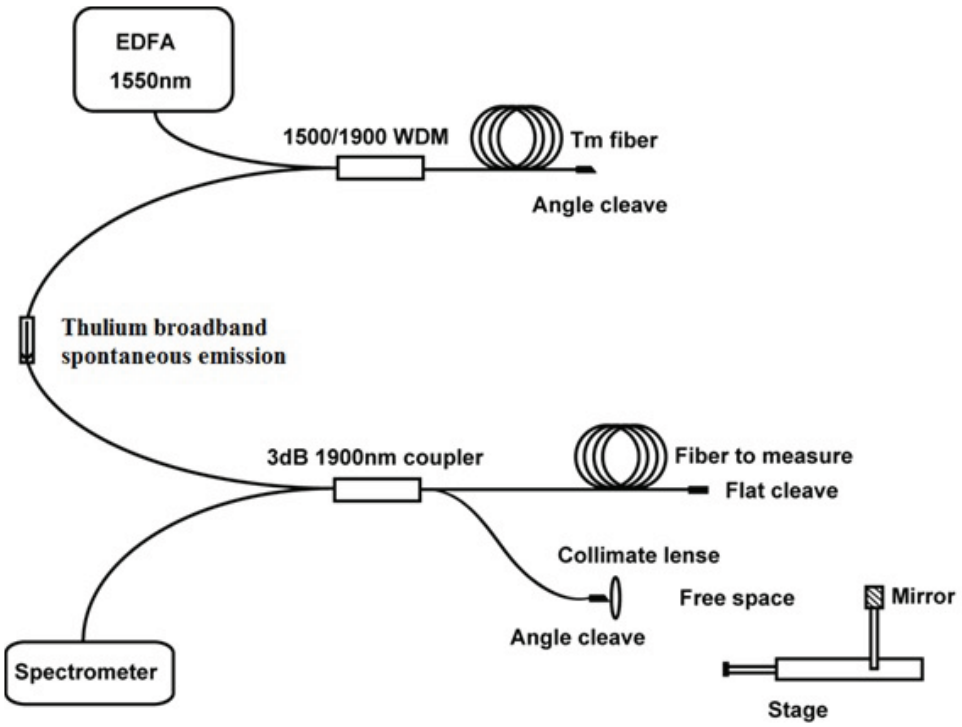

Figure 2.9: Scheme of setup for fiber dispersion measurement at $1.9\mu m$.

fringes are registered by a spectrometer placed after the monitoring port. The spectrum of the recombined beam can be written as

$$I(\omega) = |E_{air} + E_{FUT}|^2 \sim 1 + \cos\phi(\omega) \tag{2.10}$$

where E_{air} and E_{FUT} present the electric fields of the free space arm and the FUT arm respectively and $\phi(\omega)$ is the phase difference of these two reflected fields as the two arms recombine. $\phi(\omega)$ can be expanded as

$$\begin{aligned}\phi(\omega) = \phi_0 + (\beta_1(\omega_0)L_{FUT} - \frac{L_{air}}{c})(\frac{2\pi c}{\lambda} - \frac{2\pi c}{\lambda_0}) \\ + \frac{1}{2}\beta_2(\omega_0)L_{FUT}(\frac{2\pi c}{\lambda} - \frac{2\pi c}{\lambda_0})^2 + \frac{1}{6}\beta_3(\omega_0)L_{FUT}(\frac{2\pi c}{\lambda} - \frac{2\pi c}{\lambda_0})^3 + \cdots\end{aligned} \tag{2.11}$$

where β_2 and β_3 are the second order and third order dispersion of the FUT and we consider the free space reference arm as non-dispersive. As the incident TDF spontaneous emission

is broad in spectrum and of weak coherence, when the optical lengths of the two arms are matched and equalized, interferometric fringes of the recombined light will be addressed by the monochromator. By fitting the measured spectral interference fringes to Equation 2.11, both the second order and third order dispersion of the FUT can be extracted.

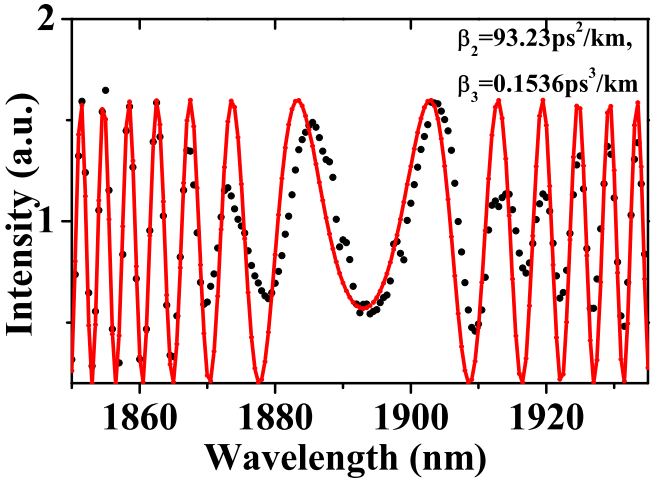

Figure 2.10: Interference fringes for NDF dispersion measurement around $1.9\mu m$. The dots show the measurement data and the solid represents the curve fitting results.

After tremendous search and measurement, a normal dispersion fiber (NDF) around $1.9\mu m$ is identified (NA=0.35, 2.2-μm core diameter). Figure 2.10 shows the measured interference patterns and the fitting results. The sign of FUT's GVD is decided in this way after seeing the interference fringes, if the fringes' center value moves towards longer wavelength as the length of the free space reference arm slightly increases, the FUT takes anomalous GVD; otherwise the GVD is normal. By using the white light interferometric method, the dispersion of NDF is measured to be $\beta_2 = 93ps^2/km$ at $1.9\mu m$ and the 3rd order dispersion coefficient is $\beta_3 = 0.15ps^3/km$ for which $1m$ long FUT in used. In comparison, the dispersion coefficient of single-mode fiber SMF-28e from Corning around $1.9\mu m$ is anomalous and the value is measured as $\beta_2 = -67ps^2/km$ and this value agrees with the reported ones whereas [24]. Figure 2.11 is the interference patterns and the fitting curve for SMF-28e dispersion measurement at $1.9\mu m$.

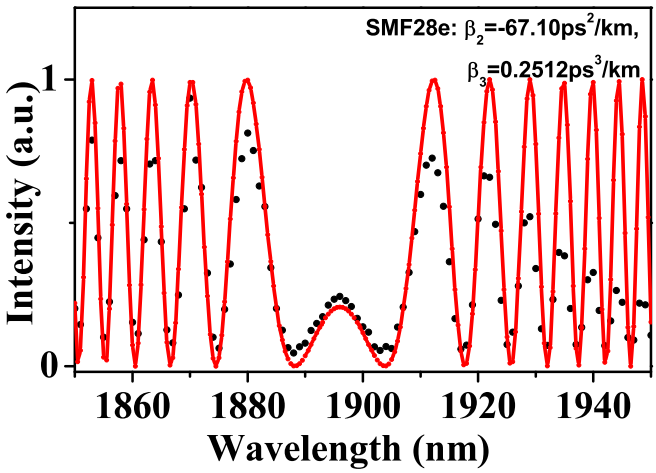

Figure 2.11: Interference fringes for SMF-28e dispersion measurement around $1.9\mu m$. The dots show the measurement data and the solid represents the curve fitting results.

2.1.3 Birefringent dispersion of single-mode fiber

Besides dispersion, another fiber's parameter that needs to be taken into consideration is birefringence. Even for single-mode fiber, there are two degenerate polarization modes that are supported in the fiber. Under ideal condition, for single mode-fiber with perfect cylindrical symmetry and free of stress, these two degenerated modes are of exactly the same propagation constant β and the polarization of incident beam will preserve its polarization state as it travels through the fiber. However for real fibers, these two degenerated polarization states are usually of small different propagation constants as the result of the destructed symmetry of the fiber from the imperfect fabrication process and the significance of this difference highly depends on the extent of the symmetrical destruction. This phenomena, two degenerate polarizations states of different propagation constants in fiber is called fiber birefringence or birefringent dispersion. Fiber birefringence causes light to alter its polarization state as it propagates in fiber.

The strength of fiber birefringence is measured by the refractive index difference between these two degenerate polarization modes:

$$\mathrm{B}_m = |n_x - n_y| = \frac{|\beta_x - \beta_y|}{k_0} \tag{2.12}$$

Another measure of this strength is called fiber beat length, which is defined as

$$L_\mathrm{B} = \frac{2\pi}{|\beta_x - \beta_y|} = \frac{\lambda}{\mathrm{B}_m} \tag{2.13}$$

For a give value of B_m, two orthogonal polarization states exchange their power in a periodic manner as they propagate in fiber, and the period is beat length L_B as defined in 2.13.

Knowledge of the fiber birefringent dispersion strength is also very meaningful, especially for the design of mode-locked fiber laser by NPE mechanism. The following section discusses and presents the method we used to measure fiber's birefringence.

2.1.4 Birefringent dispersion measurement

Like to characterize fiber chromatic dispersion, numerous methods can be applied to measure fiber birefringent dispersion [32, 33, 34]. For us, a fiber Sagnac loop interferometer by a 3-dB 2×2 fiber coupler and a set-up as shown in Figure 2.12 are used to measure the fiber birefringence. Moreover by tracing birefringence change and response to environmental transverse stress and bending experienced by the FUT, this set-up has been reported to serve as a valuable optical fiber sensor [35].

The principal of this birefringent dispersion measurement can be briefed as follows: initially the broadband light source is evenly coupled into the fiber loop along clockwise and counterclockwise directions through the $3dB$ fiber coupler and when these two parts of light recombine in the coupler,they will interfere and interference fringes are generated and registered by the optical spectrum analyzer(OSA) if the fiber loop exhibits birefringent dispersion. Jones matrices in linear polarization basis to present the fiber loop along clockwise and counterclockwise directions are written as:

$$M_{CW} = \begin{bmatrix} A & -B^* \\ B & A^* \end{bmatrix}, \quad M_{CCW} = \begin{bmatrix} A & -B \\ B^* & A^* \end{bmatrix} \tag{2.14}$$

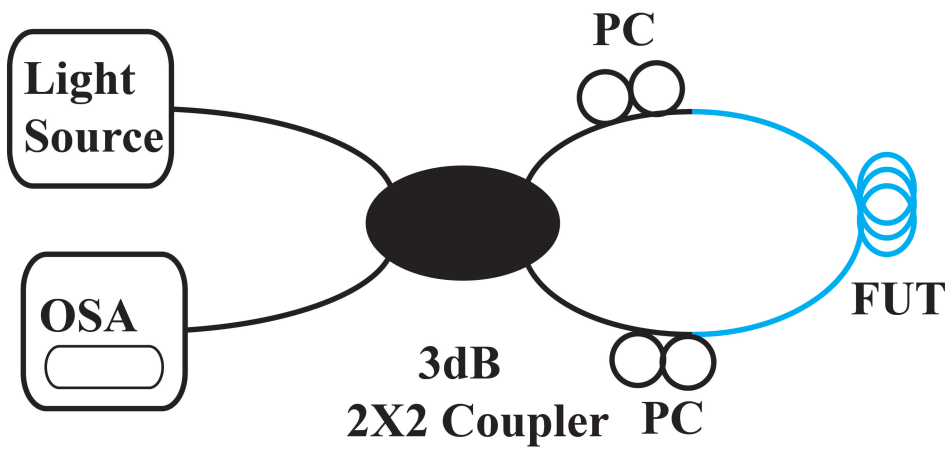

Figure 2.12: Sagnac interferometer by a 3-dB 2×2 fiber coupler to measure and trace the birefringence of FUT(PC: optional polarization controller)

If a linearly polarized light $[\begin{smallmatrix}1\\0\end{smallmatrix}]$ is initially coupled into the fiber loop, the light field registered by the OSA would be $[\begin{smallmatrix}iIm(B)\\0\end{smallmatrix}]$ (note: there is $\pi/2$ wavelength-independent phase delay between the two split fields). Similarly if a linearly polarized light $[\begin{smallmatrix}0\\1\end{smallmatrix}]$ is coupled into the fiber loop, the field detected by OSA is $[\begin{smallmatrix}0\\iIm(B)\end{smallmatrix}]$. The output intensity through the OSA port is thus the same for any polarization, and unpolarized light and majorly decided by birefringence B of the included fiber loop. Assuming the accumulated phase delay due to linear birefringence of the fiber loop is φ, the light intensity addressed by the OSA port is then $I_0 \sin^2(\varphi/2)$. Since φ is wavelength dependent, it means different wavelength will experience different phase shift and it is interference fringes over wavelength that is registered on the OSA.

Mathematically, the differential phase between two polarized modes after propagating through fiber of length L is:

$$\varphi = \frac{2\pi L \mathrm{B}_m(\lambda)}{\lambda} \tag{2.15}$$

then

$$\frac{\mathrm{d}\varphi}{\mathrm{d}\lambda} = \frac{2\pi L}{\lambda^2}\left(\lambda\frac{\mathrm{dB}_m(\lambda)}{\mathrm{d}\lambda} - \mathrm{B}_m(\lambda)\right) \approx -\frac{2\pi L}{\lambda^2}\mathrm{B}_m(\lambda), \text{ if } \lambda\frac{\mathrm{dB}_m(\lambda)}{\mathrm{d}\lambda} \ll \mathrm{B}_m(\lambda) \tag{2.16}$$

Set $\triangle\varphi = -2\pi$ as for two neighboring interference dips,

$$\mathrm{B}_m = \frac{\lambda^2}{\triangle\lambda L} \tag{2.17}$$

Figure 2.13 shows the interference pattern for 75-cm Hi-Bi PM fiber included in the above

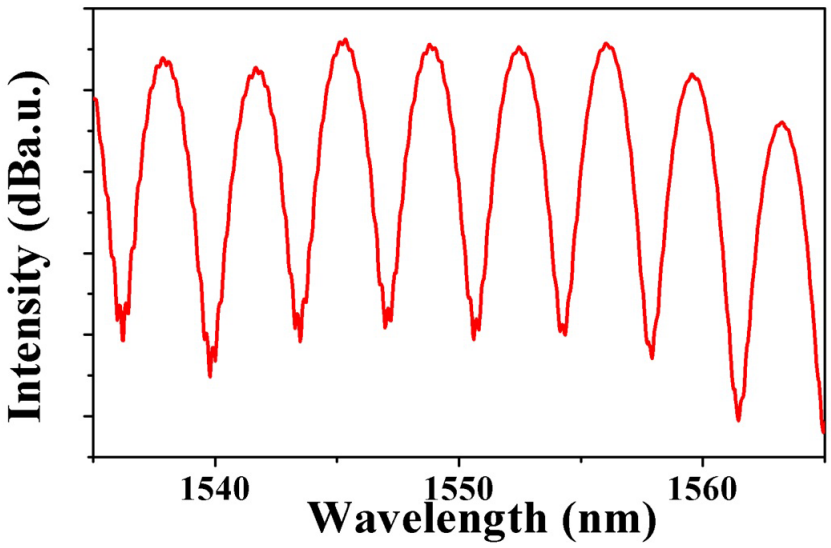

Figure 2.13: Sagnac interference pattern for 75-cm Hi-Bi PM Fiber centered at 1550nm

mentioned Sagnac loop interferometer. The spectral dips are evenly separated by $3.58nm$ and the birefringence for the Hi-Bi PM fiber is calculated as 8.93×10^{-4} and the corresponding beat length is $1.68mm$ at $1550nm$ or $2.17mm$ at $2\mu m$. The beat length of standard single-mode fiber SMF-28e is measured about $25 \pm 5m$ at $2\mu m$.

2.1.5 Nonlinearity of fiber

Besides linear dispersions as discussed above, another key property of fiber is nonlinearity. This part is presented in Section 3.2.2.

2.2 ACTIVE RARE EARTH DOPED FIBERS

This part is going to concisely talk about the active fibers for which the fiber core area is doped with rare-earth ions and thus provides the needed gain to build a fiber laser or amplifier. In particular, some properties like lasing transition and absorption and emission spectra of the Thulium-doped silicate fiber we use to build our mode-locked $2\mu m$ fiber lasers are covered in this part.

2.2.1 Rare earth dopants in glass fibers

Shortly after the invention of laser [5], scientists came up with the idea to host the gain medium in the fiber and thus made fiber lasers. As fiber lasers offer many valuable merits. Dopants are added into the core of fiber and provide the required optical gain for the amplifier and these dopants are commonly ions of rare-earth elements like Erbium, Ytterbium, Neodymium, Holmium, Praseodymium and Thulium. And the hosting materials are usually various glasses such as silicate, fluoride, tellurite, chalcogenide and others. Recently, with the availability of low-loss fibers and matured fiber doping technology , significant progress about fiber lasers has been made and reported in the past 30 years and fiber lasers have become more practical and attractive for both laboratorial research and industrial applications.

Rare-earth doped fiber lasers provide gain to generate lasers at many important wavelengths, which depends on the selection of dopant and also host. For example, Erbium-doped silicate fiber lasers produce light at a wavelength near 1550nm, given proper optical pump and they have been widely used as the signal carrier for long-distance high-speed telecommunication, as the well-developed silicate glass fibers exhibit the lowest loss near this Erbium's emission wavelength.

Table 2.1: Common rare-earth doped silicate fibers and their typical pump and emission wavelength in near-IR.

Ion in Silica	$\lambda_{pump}(\mu m)$	$\lambda_{emission}(\mu m)$	Gain Bandwidth
Ytterbium(Yb^{+3})	089, 0.98	1.06	∼20
Erbium(Er^{+3})	0.98, 1.48	1.55	∼40
Thulium(Tm^{+3})	0.79, 1.55	1.93	∼200
Neodymium(Nd^{+3})	0.59, 0.79	1.06	∼20
Praseodymium(Pr^{+3})	0.59	1.06	∼20
Holmium(Ho^{+3})	0.46, 1.91	2.1	∼200

Table 2.1 lists the commonly used rare-earth doped silicate fibers and their typical pump and emission wavelengths in near-IR range. These rare-earth ions can also be solely doped or co-doped in other sorts of glass. The chemical composition of the hosting glass also has its significant influence on the performance of the fabricated active fiber. First, the hosting glass decides fiber's transparency range and limits its application. For example, silicate fiber's transparency window starts from visible and terminates close to $2.4\mu m$[36], and beyond this range, silicate fiber exhibits strong absorption. Other hosting glasses need to be employed e.g. fluoride and chalcogenide if we want to extend fiber's operation wavelength range into mid-IR. Also the glass composition shows strong influenc on the possible maximum dopant concentration. For some glasses, the dopant ions can not be densely added without generated excessive clusters and these excessive clusters would result unwanted quenching effect and cause more propagation loss. Thirdly, the hosting glass also has its influences on the optical transitions of the rare earth ions, like the emission and absorption cross sections, absorption and emission bandwidth, total transition rates and thus the meta-stable level lifetimes, etc. In this thesis, the rare-earth doped fibers (EDF, TDF, YDF) we used are all rare-earth ions doped in silicate glass. Compared to other specialty glasses, the biggest advantage of silicate fibers is that they can be easily cleaved and spliced by using the commercially available equipment.

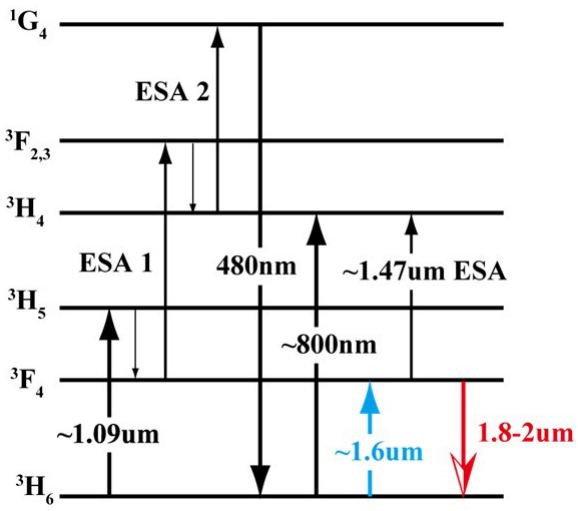

Figure 2.14: Energy levels diagram of Tm^{3+} in silica

2.2.2 Thulium doped silicate fiber

Of various kinds of rare-earth ions doped active fibers, thulium doped fiber(TDF) has its own unique energy transition lines. Figure 2.14 is the diagram of energy transitions of thulium ions doped in silicated fiber. The desired emission around $\sim 1.9\mu m$ is produced from the $^3F_4 \rightarrow {}^3H_6$ transition. The lifetime of the upper state $^3F_4$ in silica was measured and reported to be $\sim 5ms$ [**?**], which is comparable to erbium in silica $^3I_{13/2}$ $\sim 10ms$ life time [37]. This relatively long lifetime means the dynamics of the gain saturation would not significantly affect mode-locked or even Q-switched ultra-short($< ns$) pulse amplification. The first passively mode-locked silicate thulium fiber ring laser was reported by Nelson and *et al* in 1995 [24]. In his fiber ring laser configuration, many free space components like the isolator, wave plates and output couplers were involved in the cavity and a bulky and high-cost Ti:Sapphire CW laser operated at $785nm$ was used as the pump, which actually made this setup less economic and impractical for real applications.

The absorption spectrum of thulium in silica was also reported in Ref [38]. To excite the $^3F_4 \rightarrow {}^3H_6$ laser transition, light sources at wavelength $\sim 790nm$ can be used as pump

and yield higher conversion efficiency because of the so called cross-relaxation process [39]. Besides $\sim 790nm$, thulium in silica also shows strong absorption around $1.55\mu m$ which is located within silicate erbium fiber emission range which also makes $1.55\mu m$ EDFA a good candidate as the pump source. The advantages of using $1.55\mu m$ EDFAs as pump light are obvious too. Firstly, high power EDFAs with single mode output have been well developed and become a matured technology. Then, the merits of an all-fiber system can be easily preserved by selecting EDFAs as the pump, since at this wavelength many low-cost fiber parts like WDM and output couplers are commercially available now. Also $1.55\mu m$ is eye-safe and the actual laser builder or operator do not need to concern about the light pollution from the pump light leakage. As shown in Section 2.1.2, Figure 2.8 is the spontaneous emission spectrum from thulium silicate fiber under $\sim 1.55\mu m$ pump.

3.0 MODELING OF MODE-LOCKED FIBER LASERS

The chapter is meant to derive the physics and equations that backup and govern the short pulse generation via different mode-locking mechanisms in a passively mode locked fiber laser system. We start with the fundamental of lasers and mode-locking for short pulse generation, and then discuss the electric magnetic wave equation in fibers and the modeling of pulse propagation and evolution in fiber laser cavity by different mode-locking techniques. In the end, a numerical simulator with graphical user interface is developed to simulate passively mode-locked ultrashort pulse generation in fiber cavity.

3.1 LASERS

Laser, standing for light amplification of stimulated emission of radiation, is a light source which is capable of producing highly spatial and/or temporal coherent electromagnetic wave via the process of optical amplification based on the stimulated photon emission within the gain medium. The first working laser was invented by Th. Maiman [5]. Ever since its birth, lasers have significantly changed the ways we see, we communicate, we measure and many other aspects in our life.

3.1.1 Fundamentals of laser

To build a laser system, three fundamental parts are necessitated that include pump, gain medium and laser cavity. Among these three key elements, the pump is the energy supplier to keep the system running with continuous output, and for different types of lasers the form

of the pump can be either electrical current or optical pump from a flash light or another laser of different wavelength. The gain medium is a material with properties that allow it to amplify light through stimulated emission process. Light of a specific wavelength that passes through the gain medium is amplified and thus the intensity of light increases. The laser cavity, usually consisting of two partial reflectors with certain space between, provides the optical feedback and selects the operational frequency. Figure 3.1 is the illustration for an optically pumped laser, in which the green arrow stands for the pump light, and the gain medium is sandwiched by two mirrors to construct a laser cavity. For a real laser system additional parts, considerations and dedicated designs might be needed to meet the practical output requirements. Figure 3.2 shows the light-atom interaction and stimulated

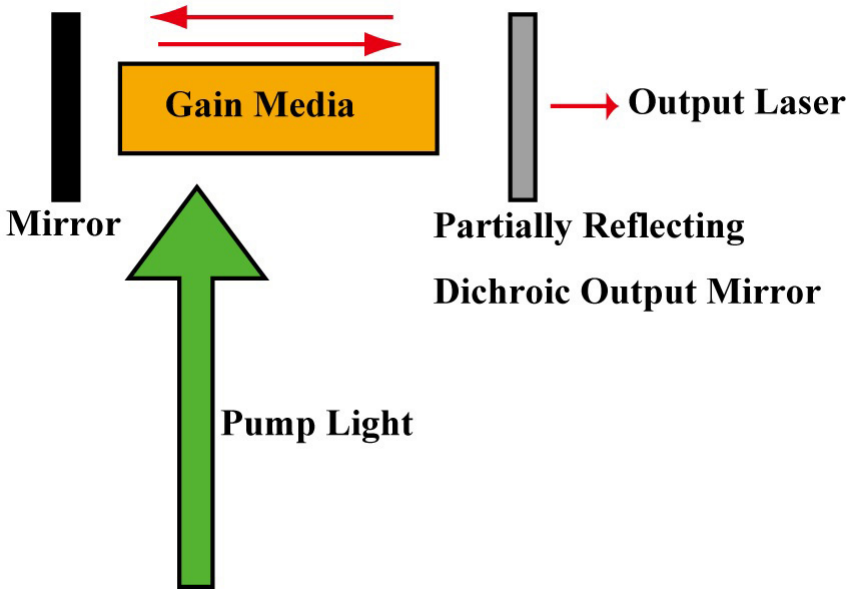

Figure 3.1: Scheme of an optically pumped laser with pump, gain medium and cavity

emission transition for a 3-level laser system. In quantum physics, the energy of an atom display many discrete levels. In a 3-level laser, each atom in gain medium is able to stay in any of three energy states E_1, E_2 and E_3 ($E_1 < E_2 < E_3$). There are a fast decay between levels 3 and level 2 and a slow decay between level 2 and level 1 between these levels. Initially, under thermal equilibrium most of the atoms will be in the ground state E_1. Then incident pump radiation of frequency $\omega_{pump} = (E_3 - E_1)/\hbar$ (green in Fig. 3.2) is used

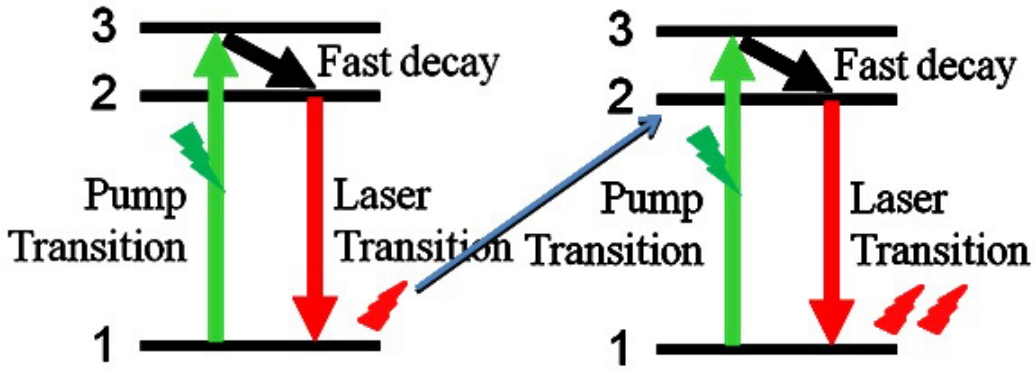

Figure 3.2: Illustration of spontaneous emission(left) and stimulated emission(right) in an optically pumped 3-level laser.

to raise atoms from the level 1 to level 3. As the electron can not hold and stay at an excited state forever, it firstly falls to lower excited level 2 via fast decay without light emission, then the electron spontaneously falls back to ground state meanwhile a photon (red in Fig. 3.2) of energy $E_2 - E_1$ and random phase is emitted. This process is called spontaneous emission. Besides falling from level 2 to level 1 by spontaneous emission, electron can also be stimulated and jump down from E_2 to E_1. In the gain medium, since there are millions of ions and many ions can be of the same energy state, once the red photon generated in the spontaneous emission as mentioned above interacts with another atom sitting on level 2, the second atom can be stimulated down to level 1 meanwhile one more red photon that is identical in energy, phase, polarization and directivity to the first red photon will be produced as shown as the right part in Figure 3.2. In this process, a photon is emitted into the mode of the incoming photon and the power of the incoming radiation is doubled. This is call stimulated emission. Thanks to the feedback provided by the cavity mirrors, when equilibrium reaches, the resulted photons in cavity will condense into the same state and partial of these condensed photons are coupled out of the laser cavity through a output coupler. This is how a laser works. Besides feedback, the cavity also plays role in the lasing frequency selection. By applying the boundary condition that is the field is none at the two end bouncing surfaces, the modes of the light wavelength allowed in a linear cavity with

optical length L is given as follows:

$$\lambda_N = \frac{2L}{N} \tag{3.1}$$

where N is an integer, standing for mode number. This selection rule can also be expressed in terms of the angular frequency of the allowed modes as:

$$\omega_N = \frac{\pi c N}{L} \tag{3.2}$$

Usually, the optical cavity is several centimeters to couple meters in length and the value of N is as large as on the order of million and the interval between each mode is pretty small if we convert it into nm or cm^{-1}, so there could be several adjacent modes of ω_N which still fall within the gain spectrum of the lasing medium.

A crucial physical difference between linear and ring cavity geometries is that for the ring resonator case, the phase matching condition is required at the end-facet junction, forcing integer-wavelength boundary conditions within the cavity. Therefore, different from Equation 3.1 and 3.2, the modes of the laser wavelength allowed in a ring cavity with optical length L is given as follows:

$$\lambda_N = \frac{L}{N} \tag{3.3}$$

and the corresponding angular frequency of the allowed modes in a ring cavity is:

$$\omega_N = \frac{2\pi c N}{L} \tag{3.4}$$

3.1.2 Short pulse generation from mode-locking

Fourier-Transform tells us purely continuous sinusoidal wave in time domain corresponds to a single shot in frequency domain, while an ultrashort pulse like an ideal delta function in time domain has uniform power distribution over the entire range of the frequency domain. As discussed in 3.1.1, usually there exist a few adjacent frequency modes in the laser cavity, and the angular frequency for each mode is expressed as 3.4. If these frequency modes

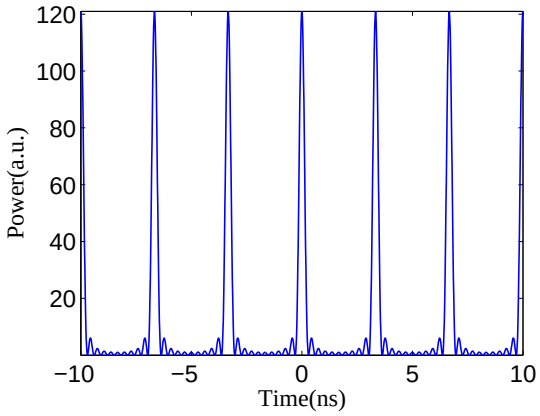

Figure 3.3: Mode-locked short pulses generation from 11 adjacent modes around $2\mu m$ with fixed phase $\phi_N = 0$ and equal amplitude in a 1-m ring cavity.

simultaneously exit in the cavity and add up with certain phase relation $\{\phi_N\}$, the total complex electrical field can be written as

$$\mathbf{E} = \sum_N \mathbf{E}_N \exp[-\mathrm{i}\{\omega_N(t - \frac{z}{c}) + \phi_N\}] \tag{3.5}$$

where the wave moves in z direction. Short pulses will be generated in temporal domain, if these frequency modes are added up with a fixed or locked phase relation $\{\phi_N\}$. Figure 3.3 shows the periodic short pulses generated by mode-locking 11 adjacent modes around $2\mu m$ with fixed phase $\{\phi_N = 0\}$ and equal amplitude in a 1-m ring cavity. The transform-limit pulse width is determined by the Fourier-transform limit of added field $\mathbf{E}$ and is proportional to the inverse of the number of modes in the cavity as in Equation 3.6.

$$\Delta t \propto \frac{2\pi}{N\Delta\omega} = \frac{L}{Nc} \tag{3.6}$$

Besides constant phase relation, different chirped pulse shapes can be produced from other locked phase relations. However if the phases $\{\phi_N\}$ are randomly varying, the output is not short pulse but random noise despite of the wide power distribution over the frequency spectrum, which is shown as the right case in Figure 3.4.

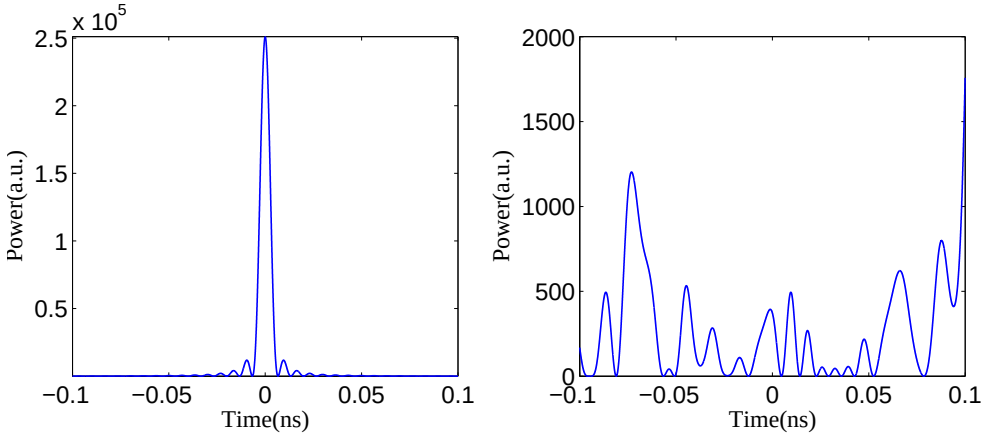

Figure 3.4: Added outputs of 500 adjacent modes around $2\mu m$ with equal amplitudes and fixed phase(left) and random phase(right) ϕ_N in a 1-m ring cavity.

3.2 PULSE PROPAGATION IN PASSIVE FIBER

As electro-magnetic field, the propagation of mode-locked pulse inside fiber is still backed by Maxwell equations [40]:

$$\begin{aligned} \nabla \cdot \mathbf{D} &= \rho \\ \nabla \cdot \mathbf{B} &= 0 \\ \nabla \times \mathbf{E} &= -\frac{\partial \mathbf{B}}{\partial t} \\ \nabla \times \mathbf{H} &= \mathbf{J} + \frac{\partial \mathbf{D}}{\partial t} \end{aligned} \tag{3.7}$$

In response to the electric field $\mathbf{E}$ and magnetic field $\mathbf{H}$, the electric and magnetic flux densities $\mathbf{D}$ and $\mathbf{B}$ are expressed as:

$$\begin{aligned} \mathbf{D} &= \varepsilon_0 \mathbf{E} + \mathbf{P} \\ \mathbf{B} &= \mu_0 \mathbf{H} + \mathbf{M} \end{aligned} \tag{3.8}$$

where ε_0 and μ_0 are the permittivity and permeability in vacuum respectively, and $\mathbf{P}$ and $\mathbf{M}$ are the induced electric and magnetic polarizations. $\mathbf{M} = 0$ in glass fibers as for a nonmagnetic medium. By taking the curl of the first equation, using others of equations 3.7 and 3.8 and setting $\mathbf{J} = 0$ in fiber, we arrive at

$$\nabla \times \nabla \times \mathbf{E} = -\frac{1}{c^2}\frac{\partial^2 \mathbf{E}}{\partial t^2} - \mu_0 \frac{\partial^2 \mathbf{P}}{\partial t^2} \tag{3.9}$$

where $c = 1/\sqrt{\varepsilon_0 \mu_0}$ is the light speed in vacuum. In response to intense electric field $\mathbf{E}$, nonlinear terms should take into consideration for electric polarization $\mathbf{P}$, especially when the strength of the applied field is comparable with interatomic electric fields(typically, 10^5 to $10^8 V/m$). And the origin of the nonlinear terms is the anharmonic response of the electrons bounded to atoms when external field is applied. In terms of electric field $\mathbf{E}$, polarization $\mathbf{P}$ is expanded as the sum of linear and nonlinear responses as:

$$\mathbf{P} = \mathbf{P}_{LN} + \mathbf{P}_{NL} = \varepsilon_0(\chi^{(1)} \cdot \mathbf{E} + \chi^{(2)} : \mathbf{EE} + \chi^{(3)} \vdots \mathbf{EEE} + \cdots) \tag{3.10}$$

$$\mathbf{P}_{LN} = \varepsilon_0 \chi^{(1)} \cdot \mathbf{E} \tag{3.11}$$

$$\mathbf{P}_{NL} = \varepsilon_0(\chi^{(2)} : \mathbf{EE} + \chi^{(3)} \vdots \mathbf{EEE} + \cdots) \tag{3.12}$$

For most glass fibers, including silica fiber, $\chi^{(2)} = 0$ since glass is centrosymmetric and the fourth and higher orders nonlinearity usually are negligible. We can present the electric polarization in fiber as:

$$\mathbf{P} = \mathbf{P}_{LN} + \mathbf{P}_{NL} = \varepsilon_0(\chi^{(1)} \cdot \mathbf{E} + \chi^{(3)} \vdots \mathbf{EEE}) \tag{3.13}$$

$$\mathbf{P}_{LN} = \varepsilon_0 \chi^{(1)} \cdot \mathbf{E} \tag{3.14}$$

$$\mathbf{P}_{NL} = \varepsilon_0 \chi^{(3)} \vdots \mathbf{EEE} \tag{3.15}$$

After using the general relation $\nabla \times \nabla \times \mathbf{E} = \nabla(\nabla \cdot \mathbf{E}) - \nabla^2 \mathbf{E}$ and $\nabla \cdot \mathbf{D} = \varepsilon \nabla \cdot \mathbf{E} = 0$ in dielectric media, we obtain the general wave equation in fiber

$$\nabla^2 \mathbf{E} = \frac{1}{c^2}\frac{\partial^2 \mathbf{E}}{\partial t^2} + \mu_0 \frac{\partial^2 \mathbf{P}_{LN}}{\partial t^2} + \mu_0 \frac{\partial^2 \mathbf{P}_{NL}}{\partial t^2} \tag{3.16}$$

which includes the linear and nonlinear polarizations in fiber in response to the electric field $\mathbf{E}(\mathbf{r}, t)$. Starting from the general wave equation 3.16, by separating variables in the

transversal and longitudinal directions of fiber, treating the nonlinear polarization term $\mathbf{P}_{NL}$ as small perturbation and using slowly varying envelope approximation, light intensity distribution over transversal modes and behaviors of light pulse propagation along fiber can be mathematically solved and more details about the derivation can be found in Appendices. In this thesis, all fibers involved are operated under single-mode condition, so we are only going to discuss the fundamental LP_{01} mode propagation in fiber.

3.2.1 Light pulse propagation in dispersive linear media

For applications where light pulse of relatively small amplitude is used(e.g. Telecommunication industry), its propagation behaviors are mainly determined by fiber's linear dispersive properties as shown in Equation 3.17

$$\mathrm{i}\frac{\partial A}{\partial z} + \sum_N \mathrm{i}^N \frac{\beta_N}{N!}\frac{\partial^N A}{\partial t^N} + \mathrm{i}\frac{\alpha}{2}A = 0 \tag{3.17}$$

where $A(z,t)$ is the slowly varying complex amplitude of pulse envelope, β_N is fiber's Nth-order dispersion and α is the fiber's transmittance loss. In most fibers for pulse of width $> 1ps$, the second order β_2 dispersion dominates when light propagates. Dropping high order dispersion terms and adopting a classical coordinate translation that moves with the pulse at the group velocity v_g ($T = t - \beta_1 z$), Equation 3.17 comes to

$$\frac{\partial A}{\partial z} + \mathrm{i}\frac{\beta_2}{2}\frac{\partial^2 A}{\partial T^2} + \frac{\alpha}{2}A = 0 \tag{3.18}$$

By normalizing the time scale to the initial pulse width T_0, defining dispersion length L_D according to β_2 and at the same time introducing a normalized amplitude U to its initial peak power P_0 as Equation 3.19, 3.20 and 3.21 for the convenience purpose

$$\tau = \frac{T}{T_0} = \frac{t - z/v_g}{T_0} \tag{3.19}$$

$$L_D = \frac{T_0^2}{|\beta_2|} \tag{3.20}$$

$$U(z,\tau) = \frac{A(z,\tau)\exp(\alpha z/2)}{\sqrt{P_0}} \tag{3.21}$$

3.18 is in form

$$\frac{\partial U}{\partial z} = -\mathrm{i}\frac{\mathrm{sgn}(\beta_2)}{2L_D}\frac{\partial^2 U}{\partial \tau^2} \tag{3.22}$$

Further by moving L_D to the right size, and defining $\xi = z/L_D$, we get

$$\frac{\partial U}{\partial \xi} = -\mathrm{i}\frac{\mathrm{sgn}(\beta_2)}{2}\frac{\partial^2 U}{\partial \tau^2} \tag{3.23}$$

which is a lot more simple and readily to be solved by applying the Fourier-transform method with suitable scales in both time and space domains. After applying Fourier-transform about the normalized time τ, which is to replace $\partial^N/\partial\tau^N$ with $(-\mathrm{i}\omega)^N$, Equation 3.23 has its presentation in frequency domain as

$$\frac{\partial \tilde{U}}{\partial \xi} = \mathrm{i}\frac{\mathrm{sgn}(\beta_2)}{2}\omega^2\tilde{U} \tag{3.24}$$

whose analytical solution is given by

$$\tilde{U}(\xi,\omega) = \tilde{U}(0,\omega)\exp\left(\mathrm{i}\frac{\mathrm{sgn}(\beta_2)}{2}\omega^2\xi\right) \tag{3.25}$$

where $\tilde{U}(0,\omega)$, the Fourier transform of the launched pulse at $\xi = 0$ is obtained by

$$\tilde{U}(0,\omega) = \int_{-\infty}^{\infty} U(0,\tau)\exp(\mathrm{i}\omega\tau)\mathrm{d}\tau \tag{3.26}$$

To see the propagation behaviors of optical pulses traveling in dispersive media when the second order dispersion β_2 dominates, we take the case of a Gaussian shaped pulse for example, and the incident Gaussian pulse is of form

$$U(0,T) = \exp\left(-\frac{T^2}{2T_0^2}\right) \tag{3.27}$$

Setting $T_0 = 10ps$ and $\beta_2 = -250ps^2/km$ and following the procedures as discussed above from 3.19 to 3.23, we calculate and find $L_D = 100m$ for the incident pulse and then using 3.25, we can numerically solve pulse propagation behaviors inside linear dispersive medium. Figure 3.5 shows the pulse temporal evolution as it propagates through 300-m fiber which is $3L_D$ The launched transform-limit Gaussian pulse is monotonically broadened as traveling in dispersive fiber and the broadening factor versus traveling distance is extracted and shown in Figure 3.6. After about L_D, a linear relation between the pulse width and the traveling

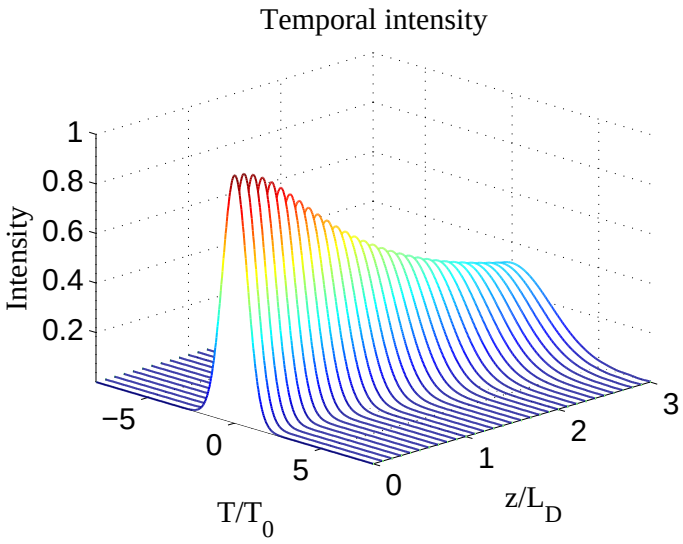

Figure 3.5: Launched transform-limit pulse temporal evolution through $3L_D$.

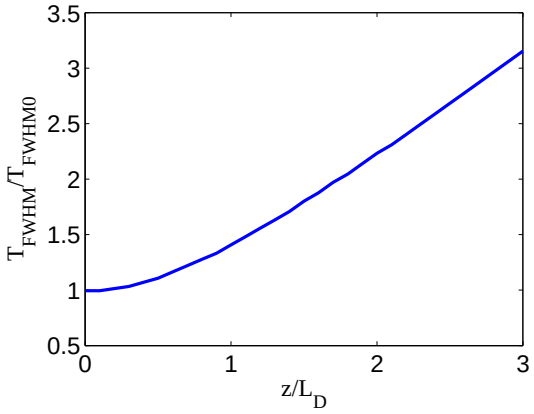

Figure 3.6: Launched transform-limit pulse broadening factor through $3L_D$.

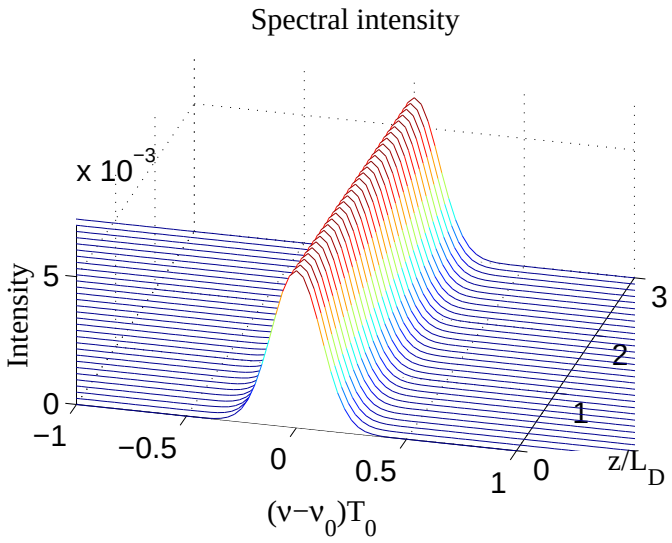

Figure 3.7: Spectral evolution of input pulse through $3L_D$.

distance can be used to approximate this broadening trend. Meanwhile the optical spectrum of the input pulse does not change as it propagates in linear dispersive fiber like shown in 3.7.

Another interesting and important application of linear dispersion is to use fiber of opposite GVD to dechirp incident pulse close to its transform-limit. Again we use the Gaussian pulse for example and the incident Gaussian pulse is chirped with chirping factor C and is of form

$$U(0,T) = \exp\left(-\frac{(1+\mathrm{i}C)}{2}\frac{T^2}{T_0^2}\right) \tag{3.28}$$

Figure 3.8 and 3.9 are the evolution of positively chirped incident pulse with $C = 1.5$ through fiber of negative dispersion. The incident is firstly dechirped to its transform-limit and then broadening as it travels. This technique to use fiber of opposite GVD to compress chirped incident pulse close to its transform-limit has widely used in telecommunication industry to recover launched short optical signal and thus endure the high-speed communication [41, 42]. Additionally for short pulses($T_0 < 1ps$), the influence from fiber's next order dispersion β_3 should also be taken into account as shorter pulse takes broader bandwidth. Also if the

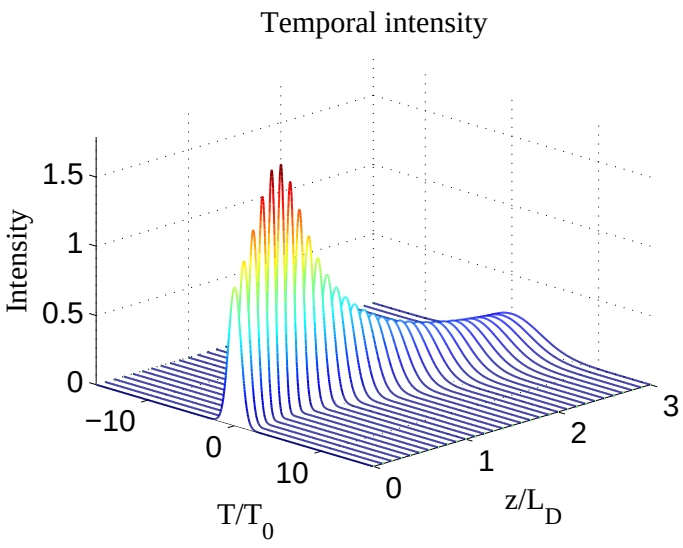

Figure 3.8: Launched chirped pulse temporal evolution through $3L_D$. $C = 1.5,\ \mathrm{sign}(\beta_2) = -1$

center wavelength of the launched light pulse is around fiber's zero dispersion wavelength(e.g. $1.3\mu m$ for SMF-28), the phase change attributed to β_3 no longer can be neglected. With β_3 added into consideration, Equation 3.18 is extended as

$$\frac{\partial A}{\partial z} + \mathrm{i}\frac{\beta_2}{2}\frac{\partial^2 A}{\partial T^2} + \mathrm{i}^2\frac{\beta_3}{6}\frac{\partial^3 A}{\partial T^3} + \frac{\alpha}{2}A = 0 \tag{3.29}$$

which can also be numerically solved by using Fourier-transform method discussed above.

3.2.2 Nonlinear effects in fiber

Because of the existence of the nonlinear polarization response $\mathbf{P}_{NL}$ as in 3.15 in glass fibers, the dielectric constant ε is intensity dependent and has its nonlinear part ε_{NL}

$$\varepsilon = 1 + \chi^{(1)}_{xx} + \varepsilon_{NL} \tag{3.30}$$

$$\varepsilon_{NL} = \frac{3}{4}\chi^{(3)}_{xxxx}|\mathbf{E}|^2 \tag{3.31}$$

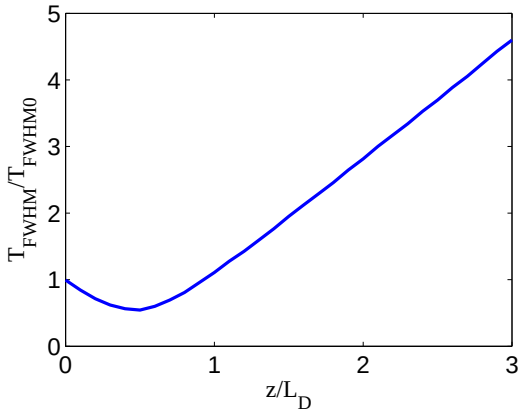

Figure 3.9: Launched chirped pulse broadening factor through $3L_D$. $C = 1.5$, $\text{sign}(\beta_2) = -1$

The refractive index $\tilde{n}$ that light actually experiences when traveling in fiber is thus also intensity dependent

$$\tilde{n} = n + n_2|\mathbf{E}|^2 \tag{3.32}$$

where

$$n_2 = \frac{3}{8n}\text{Re}\left(\chi^{(3)}_{xxxx}\right) \tag{3.33}$$

For transparent crystals and glasses, n_2 is typically of the order of 10^{-16} to $10^{-14} cm^2/W$. Silica, as used in silica fibers, has a nonlinear index of $n_2 = 2.7 \times 10^{-16} cm^2/W$ [43]. When intense light encounters, this intensity dependence of the refractive index in nonlinear fiber media manifests through an interesting phenomenon called self phase modulation(SPM) that leads to the spectral broadening of incident light. After similar arrangements as Equation 3.19 and 3.21 for the convenience purpose and introducing nonlinear length L_{NL}

$$L_{NL} = (\gamma P_0)^{-1} \tag{3.34}$$

where $\gamma = \frac{n_2\omega}{cA_{eff}}$, the pulse propagation equation solely governed by SPM becomes

$$\frac{\partial U}{\partial z} = \text{i}\frac{|U|^2}{L_{NL}}U \tag{3.35}$$

where we omit all fiber's linear dispersive effects and loss (more details are going to be included in Appendices).

The solution to Equation 3.35 can be obtained by setting $U = V\ \exp(\mathrm{i}\phi_{NL})$ and equalizing both the real and imaginary parts

$$\frac{\partial V}{\partial z} = 0; \quad \frac{\partial \phi_{NL}}{\partial z} = \frac{V^2}{L_{NL}} \tag{3.36}$$

and the general solution to Equation 3.35 is found to be of form

$$U(L,T) = U(0,T)\exp[\mathrm{i}\phi_{NL}(L,T)] \tag{3.37}$$

where

$$\phi_{NL} = |U(0,T)|^2(L/L_{NL}) \tag{3.38}$$

is called nonlinear phase shift. To depict the SPM induced pulse propagation behaviors, we use a typical value $\gamma = 1W^{-1}/km$ for regular single mode silicate fiber, and $P_0 = 100W$ for the incident peak power commonly realized in a mode-locked fiber laser. The fiber nonlinear length L_{NL} is calculated as $10m$ from Equation 3.34. Using transform-limit Gaussian shaped pulse as the incident again, Figure 3.10 shows the pulse evolution through $50m$ ($5L_{NL}$) fiber. Temporally the incident pulse shape remains unaffected but new spectral components symmetrical about the central carrier frequency are generated as pulse propagates. This spectral broadening induced by SPM is a direct consequence of the time dependence of the nonlinear phase shift ϕ_{NL}, as temporally varying phase means instantaneous frequency differences across the pulse from the central carrier frequency ω_0. This difference $\delta\omega$ from the center carrier frequency is given by

$$\delta\omega = -\frac{\partial \phi_{NL}}{\partial T} \tag{3.39}$$

The time dependence of $\delta\omega$ is called frequency chirping. The SPM induced chirp for a transform-limit Gaussian pulse after $5L_{NL}$ is shown in Figure 3.11. It is found from the plot $\delta\omega$ is negative at the leading edge and becomes positive at the tailing edge which is because it is always normal chirping that is generated across the pulse for most materials whose $n_2 > 0$. However the detailed chirp profile across the pulse also strongly depends the exact pulse shape of the incident beam [44].

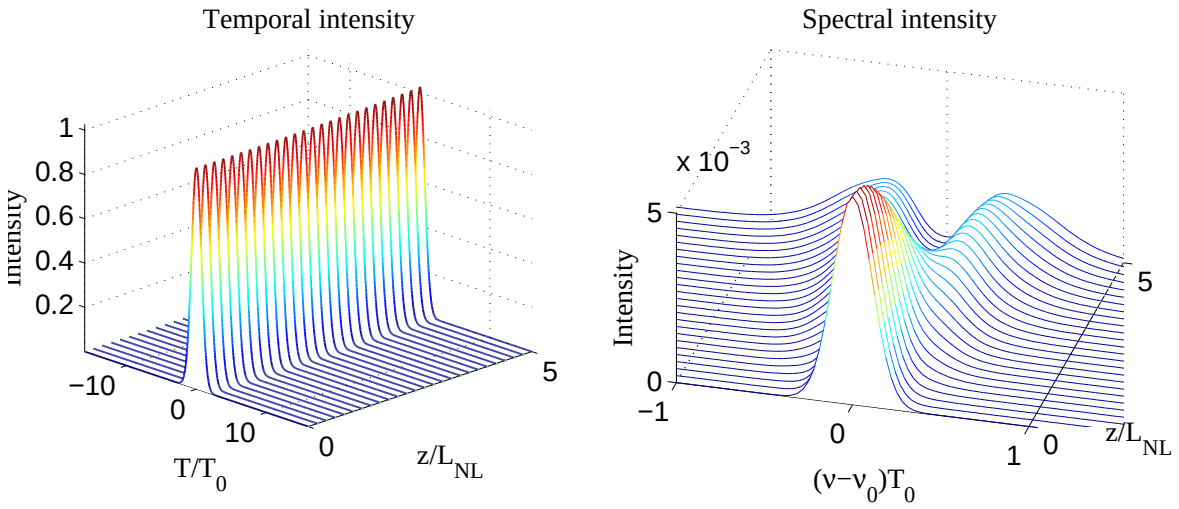

Figure 3.10: SPM induced pulse temporal(left) and spectral(right) evolution through $5L_{NL}$, using transform-limit Gaussian as the incident.

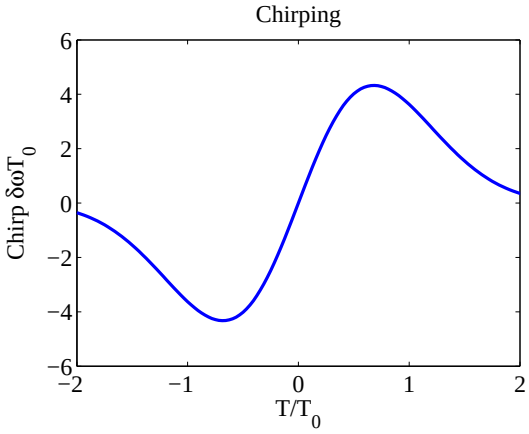

Figure 3.11: SPM induced chirp after $5L_{NL}$, using transform-limit Gaussian as the incident.

So far under the assumption of instantaneous nonlinear response and neglecting the contribution of molecular vibrations to $\chi^{(3)}$, we have studied and demonstrated pulse propagation behaviors governed solely by SPM as in the simplified Equation 3.35. This simplification is valid for pulses of duration $> 1ps$ and moderate pulse energy in silica fibers, as it is found

high order nonlinear effects Raman response in silica occurs only over a short time scale 60-70fs [45]. This simplified model has been successfully in explaining a large number of nonlinear phenomena in fiber and later in this thesis it will be shown a simulation model by including only the SPM term as the dominating nonlinear effect is sufficient and able to qualitatively resemble mode-locking in the fiber seed oscillator. However, when dealing with optical pulses with short duration ($< 1ps$) and large pulse energy ($> 10nJ$), high order nonlinear effects like Raman should be included in our model and the equation extended with higher order nonlinear effects is presented as

$$\frac{\partial U}{\partial z} = \frac{\mathrm{i}}{L_{NL}}\left(|U|^2U + \mathrm{i}s\frac{\partial}{\partial \tau}(|U|^2U) - \tau_R U\frac{\partial |U|^2}{\partial \tau}\right) \tag{3.40}$$

where $s = 1/(\omega_0 T_0)$ and $\tau_R = T_R/T_0$ are the normalized coefficients for self-steepening and intra-pulse Raman scattering respectively. In addition, a set of equations of the form like 3.40 are needed to simulate other nonlinear effects like cross-phase modulation(XPM) and four-wave mixing(FWM) when the required phase matching condition is met between multiple pulses [44].

3.2.3 Nonlinear Schrödinger Equations

By separating fiber dispersion and nonlinearity effects in previous sections 3.2.1 and 3.2.2. we have discussed fiber's dispersion and nonlinearity and demonstrated pulse propagation behaviors induced by these two factors respectively. In practice, dispersion and nonlinearity simultaneously exhibit in fibers. Given proper pulse duration and intensity, its in-fiber propagation behaviors are influenced by the combined effects from the linear dispersion and nonlinearity. If we assume the main effective linear term is the GVD and nonlinear term is the SPM which is valid for most passively mode-locked fiber lasers, the pulse propagation is then governed by the Equation 3.41 which is referred as nonlinear Schrödinger equation(NLSE).

$$\mathrm{i}\frac{\partial A}{\partial z} = \frac{\beta_2}{2}\frac{\partial^2 A}{\partial T^2} - \gamma|A|^2A \tag{3.41}$$

After normalizing the time and amplitude as in Equation 3.19 and 3.21 and introducing dispersion length and nonlinear length as 3.20 and 3.34, Equation 3.41 is rewritten as

$$\mathrm{i}\frac{\partial U}{\partial \xi} = \mathrm{sign}(\beta_2)\frac{1}{2}\frac{\partial^2 U}{\partial \tau^2} - N^2|U|^2U \tag{3.42}$$

where $\xi = z/L_D$ and N^2 is defined as

$$N^2 = \frac{L_D}{L_{NL}} = \frac{\gamma P_0 T_0^2}{|\beta_2|} \tag{3.43}$$

N^2 is the parameter that quantitatively compares the SPM strength to that by GVD. For example, the SPM dominates if $N^2 \gg 1$ and GVD rules when $N^2 \ll 1$.

A special solution to NLSE 3.42 referred as soliton is of strong interest and exists for medium that takes anomalous dispersion($\beta_2 < 0$) for which the fiber dispersion and pulse SPM cancel each other [46, 47, 48]. The parameter N^2 can be set to 1 by choosing proper time width $T_0 = T_c$ for which $\gamma P_0 T_c^2/|\beta_2| = 1$ and Equation 3.42 comes to

$$\mathrm{i}\frac{\partial U}{\partial \xi} + \frac{1}{2}\frac{\partial^2 U}{\partial \tau^2} + |U|^2U = 0 \tag{3.44}$$

under the circumstances $\beta_2 < 0$. The analytical solution for fundamental soliton is of form

$$U(\xi,\, \tau) = \mathrm{sech}(\tau)\exp(\mathrm{i}\xi/2) \tag{3.45}$$

Figure 3.12 and 3.13 show fundamental soliton's propagating behaviors in time and spectral domain respectively. As seen, the fundamental soliton preserves its profiles in both time and spectral domains without being dispersed as traveling in fiber due to the canceling out between SPM and fiber's anomalous dispersion. The perk power for the fundamental soliton in terms of the soliton duration and fiber dispersion is expressed as

$$P_0 = \frac{|\beta_2|}{\gamma T_c^2} \approx \frac{3.11|\beta_2|}{\gamma T_{\mathrm{FWHM}}^2} \tag{3.46}$$

where T_{FWHM} is soliton's width at FWHM, $T_{\mathrm{FWHM}} \approx 1.76T_c$ and the soliton's energy is inversely proportional to its duration $E_{\mathrm{soliton}} \propto 1/T_c$. In addition to fundamental soliton, solutions of form

$$U(\xi,\, \tau) = N\mathrm{sech}(\tau) \tag{3.47}$$

where N is an integer, referred as N-th order solitons are also of special interests, as these high-order soliton evolute in a periodic manner in fiber in time and spectral domains.

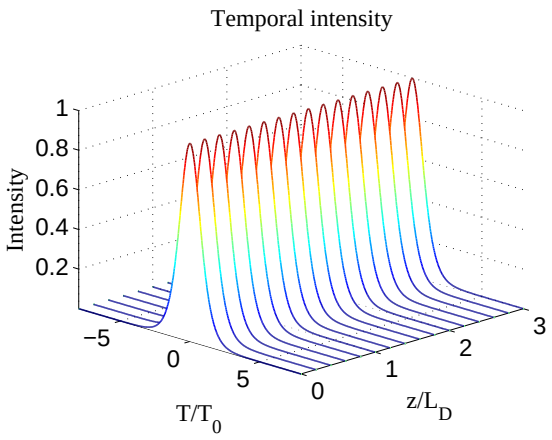

Figure 3.12: Fundamental soliton propagating in fiber(time domain).

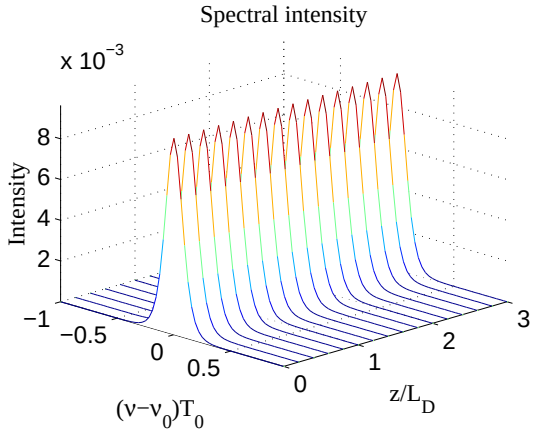

Figure 3.13: Fundamental soliton propagating in fiber(spectral domain) .

3.3 PULSE PROPAGATION IN ACTIVE RARE EARTH DOPED FIBER

This section discusses the behaviors of pulse propagation in active gain fibers, which will deal with small signal amplification, gain saturation and approximation of gain profile and ends with the derivation of Ginzburgh-Laudau Equations that governs and will be used to simulate light propagation in active gain fiber.

3.3.1 Gain profile and gain saturation

Active rare-earth doped fiber provides the required gain that counteracts the loss due to other parts like output couplers and keeps laser continuously running for fiber lasers. In general, light is amplified as it travels through the gain fiber and this amplification through active media is governed by

$$\frac{\partial A(t,z)}{\partial z} = \frac{1}{2}\int_{-\infty}^{\infty} g(t-t^{'},z)A(t^{'},z)dt^{'} \tag{3.48}$$

where $g(t,z)$ is the fiber linear gain strength and we ignore dispersion, nonlinearity and noise term due to amplified spontaneous emission(ASE). The factor $1/2$ comes from the square relationship between intensity and amplitude. However, in addition to this model, the real case is every gain must be saturated as the gain fiber can never provide amplification above the pump power [49]. So we must include this gain saturation into our consideration and express $g(t,z)$ as

$$g(t,z) = \frac{g_0(z)}{1+|A(t,z)|^2/P_{\text{sat}}}\int_{-\infty}^{\infty}\tilde{g}_{\text{s}}(\omega)\exp(-\text{i}\omega t)d\omega \tag{3.49}$$

For rare-earth doped fiber laser, the life-time of the excitation upper state is at the order of $\sim 1ms$, the width of temporal window of interest in our simulation is limited to several hundred picoseconds for mode-locked $\sim 1ps$ pulse generation and the interval between two generated neighboring pulses or pulse bundles are decided by the repetition rate which is at the order of $10MHz$, so as a result, we can do an approximation and replace the instantaneous term $|A(t,z)|^2/P_{\text{sat}}$ in Equation 3.49 with $E(z)/E_{\text{sat}}$ and rewrite 3.49 as

$$g(t,z) = \frac{g_0(z)}{1+E(z)/E_{\text{sat}}}\int_{-\infty}^{\infty}\tilde{g}_{\text{s}}(\omega)\exp(-\text{i}\omega t)d\omega \tag{3.50}$$

where $E(z)$ is the pulse energy that is expressed as the integral

$$E(z) = \int_{-T_{\text{window}/2}}^{T_{\text{window}/2}}|A(t,z)|^2dt \tag{3.51}$$

and E_{sat} is the gain fiber's saturated energy and usually set from $0.1nJ$ to $10nJ$ in a fiber laser depending on the pump power, and $g_0(z)$ is the small signal amplification coefficient and often set as a constant along the gain fiber for simulation simplicity. For rare-earth

doped fibers, the function $\tilde{g}_s(\omega)$ describes the normalized wavelength dependence of gain and is usually not a simple function. However, here we can simply approximate the gain profile by using a Lorentzian profile that is valid for ideal two-level homogenously broadband system [50]

$$\tilde{g}_s(\omega) = \frac{1}{1 + (\omega - \omega_g)^2 T_2^2} \tag{3.52}$$

where T_2 is the introduced dipole relaxation time and decided by the gain bandwidth. By doing Taylor expansion, this Lorentzian profile can be approximated as follows

$$\tilde{g}_s(\omega) \approx 1 - (\omega - \omega_g)^2 T_2^2 \tag{3.53}$$

After taking the gain saturation and using Lorentzian gain profile approximation, Equation 3.48 comes to a form like

$$\frac{\partial A(t,z)}{\partial z} \approx \frac{g_{sat}}{2}\left[A(t,z) + T_2^2 \frac{\partial^2 A(t,z)}{\partial t^2}\right] \tag{3.54}$$

$$g_{sat} = \frac{g_0(z)}{1 + E(z)/E_{sat}} \tag{3.55}$$

which is readily to be integrated to NLSE in order to add fiber dispersion and nonlinearity.

3.3.2 Implication of Ginzburg-Landau Equations

By integrating Equation 3.54 and 3.55 into NLSE Equation 3.41, we obtain the Ginzburg-Landau Equation 3.56 that governs the pulse propagation in gain fiber

$$\frac{\partial A}{\partial z} = -\frac{\mathrm{i}}{2}(\beta_2 + \mathrm{i} g_{sat} T_2^2)\frac{\partial^2 A}{\partial T^2} + \mathrm{i}\gamma |A|^2 A + \frac{1}{2}(g_{sat} - \alpha)A \tag{3.56}$$

for which we add gain fiber's GVD and SPM as the dominating linear dispersive and nonlinear effects into our consideration.

3.4 MODELING OF MODE-LOCKING MECHANISMS

So far, we have established pulse propagation model for passive and active gain fibers, and the output couplers can be modeled and simulated by simply treating them as an pure loss factor that operates on either time or frequency domain. The only thing that is missing so far is to model the passive mode-locking mechanism or mode-lockers we insert into our fiber ring resonator.The passive mode-locking mechanisms or mode-lockers are the nonlinear component that makes the laser favor an operation with short pulse output than CW mode, which introduces higher loss at low power, so that ultrashort pulses with a lot higher peak intensity are going to experience less loss in laser cavity.

3.4.1 Fast saturable absorbers

There are several key parameters of the SAs we utilized in our laser cavity to realize mode-locked output, when designing mode-locked laser systems. These parameters include the SAs' recovery time, modulation depth, working bandwidth, saturation intensity, non-saturable loss and damage threshold. It is concluded the recovery time should be ideally as short as possible in order to favor ultrashort pulse.

The mode-locked TDF lasers presented in Chapter 5 and 6 utilize graphene and SWCNTs as the SAs. It will be demonstrated in the following chapters that the GSAs and SWCNTs SAs can be considered as fast saturable absorbers and their fast saturable absorption can be mathematically simulated in a manner that is similar to the way we use to simulate the gain saturation in active fast. Under the assumption of instantaneous modulation for fast saturable absorbers operation onto pulse, we introduce an intensity dependent loss $\alpha(I)$ like written is Equation 3.57 for example

$$\alpha(I) = \alpha(|A(T)|^2) = \frac{\alpha_s}{1 + I/I_s} \tag{3.57}$$

to simulate the saturable absorption for each round trip when the light pulse interacts with the fabricated SAs and the intensity of light pulse is thus modulated.

3.4.2 Nonlinear polarization evolution

The mode-locked TDF laser presented in Chapter 4 utilizes NPE as the mode-locking mechanism. To simulate the NPE mechanism, we need to treat the two polarizations separately by introducing the Coupled Ginzburg-Landau Equations and these two equation or polarization states interplay with each other by XPM terms as shown in Equations 3.58

$$\begin{cases} \dfrac{\partial U}{\partial z} = \dfrac{\mathrm{i}\Delta\beta}{2}U - \delta\dfrac{\partial U}{\partial \tau} - \dfrac{\mathrm{i}}{2}(\beta_2 + \mathrm{i}gT_2^2)\dfrac{\partial^2 U}{\partial \tau^2} + \mathrm{i}\gamma(|U|^2 + \dfrac{2}{3}|V|^2)U + \dfrac{\mathrm{i}\gamma}{3}V^2U^* + \dfrac{g}{2}U \\ \dfrac{\partial V}{\partial z} = -\dfrac{\mathrm{i}\Delta\beta}{2}V + \delta\dfrac{\partial V}{\partial \tau} - \dfrac{\mathrm{i}}{2}(\beta_2 + \mathrm{i}gT_2^2)\dfrac{\partial^2 V}{\partial \tau^2} + \mathrm{i}\gamma(|V|^2 + \dfrac{2}{3}|U|^2)V + \dfrac{\mathrm{i}\gamma}{3}U^2V^* + \dfrac{g}{2}V \end{cases} \tag{3.58}$$

For each round trip, the polarizer placed in the cavity is represented by its Jones matrix and operates onto the light vector $\left[\begin{smallmatrix} U \\ V \end{smallmatrix}\right]$ to perform the modulation and form the artificial saturable absorption to favor short pulse generation.

3.5 NUMERICAL ALGORITHM AND MODELING PROCEDURES

3.5.1 Split-step Fourier method

Many computational methods have been developed to numerically solve the NLSE as demonstrated in Equation 3.41. Among these different methods, three mostly utilized ones are the split-step Fourier method [51, 52], the time-domain finite-difference method [53, 54] and the inverse scattering method [55]. In these thesis, we utilize the split-step Fourier method to simulate the pulse propagation behaviors inside fiber and model mode-locked TDF laser systems due to its easy implementation, high computation efficiency and excellent expansibility, compared with other method.

The NLSE 3.41 can be written in the form of

$$\frac{\partial A}{\partial z} = \left(\hat{D} + \hat{N}\right) A, \tag{3.59}$$

where $\hat{D}$ is a differential operator accounting for dispersion and $\hat{N}$ is nonlinear operator describing the nonlinear SPM effect. Actually more higher order dispersion terms and linear

fiber losses can be included in the differential operator $\hat{D}$ and meanwhile higher order nonlinear terms like Raman and self steepening effects can be added into the nonlinear operator $\hat{N}$ for a more general model like

$$\hat{D} = -\frac{\alpha}{2} - \frac{\mathrm{i}\beta_2}{2}\frac{\partial^2}{\partial T^2} + \frac{\beta_3}{6}\frac{\partial^3}{\partial T^3} + \cdots, \tag{3.60}$$

$$\hat{N} = \mathrm{i}\gamma\left(|A|^2 + \frac{\mathrm{i}}{\omega_0 A}\frac{\partial}{\partial T}(|A|^2 A) - T_R\frac{\partial|A|^2}{\partial T}\right). \tag{3.61}$$

Mathematically, solution to Equation 3.59 is

$$A\left((j+1)h, t\right) = \exp\left[h\left(\hat{D} + \hat{N}\right)\right] A\left(jh, t\right), \tag{3.62}$$

where h is the step increment in spatial domain along fiber and j is the step number. In the split-step Fourier method, or first-order split-step method to be more specific, an iterative process is used to approximate 3.62 by treating $\hat{D}$ and $\hat{N}$ separately in sequence as

$$A\left((j+1)h, t\right) \approx \exp\left[h\hat{D}\right] \exp\left[h\hat{N}\right] A\left(jh, t\right). \tag{3.63}$$

This iterative process is carried on through the entire length of fiber step by step as demonstrated in Figure 3.14. For each step, to reduce the computation time, $\hat{D}$ is performed in frequency domain by applying Fourier transformation about T which is

$$\mathcal{F}\{\hat{D}\} = \mathcal{F}\left\{-\frac{\alpha}{2} - \frac{\mathrm{i}\beta_2}{2}\frac{\partial^2}{\partial T^2} + \frac{\beta_3}{6}\frac{\partial^3}{\partial T^3} + \cdots\right\} = -\frac{\alpha}{2} - \sum_{N=2}\beta_N\frac{\mathrm{i}^{N-1}}{2^{N-1}}\left(\mathrm{i}\omega\right)^N, \tag{3.64}$$

and the nonlinear operator $\hat{N}$ is realized using first-order exponential integrator and 4th order Runge-Kutta (RK4) method in time domain. The following 4 steps describe operations we take within a space interval Δh in order to compute the pulse propagation :

- ***Step 1:*** Apply nonlinear $\hat{N}$ in time domain by first-order exponential integrator and RK4;
- ***Step 2:*** Apply FFT onto $A(z, T)$ and get $A(z, \omega)$;
- ***Step 3:*** Apply linear $\hat{D}$ onto $A(z, \omega)$ in frequency domain;
- ***Step 4:*** Apply IFFT onto $A(z, \omega)$ and get $A(z, T)$ in time domain.

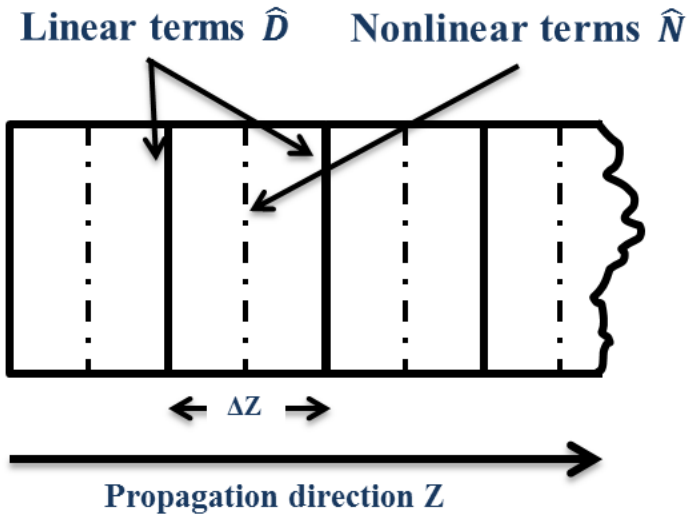

Figure 3.14: Schematic illustration of split-step Fourier method through fiber length.

Besides the first-order split-step method as shown above, the second order or symmetrized split-step method is also very often employed to solve NLSE as for higher accuracy consideration. There is not too much difference between these two methods but Equation 3.63 is approximated as

$$A\left((j+1)h,t\right) \approx \exp\left[\frac{h}{2}\hat{D}\right] \exp\left[h\hat{N}\right] \exp\left[\frac{h}{2}\hat{D}\right] A\left(jh,t\right). \tag{3.65}$$

And the way we treat linear operator $\hat{D}$ and nonlinear operator $\hat{N}$ is the same as we have demonstrated above.

We have seen many merits we can take from using split-step method to numerical solve NLSE. However, split-step Fourier method also has its limitations. For example, the split-step Fourier method can not trace both forward propagating and backward reflected waves simultaneously like what the time-domain finite difference method does. Also since the carrier frequency is eliminated or dropped when applying split-step Fourier method, split-step Fourier method might not be as accurate as finite-difference method under extreme cases to describe propagation behaviors of few-cycle or nearly single-cycle pulses.

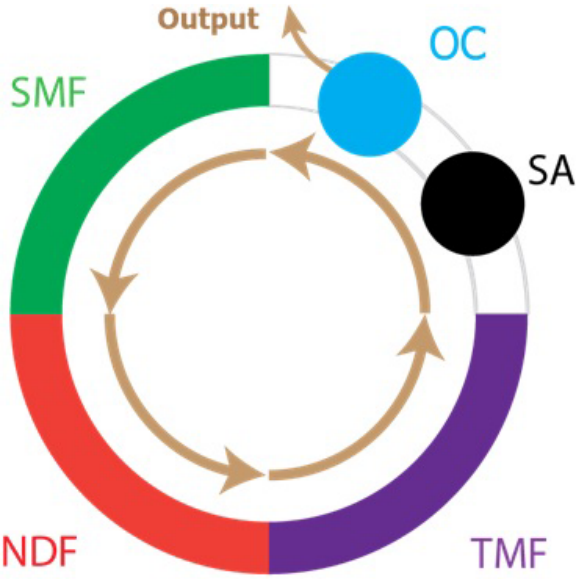

Figure 3.15: Model of the fiber laser used in our simulation. SMF, single mode fiber; NDF, normal dispersion fiber; SA, saturable absorber; OC, output coupler; and TDF, Thulium-doped fiber

3.5.2 Laser cavity simulation

With a proper numerical method to simulate in-fiber pulse propagation behaviors and the model for all individual optical components such as output couplers, filters, SAs, etc, we are ready to simulate a complete mode-locked fiber laser cavity by simply combining these individual optical elements in proper order as we experimentally construct our fiber laser cavity. To find a stable solution that our fiber laser cavities favor for, initially a pulse signal of arbitrary pulse shape is introduced into the fiber cavity to simulate noise signal. And this noise signal sequentially interacts with all optical components as shown in Figure 3.15. This simulation sequence is repeated for many round trips until the pulse has converged to some stable states and these stable states are the solutions that we search for. In the model, monitoring the change of pulse temporal duration, spectral width and per pulse energy at the output port for each round trip gives us the criteria to judge if a converged state has been achieved or not. If all these parameters reach certain stable values within predefined precision range, we will say stale mode-locked states are obtained in simulation. Also calculation and

monitoring of these parameters are very important and necessary for the simulation process itself. For examples, the consideration of gain saturation effect when pulse propagates in active gain fibers need us to know the pulse energy after each numerical setup.

To reach these converged stable states, usually 10 to 10,000 round trips need be completed in simulation, and this number shows strong dependence on the shape of initial noise signal, laser cavity configurations, etc. It also found numerical factors like step size and sampling rate also show impacts on the final results, so different values of these factors are tried in our simulation in order to void numerical error. Figure 3.16 shows the built numerical simulator for passively mode-locked fiber lasers with GUI and Figure 3.17 demonstrates a typical stable mode-locked pulse building-up from noise in simulation.

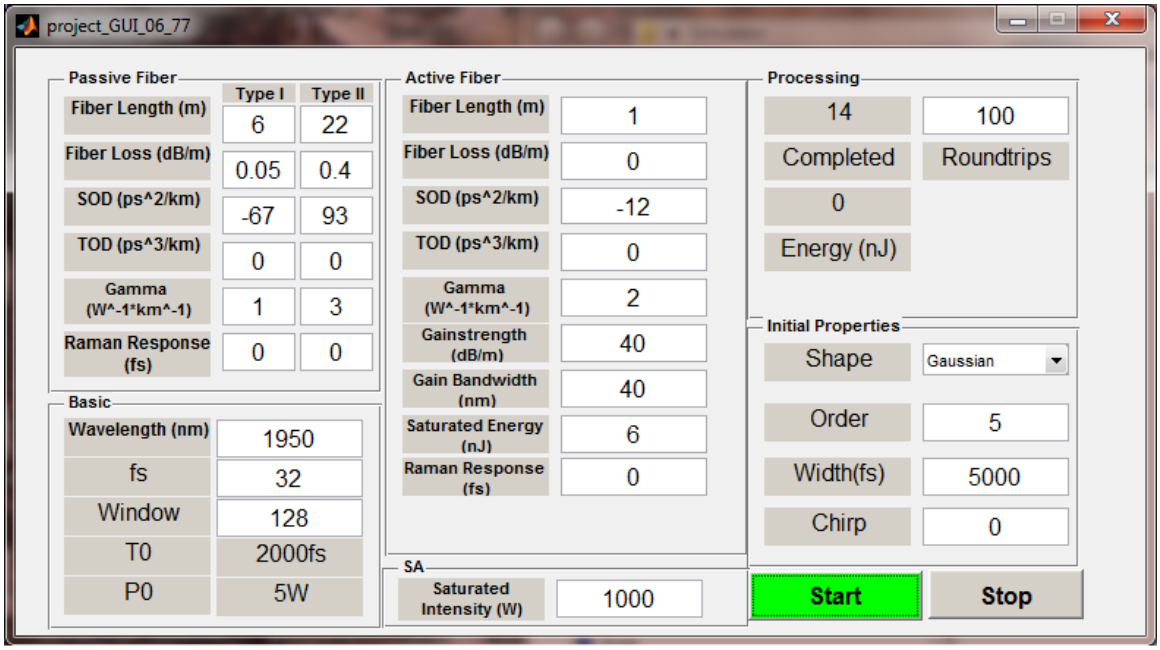

Figure 3.16: Numerical simulator for passively mode-locked fiber lasers with GUI.

Also it has been found from our simulation under certain circumstances, instead of converging to some stable values, these monitoring parameters are fluctuating around certain values. These states are referred as noise-like mode-locked pulses, which has also been confirmed in our experimental observations. Usually NLPs occur if the accumulated nonlinear

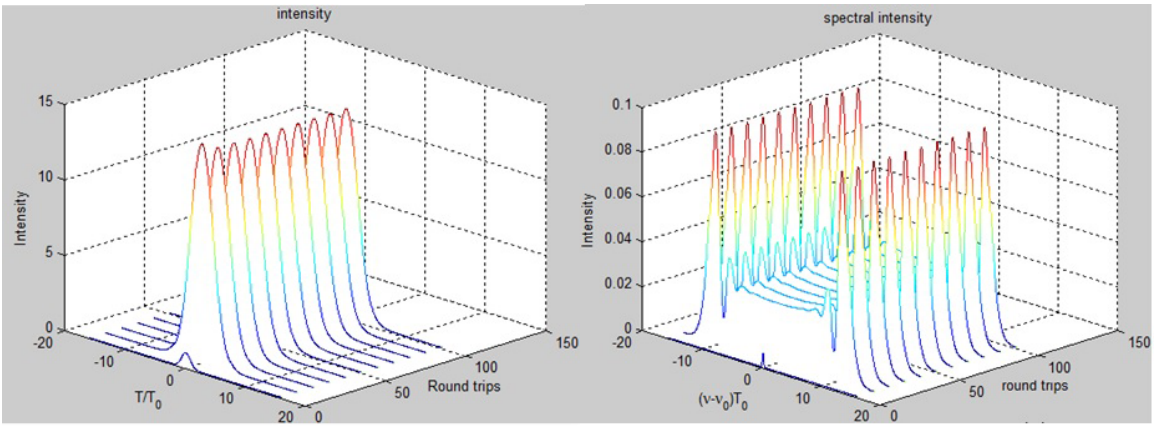

Figure 3.17: Typical stable mode-locked pulse building-up from noise in simulation.

phase shift is much greater than π, which is in Equation 3.66 :

$$\phi_{NL} = |U(0,T)|^2(L/L_{NL}) \gg \pi. \tag{3.66}$$

For more details about the differences between stale mode-locked pulses and NLPs especially about how to experimentally distinguish these two from autocorrelation measurement and RF analysis, please refer to Chapter 4 and 5.

4.0 ALL-FIBER MODE-LOCKED TDF LASER BY NONLINEAR POLARIZATION EVOLUTION

In this chapter, we demonstrate a NPE mode-locked TDF fiber laser with an all-fiber configuration. It is found the laser can work under two distinguished stable operational modes with either soliton or noise-like pulse output. Simulation is also done to consistently resembles our experimental observations for this all-fiber NPE laser system at $2\mu m$.

4.1 A BRIEF ABOUT NPE MODE-LOCKING IN FIBER LASERS

In 1995, L. E. Nelson, E. P. Ippen, and H. A. Haus reported the first solitary TDF fiber laser mode-locking passively with NPE mechanism and a intra-cavity spectral filter [24]. InGaAs quantum wells and carbon nanotube films have also been used as saturable absorbers for solitary mode-locked pulse generation at $1.9\mu m$[56, 57, 58]. Compared with other mode-locking techniques, NPE are usually employed for mode-locked short pulse generation because NPE can generally produce pulses with higher per pulse energy and the produced pulse quality and long-term stability are also better than those generated from graphene, CNTs and some other saturable absorbing materials. Up to now, NPE has been reported to successfully mode-lock fiber lasers at various wavelengths and different shaped mode-locked pulses at different energy levels have also been seen by the aid of NPE [59, 60, 61, 62, 24].

4.2 ALL-FIBER MODE-LOCKED TDF LASER WITH SOLITARY AND NOISE-LIKE OUTPUTS BY NPE

In this part, I demonstrate a Tm-doped all-fiber femtosecond laser oscillator at $1.9\mu m$ with compact design based on NPE. This design involves only fiber and fiber optical components, which greatly reduces system complexity and improves operational reliability. The schematic setup for the fiber ring oscillator is illustrated in Figure 4.1. The careful design of optical length and the dispersion in the fiber cavity allows best and stable mode-locked operations under both solitary and NLP modes. The active fiber is a 300-cm long single mode Tm-doped silica fiber with 5-μm core diameter and a numerical aperture of 0.23. The Tm dopant concentration in the fiber core is about 5 weight% with $60dB/m$ absorption rate of at $1.56\mu m$ which is measured by using a cut back method similar with that in Ref. [63]. The length of TDF is chosen to ensure maximum pumping efficiency for 1.5-μm pump sources. Two $1550nm/1900nm$ wavelength division multiplexing(WDM) couplers are used to couple pump light into the Tm-doped fiber as shown in Figure 4.1. The amplified spontaneous emission from two EDFAs fusion spliced to the gain fiber provides forward and backward pumping simultaneously to create a relatively uniform gain distribution. The pulse output is coupled out of the oscillator using a 10/90 coupler. Two compact in-line polarization controllers are used to control the polarization in the laser cavity. A customized polarization-sensitive isolator with 25% insertion power efficiency and over $50dB$ isolation at $2\mu m$ wavelength is fusion spliced between the two polarization controllers and thus enforces a clockwise unidirectional ring cavity. A second isolator for $2\mu m$ wavelength is also fusion spliced to the 10% output port to suppress back reflection into the cavity.

There is about 17-m of SMF-28e fiber in the laser cavity. The length of fiber was chosen and optimized to ensure stable mode-locking through the NPE process for both solitary and NLP operations. The anomalous dispersion of the SMF-28e fiber at $1.9\mu m$ was measured to be $-67ps^2/km$ by using a white-light interferometry technique [64, 65]. The dispersion measurements were performed using a TDF spontaneous emission as the light source like demonstrated before in Figure 2.9. The dispersion of TDF used in the experiment was estimated to be $-12ps^2/km$. The net dispersion in the cavity was calculated as $-1.31ps^2$.

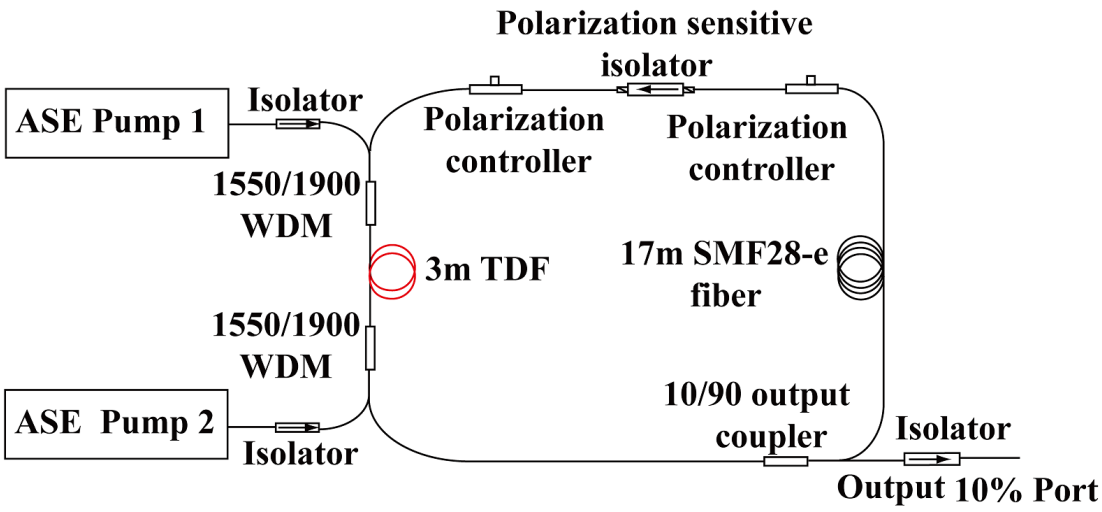

Figure 4.1: Scheme of TDF ring cavity, based on NPE[1].

The small amount of dispersion due to the optical isolator was neglected.

4.2.1 Soliton output

For a fiber ring cavity of anomalous dispersion like demonstrated right above, solitons are supported from mode-locking for which dispersion balancing between SPM and fiber's GVD is achieved within the pulse's profile as it circulates in fiber cavity. Mode-locking of the oscillator is passively achieved by NPE in the fiber ring. Pumped at a power of $240mW$, stable CW mode-locking can be achieved by carefully adjusting the polarization controllers. The pulse trains were measured using a 15-GHz fast detector and shown in Figure 4.2. The repetition rate is $9.78MHz$, which indicates that the oscillator operates with one pulse per round trip. Once mode-locking is achieved by the initial alignment of the polarization, the pulses are self-starting and do not require any tuning the polarization when the pump power is switched on. Figure 4.3 shows the typical optical spectrum of the mode-locked output measured with a resolution of $0.2nm$ on a linear scale when pumped at $240mW$. The central wavelength was $1982nm$ and the FWHM was $5.2nm$. The characteristic side-lobes due to the inference of dispersion waves indicate the laser was operating under soliton mode[66].

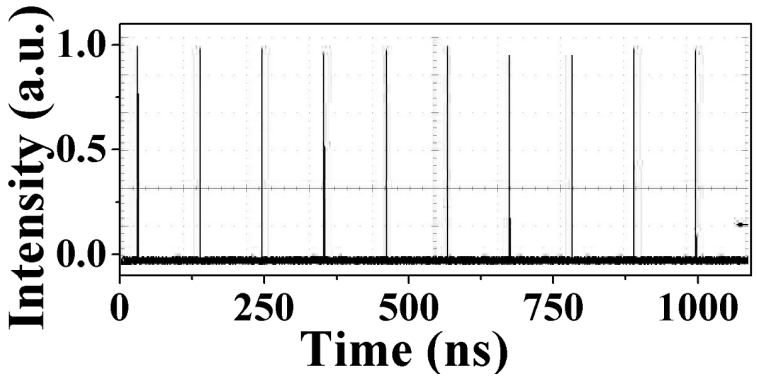

Figure 4.2: Pulse train by NPE at the fundamental repetition rate picked on oscilloscope[1].

A short scan-range interferometric autocorrelation measurement was performed to determine the pulse width. The second harmonic generated signal from 1.9-μm photons was picked by a silicon detector of high gain. The co-linear and intensity autocorrelation traces in Figure 4.4 give a pulse width of $770fs$ and well exhibit the 1:8 shoulders to peak ratio, for which we used deconvolution factor 0.647 based hyperbolic-secant pulse shape assumption.

Combined with the 5.2-nm FWHM centered at $1982nm$, it yields a 0.31 time bandwidth product(TBP). The small deviation from the 0.315 transform limit for a typical hyperbolic-secant soliton shape indicates that the pulses are almost transform limited. The average output power was measured to be $1.5mW$. Given the 9.78-MHz repetition rate, the pulse energy was about $0.15nJ$.

4.2.2 Noise-like operation

It is widely recognized that for such an all anomalous mode-locking scheme based on NPE without dispersion management in the cavity, the single solitary pulse energy is limited to be close to that of the soliton [67]. For our fiber laser setup under solitary mode locking, increasing the pump power merely pushes the system to operate under high harmonic repetition rates with comparable per pulse energy and spectrum, for which more than one pulses are generated per cavity round trip. However, as the pump power was ramped up to $400mW$, by

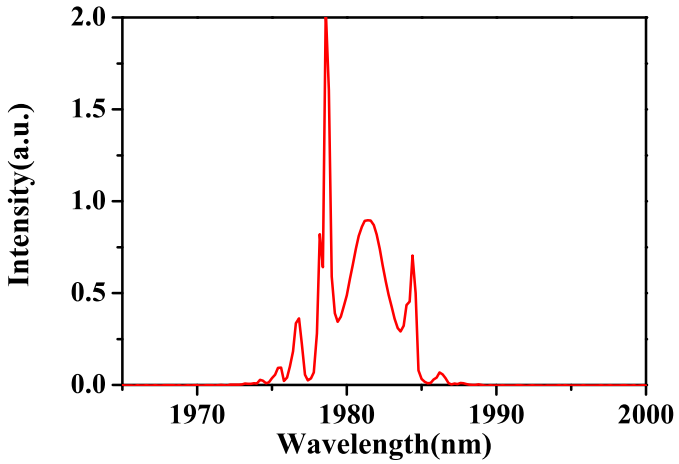

Figure 4.3: Typical spectrum of mode-locked soliton on linear scale by NPE[1].

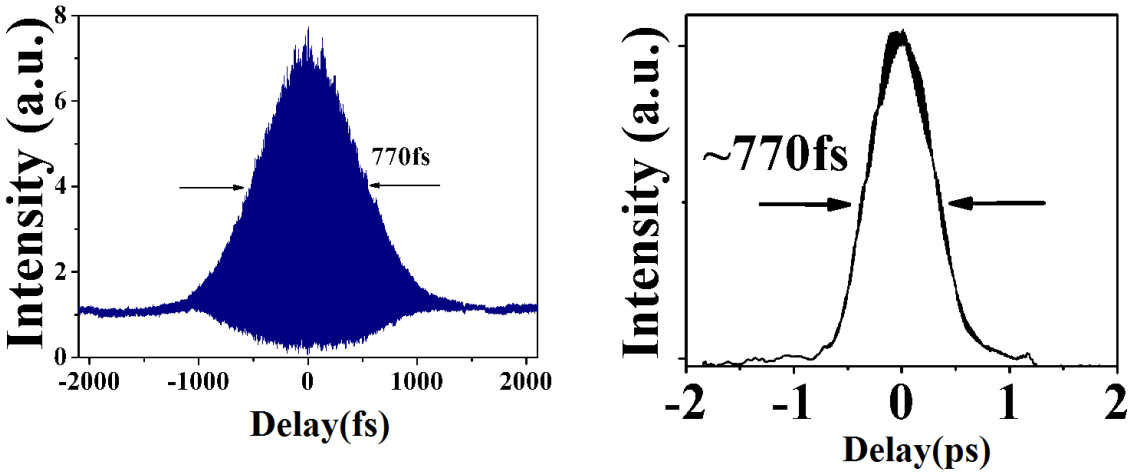

Figure 4.4: Interferometric autocorrelation(left) and intensity autocorrelation(right) traces of the solitary pulses [1].

slightly tuning two polarization controllers, stable mode-locked noise-like pulse trains with significantly different spectral and temporal features from soliton pulses were observed at

the fundamental repetition rate. The wide curve in Figure 4.5 shows this spectrum of the evolved new pulse trains.

30-mW output power was measured from the output port. Below this threshold, NLPs were also observed but not stable.For the evolved NLP trains, interferometric autocorrelation traces as the left part in Figure 4.6 revealed short pulse width but also complex temporal features. The pulse width was measured $260fs$ which was about transform-limited provided the 3-dB 15-nm spectrum width as shown in Figure 4.5. However, the shoulder to peak exhibits a 2:8 radio instead of that of 1:8 for the solitary mode-locking. This is because at a larger time scale, there exist bunch of short pulses whose width and power are randomly varying.

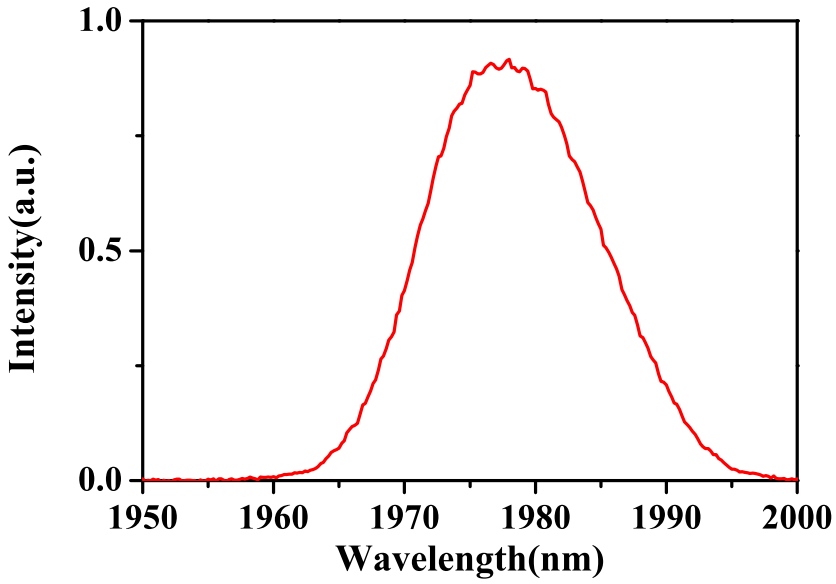

Figure 4.5: Typical spectrum of mode-locked noise-like output on linear scale by NPE[1].

A long-range intensity autocorrelator by employing a translational stage (Newport M-UTM100) was set to measure the NLPs. An example is shown in the right of Figure 4.6. The long-range intensity auto-correlation measurement reveals a narrow spike riding on a broad pedestal whose width could span from tens pico-seconds to several nano-seconds [68, 69]. Also the pedestal's width is found to increase as the pump power ramps up or as the cavity's

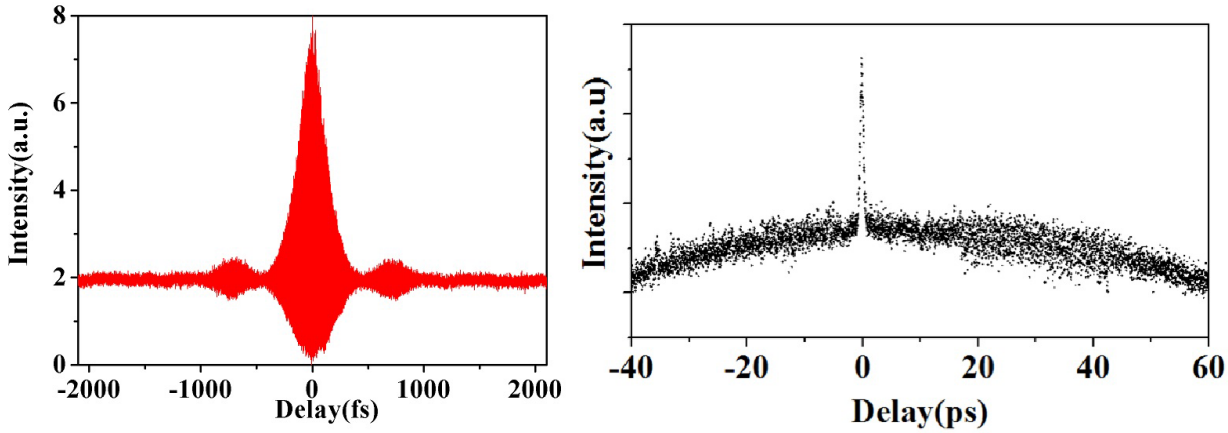

Figure 4.6: Interferometric autocorrelation(left) and intensity autocorrelation(right) traces of the noise-like pulses[1].

optical length is increased. Over 10-ns wide NLP bunch could be generated from 200m long ring cavity under 2W pump power observed from oscilloscope. The NLP's spectrum is comparable with Figure 4.5 but no stable soliton mode is observed for this case under different pump powers as this cavity is estimated to far exceed soliton's $8Z_0$ where Z_0 is the soliton's period[70].

4.3 SIMULATION OF TDF FIBER LASER MODE-LOCKED BY NPE

This part is the simulation of mode-locking by NPE, which is going to include the principal of mode-locking by NPE, numerical simulation procedures and results by solving CGLEs. The comparison and discussion with the experimental observations will be demonstrated at the end of this section.

4.3.1 Principal of mode-locking by NPE

Figure 4.7 illustrates the saturable absorbtion by nonlinear polarization evolution in fiber. Initially two beams of elliptically polarized light of the same polarization state but different

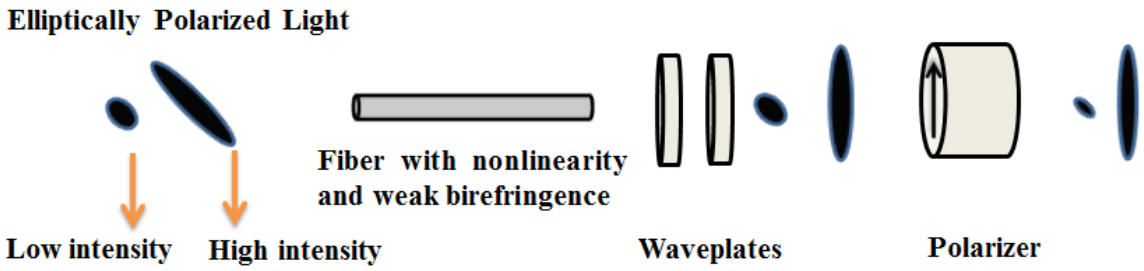

Figure 4.7: Illustration of saturable absorption by NPE.

intensity are sequentially injected into a piece of single-mode fiber. As the fiber like SMF-28e and many others takes nonlinearity and weak birefringence, the two beams would experience different nonlinear phase shifts along fiber's slow and fast axis and thus be of different polarization states after traveling through the fiber for which we assume the fiber are of weak linear birefringence. Then the polarization of the light after the fiber is tuned by a set of quarter and half waveplates so that the more intense light's polarization state favors the following polarizer placed after the waveplates and experiences less attenuation than that of the less intense light when passing through the polarizer. In this way, aftermath we create an artificial saturable absorber based on the nonlinear polarization evolution in fiber.

The first NPE mode-locked fiber laser was achieved by M. Hofer and his colleagues in 1991 from which 70-fs pulse of 1-nJ energy at 1.064μm was produced from neodymium glass fiber [71]. Since then, this mode-locked technique has been widely studied and become a matured method that is extensively applied for mode-locked fibers of various pulse energy at different wavelengths [16, 59, 24].

4.3.2 Numerical simulation and results

The CGLEs 4.1 are used to model our ring oscillator, in which the fiber is assumed linearly birefringent and U and V are the two polarization components along slow and fast axis respectively. $\Delta\beta$ is the wave number difference and 2δ is the group velocity difference between

these two polarizations. β_2 is the group velocity dispersion and γ is the fiber's nonlinearity, for which higher order dispersions and nonlinear effects like Raman response and self-steepening are neglected and could be included later on. $g = g_0 \cdot \exp(-E/E_{sat})$ is the saturated gain strength of the fiber and T_2 is the dipole relaxation time. The polarization controllers (PCs) and polarization sensitive isolator are presented by their Jones matrices[72]. The parameters we put into our simulation are as following: $\gamma = 1W^{-1}km^{-1}$; $\beta_2 = -67ps^2km^{-1}$(SMF-28e); $\beta_2 = -12ps^2km^{-1}$(TMF); gain bandwidth is $100nm$; $g_0 = 30dB/m$; the fiber beat length is $10m$ and the polarizer is 45° oriented between the slow and fast axes.

$$\begin{cases} \dfrac{\partial U}{\partial z} = \dfrac{\mathrm{i}\Delta\beta}{2}U - \delta\dfrac{\partial U}{\partial \tau} - \dfrac{\mathrm{i}}{2}(\beta_2 + \mathrm{i}gT_2^2)\dfrac{\partial^2 U}{\partial \tau^2} + \mathrm{i}\gamma(|U|^2 + \dfrac{2}{3}|V|^2)U + \dfrac{\mathrm{i}\gamma}{3}V^2U^* + \dfrac{g}{2}U \\ \dfrac{\partial V}{\partial z} = -\dfrac{\mathrm{i}\Delta\beta}{2}V + \delta\dfrac{\partial V}{\partial \tau} - \dfrac{\mathrm{i}}{2}(\beta_2 + \mathrm{i}gT_2^2)\dfrac{\partial^2 V}{\partial \tau^2} + \mathrm{i}\gamma(|V|^2 + \dfrac{2}{3}|U|^2)V + \dfrac{\mathrm{i}\gamma}{3}U^2V^* + \dfrac{g}{2}V \end{cases} \tag{4.1}$$

We numerically solve CGLEs 4.1 by split-step Fourier propagation method combined with fourth order Runge-Kutta.Initially, a relatively long ripple of low intensity is introduced into the cavity to simulate weak noise and then this noise periodically evolutes and interacts with all the components in the cavity as governed basically by CGLEs. By tuning the linear phase delay induced by two PCs, stable mode-locked pulse trains favoring the cavity's configurations are obtained as shown in Figure 4.8. The left shows the temporal evolution and for this depicted case, stable mode-locked solitary pulses are obtained after about 30 simulated cavity round trips for which E_{sat} is set to be $0.1nJ$. The right is the spectrum of typical soliton pulses.

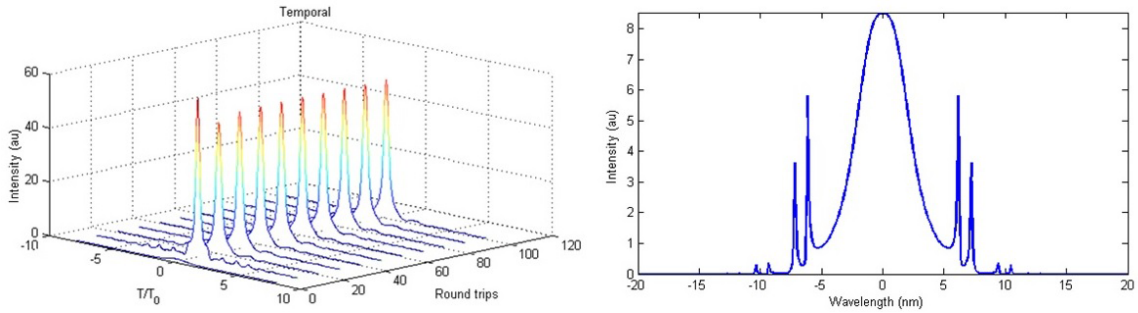

Figure 4.8: Typical simulated soliton evolution(left) and spectrum(right) by NPE with $T_0 = 2ps$, $\lambda_0 = 1950nm$.

As discussed above, for an mode-locking ring cavity with all anomalous dispersion, the generated mode-locked single pulse energy is limited to be close to that of the soliton pulse. Also as reported and observed, under higher pump power, noise-like pulse trains at the cavity fundamental repetition rate can be produced for which multiple short pulses of randomly varying phase and width exist within a relatively broader time window. To simulate the NLPs generation in our setup, E_{sat} is increased to $1nJ$ in response to the increased pump power and also $\pi/20$ linear phase delay difference by the PCs is imposed to simulate NL operations as experimentally a slight tuning of the PCs from the soliton operation is needed for stable NL operation. The simulated results of the NL operation in demonstrated in Figure 4.9. The left is the temporal evolution in fiber cavity. Even though the NLP bundles vary in phase and temporal profile trip by trip as they circulate, statically they show long-term stability in term of the spanning time range and optical spectrum. The right is the averaged spectrum of the output NLPs which is as wide as $\sim 20nm$ and this results is well comparable with our experimental observation. More over, simulation also shows that The exact temporal spanning range of NLP bundle varies with the pump power, which could be as broad as several hundred of picoseconds to several nanoseconds under strong pumping.

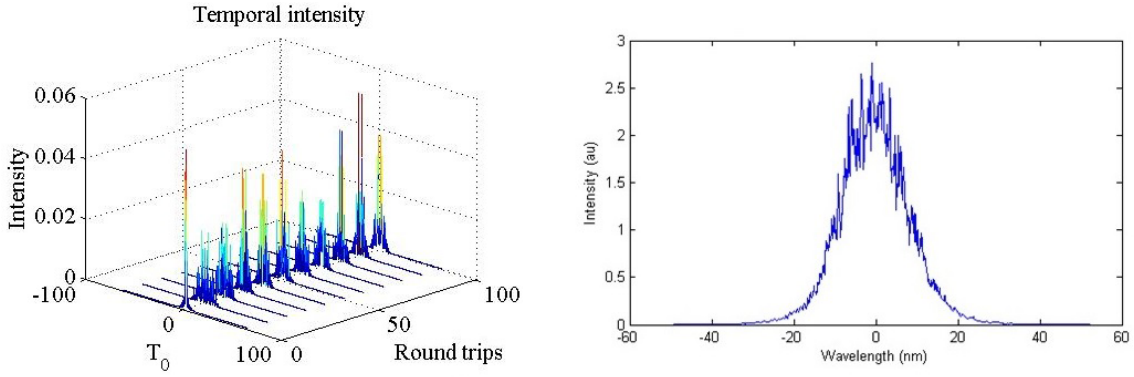

Figure 4.9: Typical simulated NLPs evolution(left) and spectrum(right) by NPE with $T_0 = 2ps$, $\lambda_0 = 1950nm$.

5.0 $2\mu m$ SOLITON PULSES BY OPTICALLY DEPOSITED GRAPHENE SATURABLE ABSORBER

Other than to use NPE scheme for ultrashort mode-locked pulse generation in fiber, passively mode-locked fiber and bulk lasers based on saturable absorbers have also been well developed and widely used in commercially available systems[73, 74, 75]. The saturable absorbers serving as the passive mode-lockers in different forms of laser cavities includes SESAMs, GSAs, SWCNT SAs, topological insulators and etc. These new forms of saturable absorbers are generally considered as part of innovative mode-locking techniques in laser field and this thesis. Specially, compared to SESAMs and others, carbon nanomaterials based SAs(GSAs and SWCNT SAs) own many desirable advantages and unique features as they can serve as broadband and cost effective mode-lockers[76, 77, 78].

In this chapter, we integrate graphene with fiber optics for ultra-short pulse generation and demonstrate a 2-μm all-fiber GSA passively mode-locked TDF ring oscillator, for which the GSA is fabricated by optically depositing few layers graphene micro-sheets onto the core area of the single mode fiber's end tip. The typical nonlinear transmittance curve of the fabricated graphene saturable absorber at $2\mu m$ is also characterized and simulation by numerically method for ultra-short pulse generation is demonstrated.

5.1 PRINCIPAL OF SATURABLE ABSORPTION IN GRAPHENE

In this section, at first it is going to brief graphene material and its application as optical saturable absorbers for various wavelengths. The physics behind graphene saturable absorption is then discussed as its following.

5.1.1 Brief about graphene

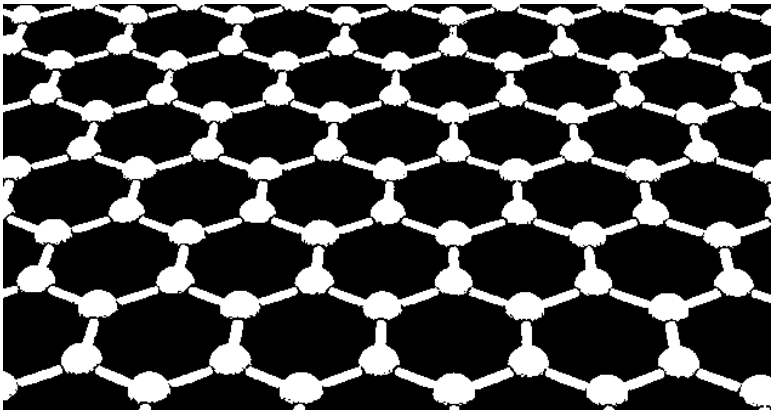

Figure 5.1: Graphene as a monolayer of carbon atoms arranged in a two-dimensional honeycomb pattern.

Graphene forms by a monolayer of carbon atoms arranged in a two-dimensional honeycomb pattern as demonstrated in Figure 5.1. All the chemical bonds that connects carbon atoms in graphene are sp^2 carbon-carbon bonds, which are the most firm chemical bonds found so far, and this is believed to be the main reason why graphene takes excellent mechanical strength [79]. Other than excellent mechanical strength, graphene also possesses a unique electronic band structure. The band structure of graphene was first calculated by Phillip Russel Wallace in 1947 when he tried to obtain the band structure of graphite [80]. From his theory it was found for graphene, the valence band and conduction band connect at six different points that have the same energy and these points are named " K points" or "Dirac points" and labeled from K^1 to K^6. Near these K points, the relationship between the electron energy and momentum(dispersion relationship) can be well approximated by a linear function. Figure 5.2 shows this linear relationship near one of these Dirac point and this linear band structure is called Dirac cone structure [81, 82]. The feature that valence band and conduction band touch and do not overlap is very unique, and for this reason, graphene is also called as an representative "zero-bandgap" semiconductor. However, this form of specially arranged carbon material does not draw tremendous research interests until the groundbreaking "discovering and isolating a single free-standing atomic layer of carbon and elucidating its remarkable electronic properties" by Andre Geim and

Kostya Novoselov in 2004 using micromechanical cleavage technique [83]. Ever since this achievement, graphene have been subjected to extensive research studies and meanwhile a lot of attempts in seeking applications for this new material have also been made. Among these attempts, many people and research groups have found graphene possesses excellent optical saturable absorption prosperities over a wide wavelength range [84, 85] and different forms of passively mode-locked lasers with graphene-base materials as the mode-lockers have also been reported and demonstrated.

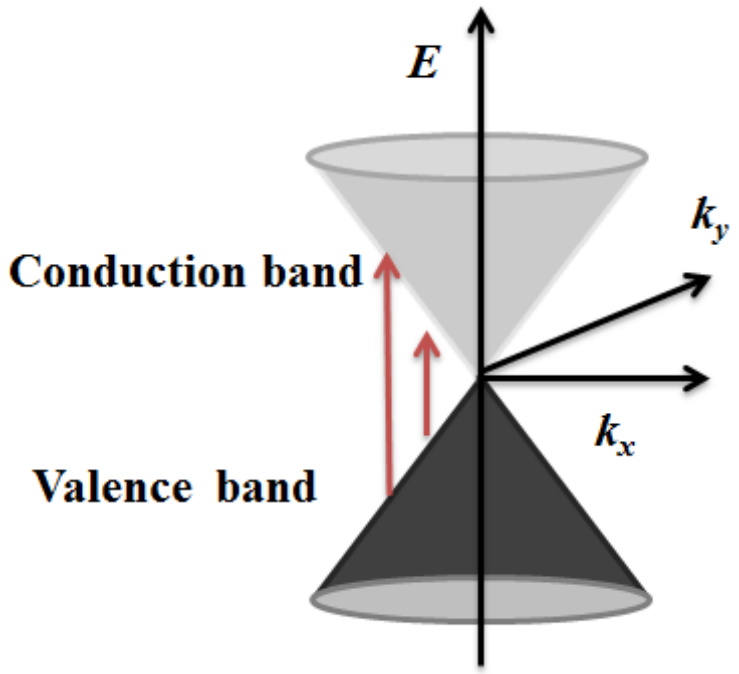

Figure 5.2: Graphene's Dirac-cone band structure near its Dirac point.

5.1.2 Graphene's saturable absorption under intense excitation

Though formed by a single layer of carbon atoms, graphene is found to strongly absorb incident light. It was reported, for a single-layer graphene, the calculated absorption is $\pi\alpha \sim 2.3\%$ where α is the fine structure constant ($\alpha = e^2/\hbar c$) and this value is not related with any material science [86]. Also because of the zero band-gap and linear energy-momentum

dispersion relation, this absorption is independent of wavelength and thus makes graphene suitable to work and absorb under a wide bandwidth from visible to mid-infrared. However, this absorption ∼2.3% is only for the case of low-intensity excitation. As for saturable absorption, inter-band and intra-band precesses and interactions of electrons and photons in graphene under intense excitation should be interrogated which is discussed as the following.

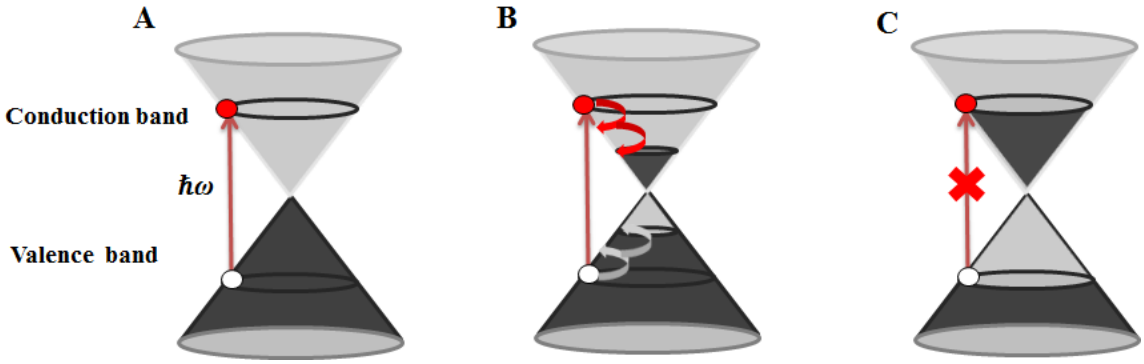

Figure 5.3: Electron and light interaction in graphene (A) A photon of energy $E = \hbar\omega$ excites an electron at $-E/2$ from valence band to $+E/2$ at conduction band; (B) Photogenerated carriers thermalize and cool down to form an equilibrium electron and hole distribution via *e-e* and *e-ph* scattering and electron-hole recombination (C)Under intense excitation, the photogenerated carriers fill up states below $E/2$ and cease further light absorption in graphene.

The physics and saturable functionality for single-layer and few-layer graphene as saturable absorber for ultrafast pulsed lasers is interrogated and discussed in Ref [87]. Like depicted in Figure 5.3, Figure 5.3A is the excitation process as a photon of energy $E = \hbar\omega$ is absorbed in singe-layer graphene, for which an electron is moved up to the corresponding energy level in the conduction band from the valence band meanwhile a hole is produced in the valence band. Shortly after the excitation, these hot electrons redistribute via intra-band electron-electron *e-e* scattering and electron-phonon *e-ph* scattering, and transport from the surface into the bulk as in Figure 5.3B. Experiments reveal the *e-e* scattering happens very quickly within 10-150fs while the *e-ph* process is with a timescale of ∼1ps [88, 89, 90, 91]. Meanwhile in the valence band similar intra-band processes apply to the holes. After ∼1ps, electron-hole recombination through the Dirac point will dominate the process until the thermal equilibrium electron and hole distribution is restored. However, under intense optical

excitation that the supposed photo-generated carriers are much larger than the graphene's intrinsic electron and hole carrier density $\sim 8 \times 10^{10} cm^{-2}$ [92] and thus fill up the conduction and valence bands below E, this effect actually ceases further light absorption and produces absorption saturation as a result of Pauli blocking process [93].

5.2 GSAs FABRICATION BY OPTICAL DEPOSITION

Single-layer and few-layer graphene can be synthesized and obtained by using different methods, which can generally be divided into two classes: physical exfoliation methods and chemical synthesis methods. For physical exfoliation, the two mostly utilized methods are Scotch-tape method and liquid-phase exfoliation method. For Scotch-tape method, it is to simply use adhesive tape to repeatedly split graphite flakes into thinner and thinner pieces, and few-layer and single-layer graphene can then be obtained and transferred to other substrates. For liquid-phase exfoliation method, graphene flakes are firstly dispersed in solvent, then ultrasonically bathed and lastly centrifuged to develop dispersed solution of small pieces of few-layer and single-layer graphene. Surfactants are usually also added into solvent to assist the exfoliation. On the other side, the most promising and successful chemical synthesis method for few-layer and single-layer graphene fabrication is the chemical vapor deposition(CVD) method[94].

Of these different graphene fabrication methods as mentioned above, each of them has its advantages and also shortcomings when compared to others. For instance, Scotch-tape method can produce the best samples in terms of purity and size, but not possible to be applied into mass production. Mass production of few-layer graphene can be achieved by liquid-phase method, but the obtained graphene samples' size is small and the layers' number can not be precisely controlled. Mass production of large-area graphene samples is also possible by CVD chemical method, but the expense and investment on required equipment are usually not affordable for many laboratories.

5.2.1 Development of dispersed few-layer graphene solution

In this part, we adopted a liquid-phase exfoliation method to obtain few-layer graphene samples as it is found nonlinear photonic applications are usually not very sensitive to the size of developed graphene flakes [3] which has also been confirmed by our experimental trials. The graphene solution development procedures are described as follows.

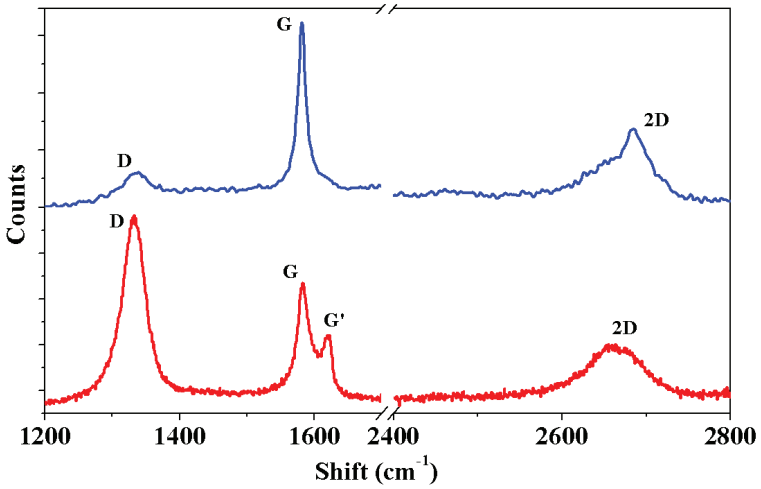

Figure 5.4: Raman spectra for the starting graphite flakes (top) and the derived graphene dispersion solution (bottom).

A modified ultrasonic exfoliation method [95] is employed to prepare high concentration graphene dispersion from graphite flakes. 3% wt. graphite flakes were firstly mortared and dispersed in N-dimethylformaminde (DMF) and 1-hexyl-3-methyl-imidazolium hexafluorophosphate (HMIH) mixed solvent and ultrasonically exfoliated for 48 hours. The dispersion was then centrifuged for 30 minutes at 10,000 rpm. The top portion of homogenously transparent liquid with lightly grey color contains graphene. They were collected for further process. Figure 5.4 shows the Raman spectra for the starting graphite flake (top) and the derived dispersion solution after the process (bottom). The Raman spectra were acquired using 633-nm laser excitation. The higher D/G band intensity ratio in the dispersion solution suggests the breakdown of the graphite flake after the process. The relative shift of the 2D peak and the ratio of 2D/G peaks indicate the formation of single-layer and few-layer graphene sheets in the dispersion solution. It was reported that this process can produce the

dispersion solution containing 10% mono-layer graphene sheets and up to 80% of few-layer graphene sheet containing less than five graphene layers[95]. Both single-layer and few-layer graphene can be used as efficient optical saturable absorbers.

5.2.2 GSAs fabrication by optical deposition and function characterization

After the derivation of suspended few-layer graphene solution, Graphene suspended in liquid was deposited onto end end-tips of single mode fibers using an optical trapping approach shown in the left of Figure 5.5 [96]. An EDFA spontaneous emission light source ($200mW, 1.5\mu m$) was used to trap and to deposit graphene films onto the fiber tips. Once the graphene film is optically trapped and deposited onto the fiber tip by the optical deposition method, an enhanced back-reflection can be registered by the OSA to confirm the deposition, which is because the refractive index of graphene ∼3 is larger than that of DMF liquid ∼1.5. This is a very effective approach for the graphene deposition. The right of Figure 5.5 shows the fiber end face under microscope after the optical deposition of graphene film. Layers of graphene were coated onto the fiber's core area. The graphene-coated fiber was then connected with a fiber cable using a fiber connecting sleeve and inserted into fiber cavity as a GSA. Thus it finishes the GSA fabrication process.

The nonlinear transmittance of the fabricated GSA is the characterized by using an amplified mode-locked laser operated at central wavelength of $1945nm$ with 12.8-MHz repetition rate, ∼2-ps temporal duration as the pump. The typical normalized transmittance curve at $1945nm$ as the function of average incident power is shown in Figure 5.6. The transmittance is consistently around 62% when the average pump power is below $3mW$ and increases by ∼4% as the pump rises to $6mW$ due to the absorption saturation.

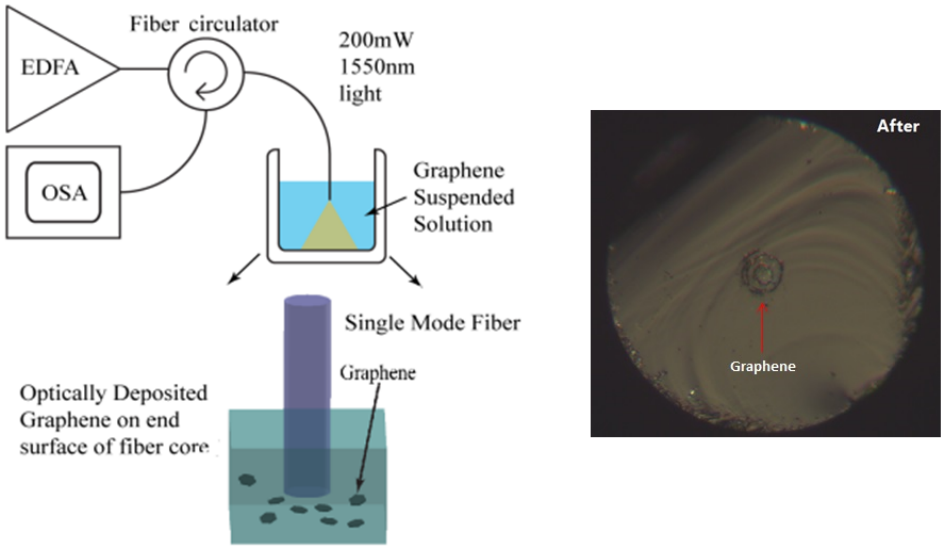

Figure 5.5: Scheme of optical deposition of graphene film on to the fiber tip(left) and the fiber end face under microscope after the optical deposition(right).

5.3 PASSIVELY MODE-LOCKED ALL-FIBER TDF RING LASER BY OPTICALLY DEPOSITED GSA

5.3.1 Configuration of TDF ring laser by GSA

The fabricated GSA was inserted into an TDF ring cavity as depicted in Figure 5.7. The active fiber in the laser cavity is a piece of 35-cm long single mode Tm-doped silica fiber with 5-μm core diameter and the numerical aperture is 0.23. A 1550-nm/1900-nm WDM couplers is used to couple pump light into the cavity. An amplified spontaneous emission light source from an EDFA is fusion spliced to the WDM to provide forward pumping. The laser output from the oscillator is coupled out through the 10% port of a 10/90 output coupler. A polarization insensitive isolator is fusion spliced into the cavity to enforce a counterclockwise unidirectional ring. A second isolator at 2-μm wavelength is also fusion spliced to the output port to suppress back reflection into the cavity. An in-line polarization controller (PC) is inserted into the cavity to examine the polarization effects on the mode-locking operation. It was intended to balance the intrinsic weak birefringence of single-mode fibers used to

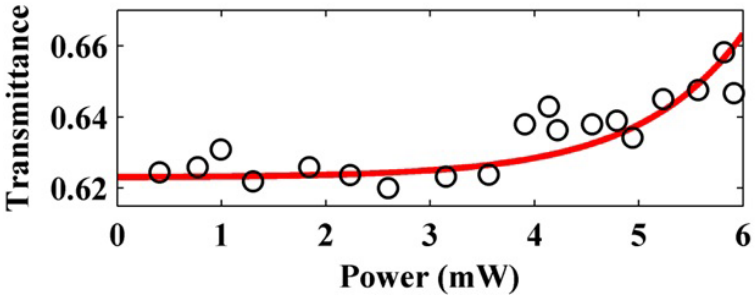

Figure 5.6: : Typical GSA normalized transmittance curve at $1945nm$ as a function of average incident power. Pump of 12.8-MHz repetition rate, ∼2-ps temporal duration.

construct the laser cavity. However, our experimental results showed that the mode-locking operation is virtually independent of the tuned position of the PC, suggesting that the PC is not needed. The laser cavity shown in 5.7 consists of 11.5-m of SMF-28e fiber. SMF-28e fiber takes anomalous dispersion at $1.9\mu m$ and the value of is dispersion is $-67ps^2/km$ as measured before by using a white-light interferometry technique. The dispersion of the TDF used in the experiment is estimated to be $-12ps^2/km$. The net dispersion in the cavity is calculated as $-0.77ps^2$. The small amount of dispersion due to other optical components is neglected.

5.3.2 Soliton pulses from TDF ring laser by GSA and measurements

Stable CW mode-locking of the oscillator is self-started as the pump goes up to $130mW$. Figure 5.8 shows a typical optical spectrum of the mode-locked output with a 0.1-nm resolution under 130-mW pumping power. The central wavelength is $1953.3nm$ and the FWHM is $2.2nm$. Strong Kelly side-lobes due to the interference of dispersion waves are clearly indicative of the solitary operation of the laser[66]. The mode-locking operation is not affected by tuning the position of the polarization controller, which confirms that the nonlinear amplitude modulation in the ring cavity is due to the graphene saturable absorption other than any unbalanced NPE effect. The pulse width, which was determined by a lab-built intensity autocorrelator, is shown in Figure 5.9. The autocorrelation measurement yields

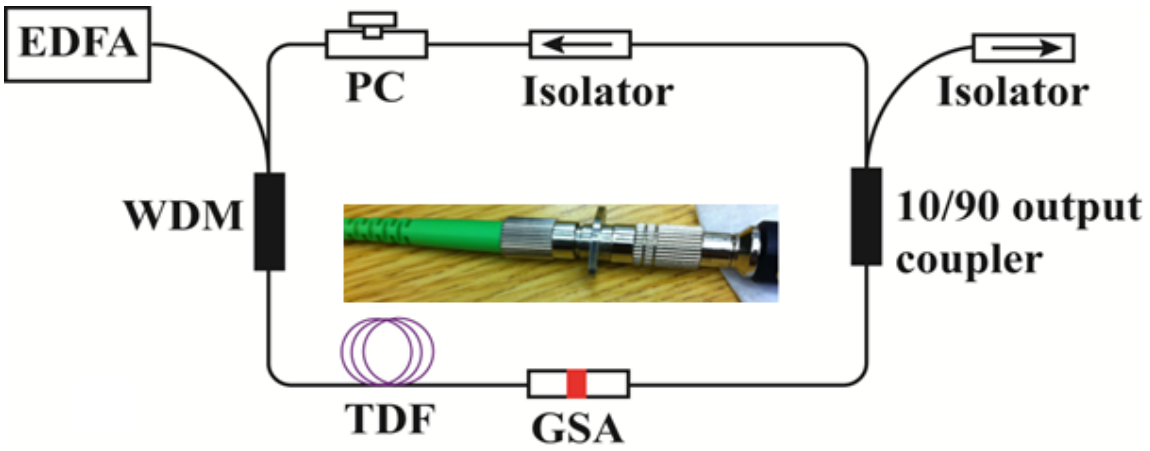

Figure 5.7: Scheme of the TDF ring cavity based on the fabricated GSA, and fabricated GSA photo as the inset: graphene sandwiched between two fiber connectors [2].

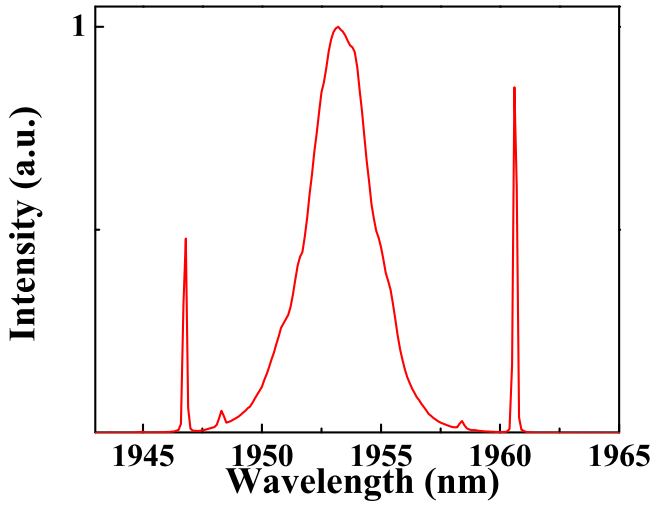

Figure 5.8: Typical spectrum of the mode-locked laser on linear scale under 130-mW pump [2].

2.1-ps FWHM pulse width assuming a hyperbolic-secant soliton pulse shape. Considering the 2.2-nm 3-dB bandwidth, the TBP is calculated as 0.363, which is slightly larger than the

transform-limit value 0.315. A 7-GHz fast InGaAs detector was used to measure the radio frequency(RF) characteristics of the mode-locked operation. High resolution RF spectrum of the graphene mode-locked pulse trains at the fundamental repetition rate is shown in Figure 5.10. The center frequency is 16.937MHz, which is consistent of the fundamental repetition

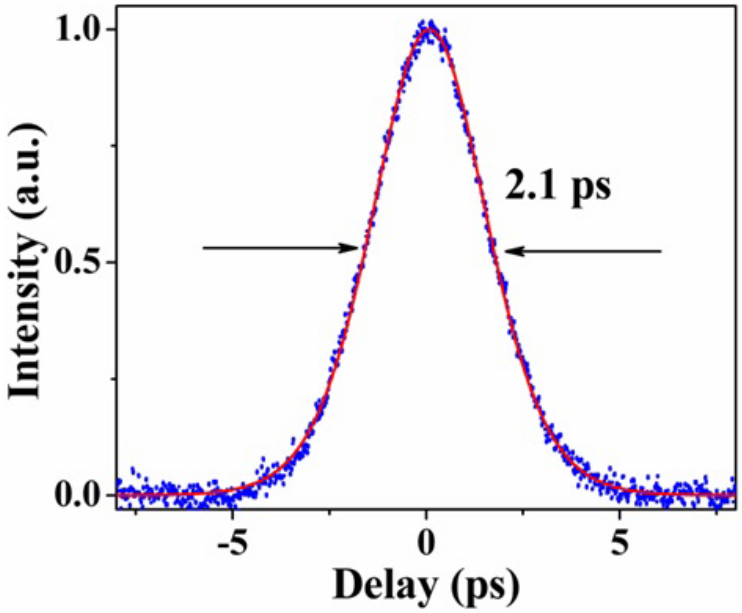

Figure 5.9: Intensity autocorrelation trace of GSA mode-locked TDF laser with soliton output and the red line is the fitted curve.

rate of the cavity. This confirms that one pulse is produced per round trip. The signal to noise ratio (SNR) is as high as 50dB and the 3-dB width of the RF spectrum is sub the RF resolution of 20Hz. Wide range RF spectrum from 0 to 2GHz is shown as the Figure 5.11. These measurement results indicate low time jittering of the pulse trains. The average output power from the 10% output port is measured as 1.41mW. Given 16.937-MHz repetition rate, the per-pulse energy is about 80pJ. It also has been tested that this thulium-doped fiber laser is capable of long-term operation under mode-locked working mode.

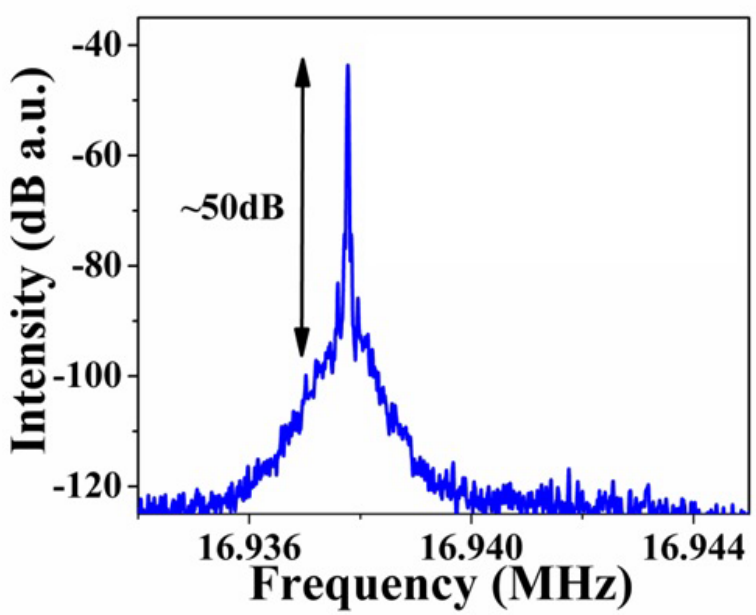

Figure 5.10: RF spectrum around the fundamental repletion rate.

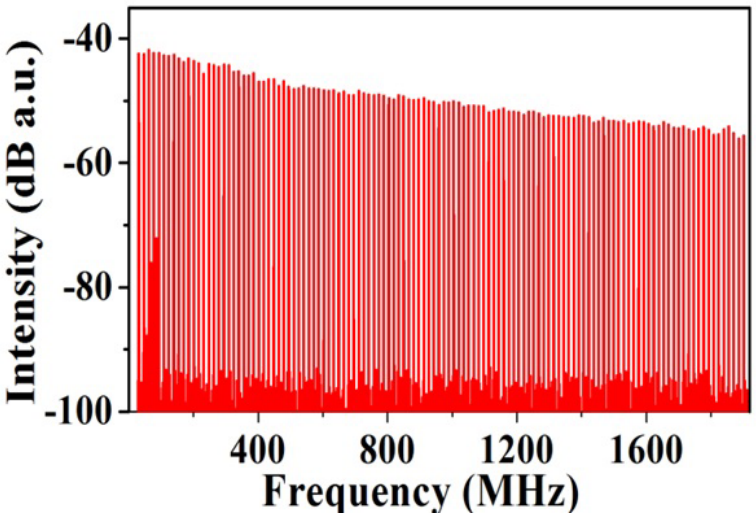

Figure 5.11: RF spectrum from 0 to $2GHz$.

5.4 NUMERICAL SIMULATION OF MODE-LOCKED TDF LASER BY GSA

GLE equation 3.56 is used to model our GSA-assisting mode-locked ring oscillator. β_2 is the fiber's second order dispersion, γ is the fiber's nonlinearity, $g = g_0 \exp(-E/E_{sat})$ is the saturated gain strength of the fiber and T_2 is the dipole relaxation time which decides the active fiber's gain spectrum width, in which we omit any birefringent effect in our demonstrated all fiber laser cavity. Table 5.1 lists the parameters of the fibers and optical components we used in our simulation.

Table 5.1: Fibers' and optical components' parameters used in simulation

Parts	Length(m)	$\beta_2(ps^2/km)$	$\gamma(W^{-1}km^{-1})$	Loss(dB)
SMF-28e	11.5	-67	1	-
TDF	0.35	-12	2	-
WDM	-	-	-	0.46
Isolator	-	-	-	0.96
Output coupler	-	-	-	0.46
Parts	Gain width(nm)	$g_0(dB/m)$	$E_{SAT}(nJ)$	Loss(dB)
TDF	40	30	0.1	-

To closely resemble and simulate the passive mode-locking by lab-fabricated GSA, the GSA's transmittance T in response with light intensity I at $1.9\mu m$ is modeled as a nonlinear curve as shown in Formula 5.1, and four involved coefficients $ABCD$ are extracted from the characterized data as shown above in Figure 5.6.

$$T(I) = \frac{A}{1 + B \cdot e^{-C \cdot I}} + D \tag{5.1}$$

for which $A = 0.037$, $B = 100$, $C = 4{\times}10^{-3} area/W$ and $D = 0.623$. We numerically solve GLE equation by split-step Fourier propagation method combined with fourth order Runge-Kutta. Initially, a relatively long ripple of small intensity is introduced into the cavity to

simulate weak noise and then this noise periodically propagates and interacts with all the components in the cavity as governed basically by GLE equation.

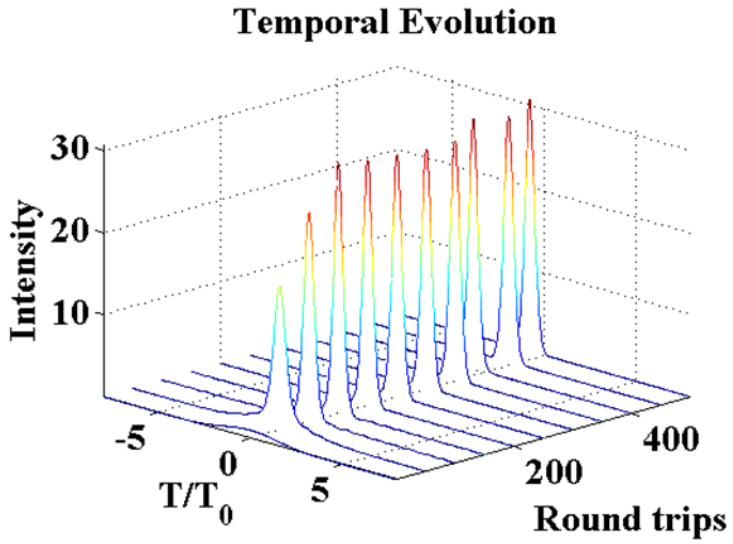

Figure 5.12: Simulated pulse temporal evolution for soliton generation by fabricated GSA.

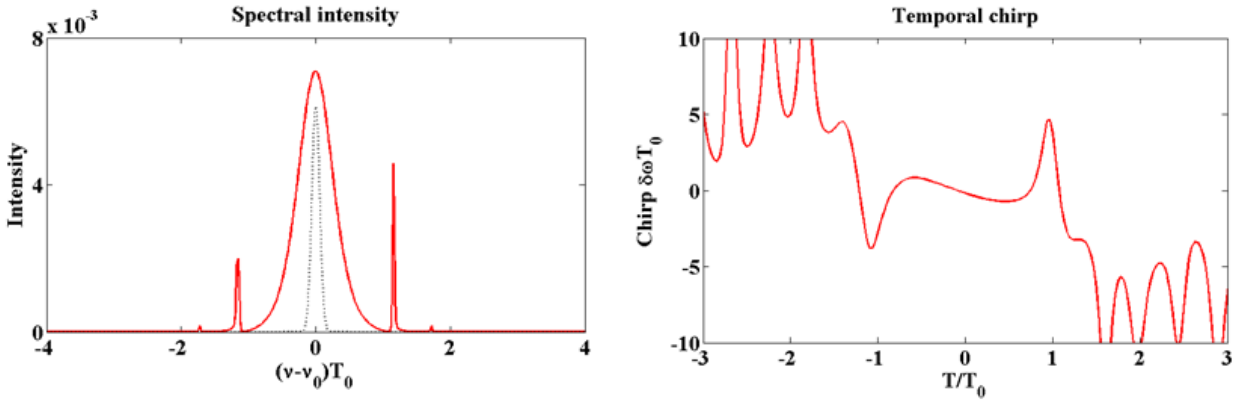

Figure 5.13: Spectrum of the generated soliton (solid) and initial noise (dashed) (left)and phase of the generated soliton(right) by simulation.

The simulated results are demonstrated as follows. Figure 5.12 is the temporal evolution as the initial light propagates; as seen, stable self-consistent mode-locked pulses are

produced after about 100 simulated round trips. In the left of Figure 5.13, the solid curve is the spectrum of the simulated stable GSA mode-lock soliton pulse and the dashed line is the spectrum of the initial 4-ps Gaussian pulse. The right of Figure 5.13 tell the phase information of the generated pulse and we can see there is no significant chirping under the envelope of the generated pulse, which agrees with our experimental observation of almost transform-limit pulse generation from the auto-correlation measurement results.

5.5 SUMMARY AND DISCUSSION

In this above section, we integrate graphene with fiber optics for ultra-short pulse generation and demonstrate a 2-μm all-fiber GSA passively mode-locked TDF ring oscillator. The GSA is fabricated by optically depositing few layers graphene micro-sheets onto the core area of the single mode fiber's end tip. The typical nonlinear transmittance curve of the fabricated graphene saturable absorber at $2\mu m$ is also characterized and simulation by numerically solving nonlinear GLE equation for ultra-short pulse generation is demonstrated which agrees with our experimental observations.

Numerical simulation also reveals highly chirped dissipative pulses with larger pulse energy could also be supported and produced by GSAs if dispersion control is brought into cavity. However, it is found from our experiments the GSAs fabricated by the optical deposition methods in Section 5.2 suffers from a relatively low damage threshold and they tends lose saturable absorbing functionality under high pump power, which makes them not suitable for high-energy dissipative pulse generation by implicating dispersion management inside laser cavity. Other fabrication mothers to obtain graphene-based SAs with higher damage threshold need to be addressed in future studies.

6.0 MODE-LOCKED TDF LASER BY SWCNTs AT NORMAL DISPERSION

The 1-D multi-wall and single-wall carbon nanotubes(CNTs) were discovered by S. Iijima in 1991 [97] and 1993[98] respectively. Like single-layer and few-layer graphene, CNTs as the 1-D rolled graphene with unique band structure also show to exhibit optical saturable absorbing properties under intense light excitation and has been studied and successfully mode-locked different lasers at various wavelengths [99, 100, 57]. Figure 6.1A is the SWCNTs formed by rolling single-layer graphene sheet.Like graphene, SWCNTs also exhibit wide saturable absorption bandwidth, which makes it in favor suitable for mid-IR ultrafast photonic applications at $2\mu m$ and beyond [101]. Particularly, recent studies also reveal that SWCNTs has higher optical damage threshold than some other SAs [74]. This trait makes SWCNTs an excellent candidate for ultrafast fiber laser with high pulse energy. SWCNTs based SAs have been reported to successfully generate dissipative solitons for 1-μm and 1.5-μm fiber lasers respectively [57, 102, 103].

In this chapter, we demonstrate a 1.9-μm passively mode-locked dissipative TDF ring oscillator by using optically deposited SWCNTs on the fiber end tip as the saturable absorber (SA). Carefully selected segments of special fiber of measured normal dispersion (NDF) is added to the cavity to compensate the anomalous dispersion from other fibers and create net normal dispersion in the cavity at $1.9\mu m$.

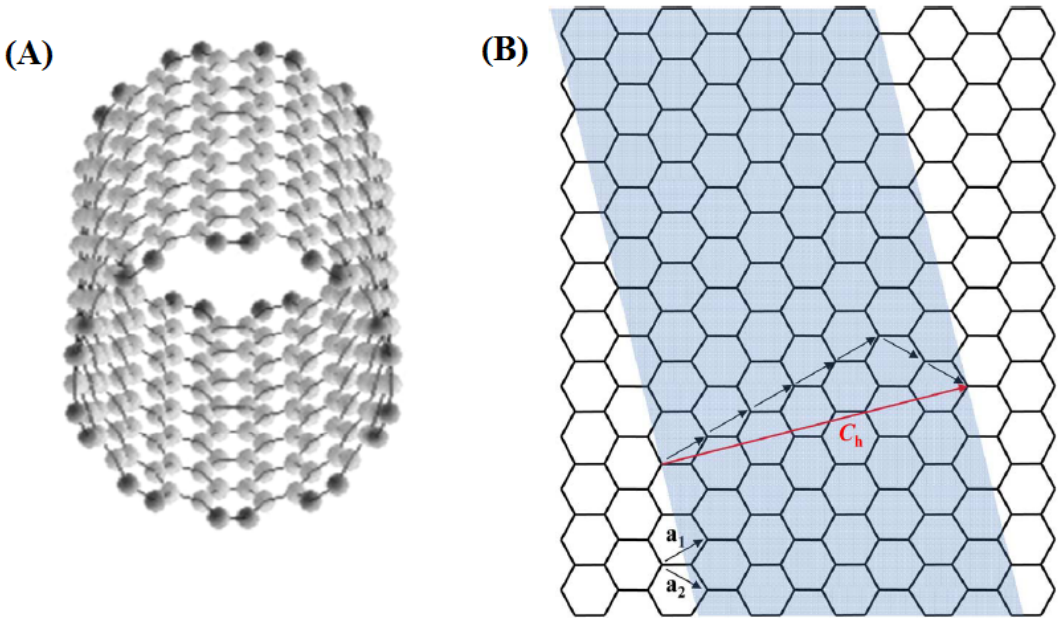

Figure 6.1: (A)Single-wall carbon nanotube, (B)The forming of SWCNT by folding a graphene sheet, and the chirality vector C_h is (5, 2) [3].

6.1 PRINCIPAL OF MODE-LOCKING BY SWCNTs AND ITS APPLICATIONS IN FIBER LASERS

CNTs are usually divided into two classes, multi-wall and single-wall ones, depending on the number of graphene layers that the CNTs is formed by rolling. However, in most cases, only the SWCNTs are used for photonic and electric applications. An interesting and important electric property of SWCNTs has been revealed by research that is SWCNTs can be either metallic or a semiconductor, solely depending the direction or vector along which graphene is rolled up to form SWCNTs or so-called chirality vector $C_h(n, m)$ [104, 105, 106]. If $n - m = 3k$ (k is an integer), it is metallic CNT that is formed, and $n - m \neq 3k$ for semiconducting CNTs. Figure 6.1B demonstrates the forming of metallic SWCNT by folding a graphene sheet whose chirality vector $C_h(n, m)$ is (5, 2). Also the diameter of the formed CNTs is

expressed as:

$$d = \frac{a}{\pi}\sqrt{n^2 + nm + m^2} \quad \text{where}\, a = 0.246nm \tag{6.1}$$

For semiconducting CNTs, their bandgaps are dependent on the size of tube diameter [107]. The typical diameter of the formed semiconducting CNTs is 0.7-1.5nm and correspondingly the bandgap energy is 1.2-0.5eV or 1-2μm in wavelength, and this range happens to overlap with the emission from rare-earth doped fibers which makes them suitable for many fiber-based photonic applications. Also nowadays for most reported and commonly used CNTs fabrication methods, it is not possible to control SWCNTs' growth chirality vector, so the product always contains CNTs of different types and various sizes and hence extends the application optical bandwidth of these mixed CNTs of various sizes to several hundred nanometers wide. Moreover, aligned SWCNTs shows polarization dependence [108], however the SWCNTs that we used to fabricate SA are randomly oriented on the fiber endtip, so no polarization dependence has been considered and observed for our case. Like in Figure 6.2A, SWCNTs has optical absorption between two energy level in conduction and valence bands.

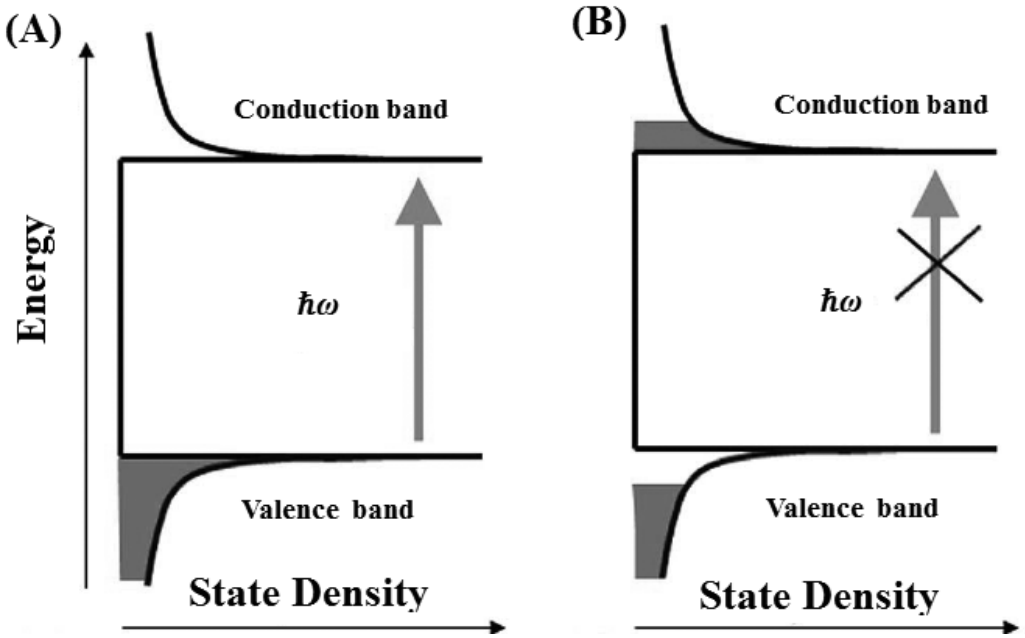

Figure 6.2: Optical absorption and saturable absorption in SWCNTs.

However, under intense excitation by light within band, the possible state at the conduction and valence bands are fully occupied, the absorption is thus saturated as seen in 6.2B. The recovery time of these transitions in SWCNTs are very fast, $\sim 1ps$ for E_{11} transition and $\sim 100fs$ for E_{22} transition as reported [109].

6.2 ALL-FIBER THULIUM-DOPED FIBER RING LASER WITH DISSIPATIVE SOLITON AND NOISE-LIKE OUTPUT IN NORMAL DISPERSION BY SWCNTs

As discussed so far, early mode-locked TDF fiber lasers were operated in soliton regime [24, 56, 57, 58]. The pulse energy of mode-locked fiber lasers were limited by the nonlinearity of construction fibers. More recently, by implementing normal-dispersion fiber cavity, fiber lasers operated in dissipative soliton regimes have also been demonstrated. In contrast to conservative solitons, dissipative solitons produced from normal-dispersion fiber lasers have demonstrated much higher pulse energy by allowing strongly chirped pulses to circulate in the oscillator, which suppresses the side effects from the intra-cavity nonlinearity that tends to destabilize and break down pulses [17]. For mode-locked TDF fiber laser with high pulse energy dissipative pulse output around $2\mu m$ wavelength, Gumenyuk reported the first mode-locked TDF laser with net normal dispersion in the cavity [110]. This was achieved by introducing a highly chirped fiber Bragg grating(FBG) at 2-μm into the fiber cavity. The mode-locked operation was realized using a wavelength-specific SESAM. Haxsen and *et al.* also reported a hybrid mode-locked fiber configuration by a combination of SESAM and NPE mechanisms for which normal dispersion fiber was used to create net normal intra-cavity dispersion [111].

In this part, we demonstrate a 1.9-μm passively mode-locked TDF ring oscillator with large net normal dispersion to produce both dissipative soliton and noise-like outputs. The mode-locked operation was enabled by using optically deposited SWCNTs on the fiber end tip as the saturable absorber. Dissipative soliton produced by the fiber laser oscillator was centered at $1947nm$ with 4.1-nm FWHM bandwidth. To our best knowledge, this is first all-

fiber dispersion-managed mode-locked TDF ring oscillator enabled by SWCNTs in normal dispersion.

Since most of silica fibers take anomalous dispersion around 1.9-2.0μm, carefully selected segments of dispersion engineered UHNA fiber with normal dispersion were added to the cavity to over compensate the anomalous dispersion from other fibers and create large net normal dispersion in the cavity at 1.9μm. As discussed in Chapter 2, the dispersion of single-mode fiber can be considered as the sum of material's dispersion and waveguide's dispersion, for which the waveguide's dispersion is determined by the fiber's geometry and refractive index profile. By reducing the core diameter and increasing NA, the zero dispersion wavelength of the fiber can be pushed towards the longer wavelength [30]. The core diameter of normal dispersion fiber (NDF) we used is 2.2μm and the NA is 0.35(Nufern UHNA4). A white-light interferometry technique [65] was employed to measure the fiber's dispersion like shown in Figure 2.9, for which Tm-doped fiber spontaneous emission is used as the light source. Figure 2.10 shows the measured interference pattern and the fitting results. The dispersion of the normal-dispersion fiber is measured to be $93ps^2/km$ at 1.9μm. Using the same method, the anomalous dispersion of the SMF-28e fiber at 1.9μm was measured to be $-67ps^2/km$ like in Figure 2.11. The dispersion of the Tm-doped active fiber used in the experiment was estimated to be $-12ps^2/km$.

The method used to fabricate our SWCNTs SAs is described as follows. $0.2mg/ml$ SWCNTs (Sigma-Aldrich) solution was developed by dispersing into N-dimethylformaminde solvent and ultrasonically bathed for 2 hours at room temperature. The dispersed SWCNTs were then optically deposited onto the end tip of angle-cut single mode fiber by an optical trapping method described in Ref. [96]. In this approach, a 100-mW 1550-nm EDFA spontaneous light source was used to optically trap SWCNTs onto the fiber tip in a similar set-up as depicted in Figure 5.5 . An enhanced back-reflection can be registered by an optical spectrum analyzer when the SWCNTs were successfully deposited. The SWCNTs end-coated fiber was then connected with a fiber patch cord using a bare fiber connector and a mating sleeve and thus completed the SWCNTs SA fabrication.

The fabricated SWCNTs SA is inserted into an all-fiber ring cavity as illustrated in Figure 6.3. The active fiber is 100-cm long single mode TDF with 5-μm core diameter and

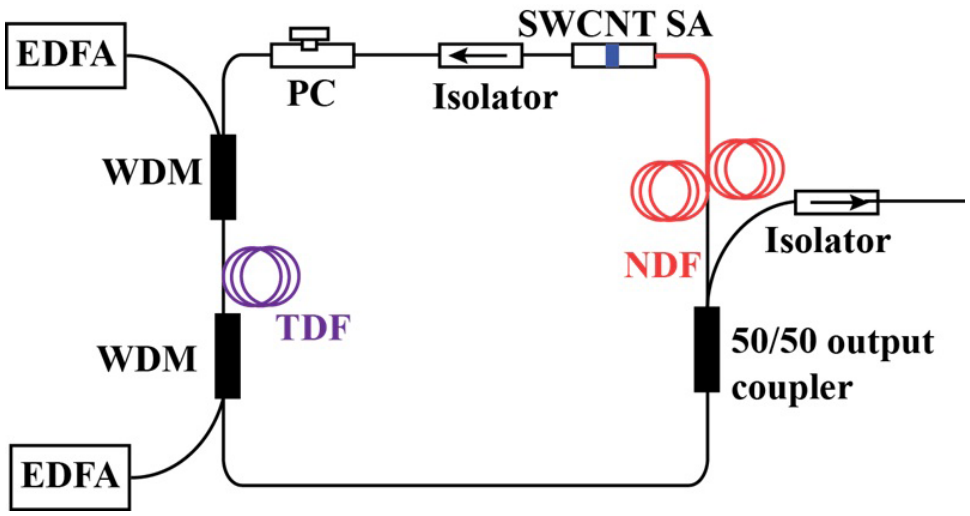

Figure 6.3: Scheme of the TDF ring cavity, based on fabricated SWCNTs SA [4].

0.23 NA. Two 1550-nm/1900-nm WDM couplers are used to couple pump light into the cavity. The amplified spontaneous emission from an erbium-doped fiber amplifiers fusion spliced to WDM provides forward and backward pumping simultaneously. A polarization insensitive isolator with 10% insertion loss and over 35-dB isolation at 2-μm wavelength is fusion spliced into the cavity and thus enforces a counterclockwise unidirectional ring. Part of the intra-cavity energy is coupled out through a 3-dB output coupler. 1% of the output is picked by a fast detector (EOTECH ET-5010F) for oscilloscope and RF analysis. Another isolator for 2-μm wavelength is also fusion spliced to output port to suppress back reflection into the cavity. An in-line polarization controller (PC) is included to finely tune the intra-cavity polarization state as for the consideration to balance the intrinsic weak birefringence of the included single mode fibers. No extra optical filter is added into the ring cavity. The Tm-doped fiber itself provides the spectral filtering and keeps the pulses self-consistent while circulating the cavity. In total there is about $6m$ of SMF-28e pigtail fiber in the laser cavity. The length of the NDF included in the cavity is $22m$. The net dispersion in the cavity is calculated as $1.63ps^2$. The small amount of dispersion due to the optical isolator can be neglected.

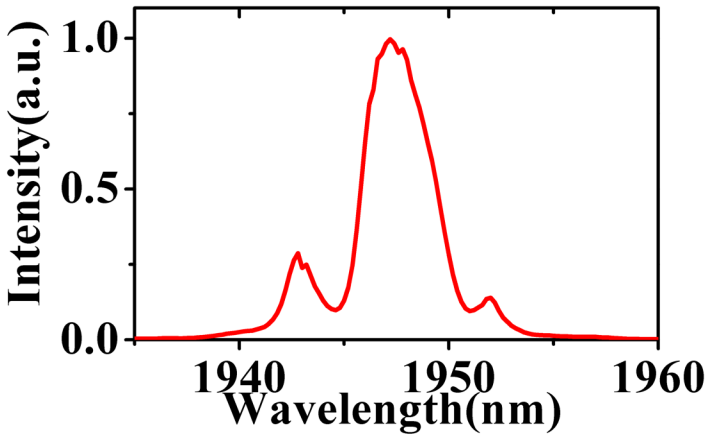

Figure 6.4: Typical spectrum of fiber laser under noise-like operation [4].

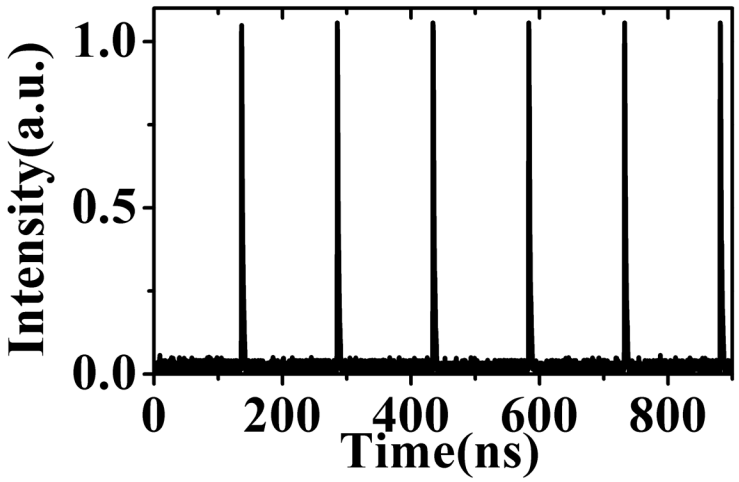

Figure 6.5: Pulse train on oscilloscope for fiber laser under noise-like operation [4].

Mode-locked operation is self-started as the pump ramps up to $650mW$. An output spectrum shown in Figure 6.4 reveals a FWHM bandwidth of $5.1nm$ laser pulse output. Figure 6.5 shows pulse trains produced by the fiber oscillator measured by an oscilloscope. The pulse width determined by a custom-built intensity autocorrelator shown in Figure 6.6.

Up conversion signal from a long scanning range of over 500-*ps* reveals a coherence spike on the zero time-delay over a wide pedestal. This indicates that the laser operates under the NL regime [112, 68]. Results shown in Figure 6.6 suggest a bunch of ultra-short pulses

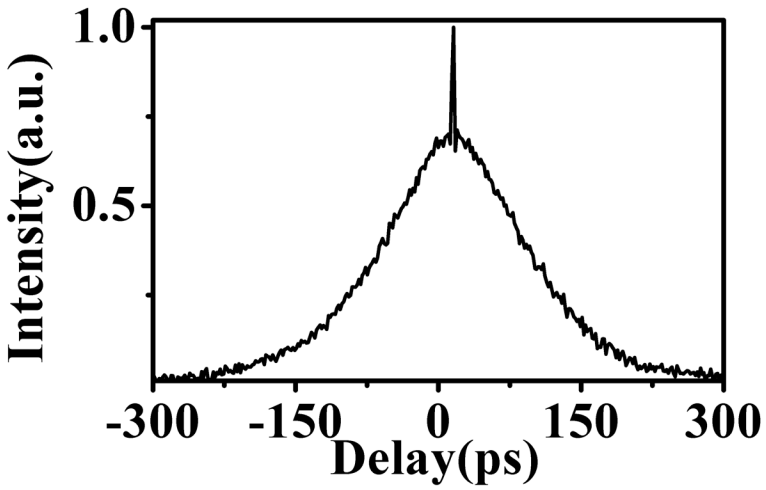

Figure 6.6: Intensity autocorrelation for fiber laser under noise-like operation [4].

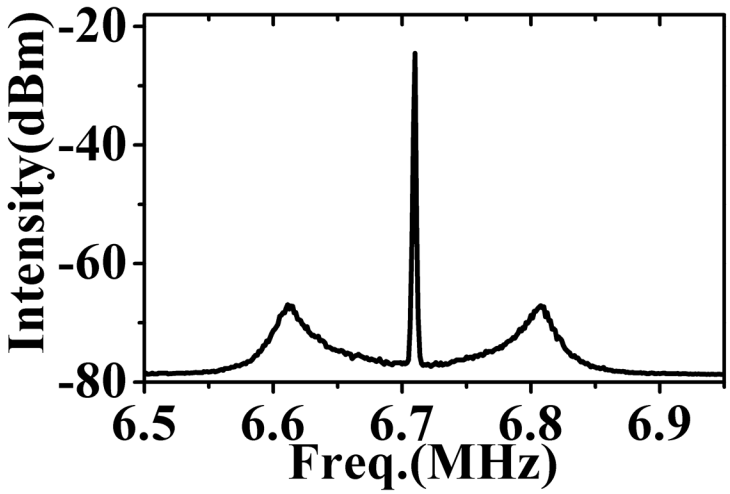

Figure 6.7: RF spectrum at fundamental repetition rate for fiber laser under noise-like operation [4].

with randomly varying pulse width and peak power are generated within an envelope of over 300 picoseconds. Figure 6.7 is the RF spectrum (measured by Agilent E4411B) of the NL pulses at the fundamental repetition rate; two wide side lobes and low SNR are indicative of the inherent jittering of NL operation. The output power was measured as 8.5mW which corresponds to 1.27-nJ per noise like pulse bundle. It is also confirmed the NL pulses produced by the laser cavity cannot be significantly compressed by propagating through negative dispersion compensating media.

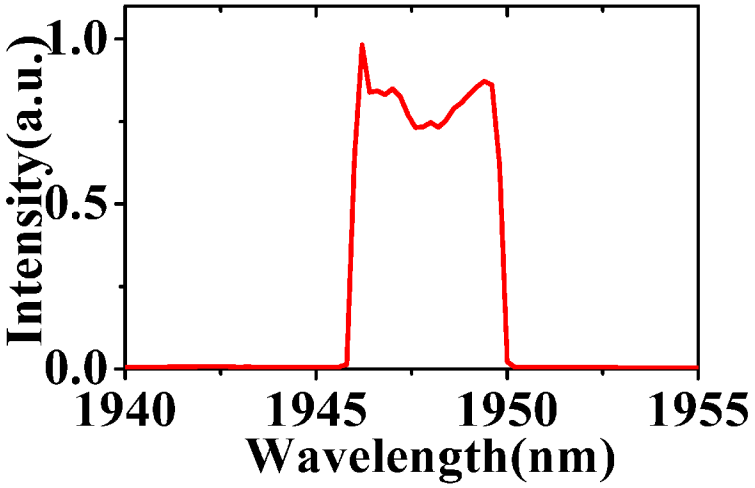

Figure 6.8: Typical spectrum of fiber laser under dissipative soliton operation [4].

By reducing the pump power down to 605mW, stable CW mode-locked pulses with significantly different characteristics were also observed. Figure 6.8 shows a typical optical spectrum of the stable mode-locked output with a resolution of 0.1nm on a linear scale. "Cat-ear" like spectrum with steep rising and falling edges are observed, which is indicative of the dissipative soliton operation in normal dispersion of the laser [17]. The central wavelength locates at 1947nm and the 3-dB spectral width is about 4.6nm. Figure 6.9 is the RF spectrum of the dissipative soliton output at the fundamental repetition rate. The SNR is as high as 46dB, this is comparable to Er-doped mode-lock fiber laser enabled by SWCNT [96]. It is indicative of stable operation and low jittering of the pulse trains. Figure 6.10 shows the autocorrelation trace of the produced pulses directly from the cavity. Assuming a Gaussian profile, it yields a pulse duration of ~47ps. Combined with the 4.1-nm bandwidth, the TBP

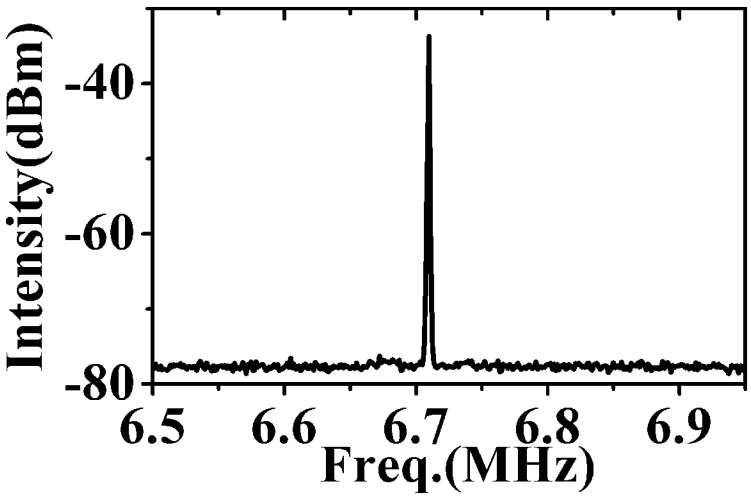

Figure 6.9: RF spectrum at fundamental repetition rate for fiber laser under dissipative soliton operation [4].

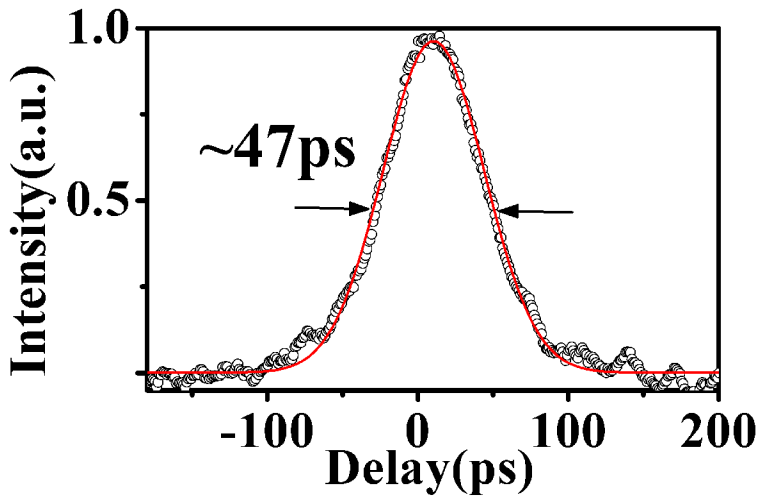

Figure 6.10: Intensity autocorrelation for fiber laser under dissipative soliton operation [4].

is calculated as ∼15.21. This is over 30 times of the transform limit 0.44, which suggests that the pulse is strongly chirped. The RF spectrum shown in Figure 6.9 also confirms only one pulse is generated per round trip. Figure 6.11 shows the pulses compression after propagating

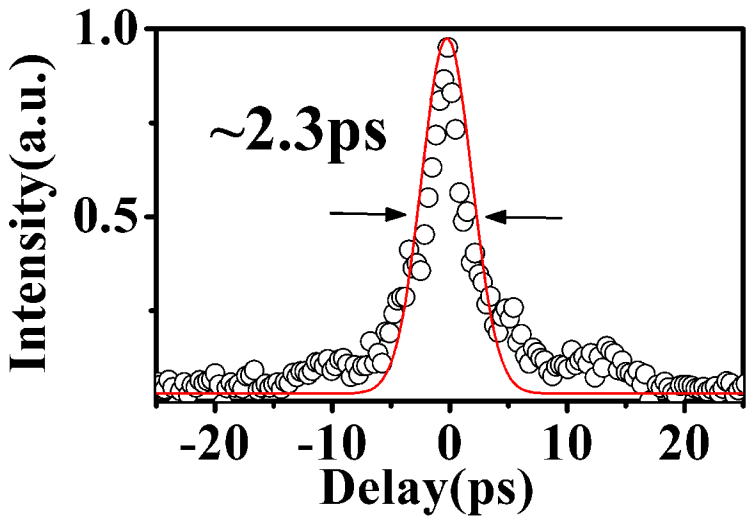

Figure 6.11: Autocorrelation of the compressed pulse after 180-m SMF-28e and Gaussian fitting for dissipative soliton output [4].

180-m SMF-28e fiber outside the cavity. The chirped pulses are compressed to $\sim$2.3ps. The average output power from the 50% output port is measured as 3mW under 605-mW pump. Given 6.71-MHz repetition rate, the per-pulse energy is about 0.45-nJ for the dissipative soliton pulses in normal dispersion. This value is about 4 times greater than that of the soliton pulse enabled by SWCNTs SA [57]. The stability of the fiber laser was also tested. The fiber laser is capable of several hours' continuous operation under both mode-locked regimes. We intermittently tested the laser over a period of 2 months, consistent operational performance has also been confirmed.

6.3 NUMERICAL SIMULATION OF MODE-LOCKED FIBERS BY SWCNTs

Again we use GLE equation 3.56 to simulate our SWCNTs SA assisted mode-locked fiber laser's behaviors. The two differences here from the simulation we did in Section 5.4 are: the inclusion of extra NDF in fiber cavity and the nonlinear transmittance curve for the lab-

fabricated SWCNT SA at 1.9μm, for which the first can be simply realized by additionally including a certain length of NDF fiber of specific normal GVD β_2 and the saturation properties of the fabricated SWCNTs SA need to be addressed. It was reported that SWCNTs SA has similar nonlinear saturation properties to the SESAMs. For example, the saturation curve at 1550nm for ~1-μm thick purified SWCNTs sandwiched by two quartz plates has been characterized by using a mode-locked erbium fiber laser as the excitation source [113]. The saturation intensity for their fabricated SWCNTs SA was estimated as I_s≈12.5MW/cm^2 and this value is very comparable to that of commonly used SESAMs [73]. The recovery lifetime of SWCNTs has also been measured by using a pump-probe setup and the measured recovery lifetime was in the order of 500fs [114, 115]. The real saturation intensity of the fabricated SWCNTs SA also shows to depend on the CNT material's quality (chirality distribution and purity) and the method used for fabrication. But the fast recovery lifetime of SWCNTs does not seem to vary significantly for different SWCNTs SAs.

As discussed above, the SCWCNTs SA shows similar saturable absorbtion with semiconductor-based SA, and thus a simple two-level saturable absorber model developed and commonly employed to model SESAMs as shown in Equation 6.2 [116] is used to simulate the loss as a function of the light intensity for our lab-fabricated SWCNTs SA in my codes.

$$\alpha(I) = \alpha_{non} + \frac{\alpha_s}{1 + I/I_s} \tag{6.2}$$

The loss due the fabricated SWCNTs SA is considered as the sum of two parts α_{non} and α_s. α_{non} is the unsaturable loss of our fabricated SWCNTs SA in which the coupling loss is also included; α_s is saturable loss which varies over light powers. It can be seen that the total loss α saturates to α_{non} as the light intensity goes up to infinity. The value of α_s is set to be 1% to 2% and α_{non} is 33% according to our experimental observations. In our simulation, it is also found there is a relatively wide range of saturation intensity (10-1000MW/cm^2) that we can select and set the saturation intensity I_s of our fabricated SWCNTs SA at for the realization of stable dissipative soliton mode-locking at 1.9-μm wavelength. Figure 6.12 shows a typical simulated absorption curve as a function of light intensity for which $\alpha_s = 1\%$, $\alpha_{non} = 33\%$, $I_s = 100MW/cm^2$ and the fiber mode area is estimated as 100μm^2.

Besides SWCNTs SA, Table 6.1 lists the typical parameters of the fibers and optical components we used in our simulation. Some things need to specially point out about the

Table 6.1: Fibers' and optical components' parameters used in simulation

Parts	Length(m)	$\beta_2(ps^2/km)$	$\gamma(W^{-1}km^{-1})$	Loss(dB)
SMF-28e	6	-67	1	0.05
TDF	1	-12	2	-
NDF	22	93	3	0.4
WDM	-	-	-	0.46
Isolator	-	-	-	0.96
Output coupler	-	-	-	3
Parts	Gain width(nm)	$g_0(dB/m)$	$E_{SAT}(nJ)$	Loss(dB)
TDF	40	40	6	-

numbers listed in Table 6.1.One is the fiber loss of NDF. As the core is reduced to 2.2μm in diameter, the transmission loss as 1.9-μm light travels in NDF is a lot greater than that in standard single-mode fiber and this loss can not be neglected in simulation any more. The average loss of NDF is estimated as $0.4dB/m$ which also take the loss due to fusion splicing with other fiber of different core size into account. The nonlinearity γ of NDF is estimated as $3W^{-1}km^{-1}$ which is greater than that of SMF-28e as a result of the reduced core size. Even though gain bandwidth of silicate TDF is over $100nm$ wide, in simulation the FWHM gain bandwidth is limited to $40nm$ and this is because the designed working bandwidth for most the fiber couplers and the isolator is only tens of nanometers wide centered about $1950nm$.

Following the procedures and numerical methods mentioned in Chapter 2, the simulated results for dissipative pulse generation by fabricated SWCNTs SA at net normal cavity dispersion are demonstrated as follows. Figure 6.13 shows the simulated mode-locked dissipative pulse building up from noise over 200 round trips in time domain. The pulse quickly converges to a stable solution allowed by the designated cavity after about 100 rounds, however for which this number also depends inial noise pulse shape we inject into cavity. Correspondingly, Figure 6.14 shows the spectral evolution as the dissipative pulses are build-

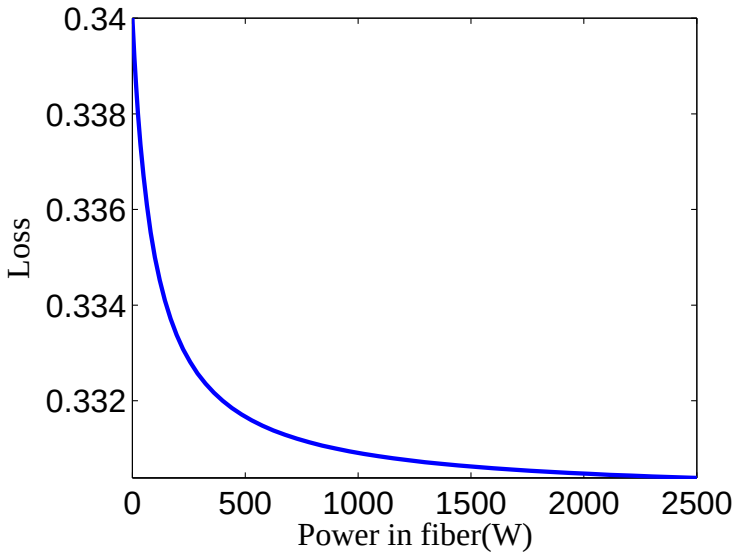

Figure 6.12: A typical simulated absorption curve as a function of light intensity for which $\alpha_s = 1\%$, $\alpha_{non} = 33\%$, $I_s = 100MW/cm^2$ and the fiber mode area is estimated as $100\mu m^2$.

ing up. Normalized temporal, spectral and chirping profiles for the inial Gaussian shaped pulse(blue) and the finalized converged dissipative pulse(red) are simultaneously depicted in Figure 6.15 for a clear comparison. Temporally, the finalized stable solution exhibits Gaussian-like pulse shape and FWHM width $\sim 50ps$ is very comparable to our experimental obtained value $47ps$. Spectrally, the finalized pulse with "car-ear" spectrum also agrees with our experimental observation. Within the pulse envelope, the pulse is of normal chirping, which indicates it can be further compressed close to its transform limit by propagating through optical medium of anomalous dispersion. The obtained pulse energy from the simulation is $0.71nJ$ which also at the same order of experimental value $0.45nJ$.

6.4 SUMMARY, DISCUSSION AND PROPOSED WORKS

To summarize, in this chapter an all-fiber SWCNTs SA mode-locked TDF laser ring oscillator in normal dispersion is demonstrated, for which the SWCNTs SA is fabricated by an efficient

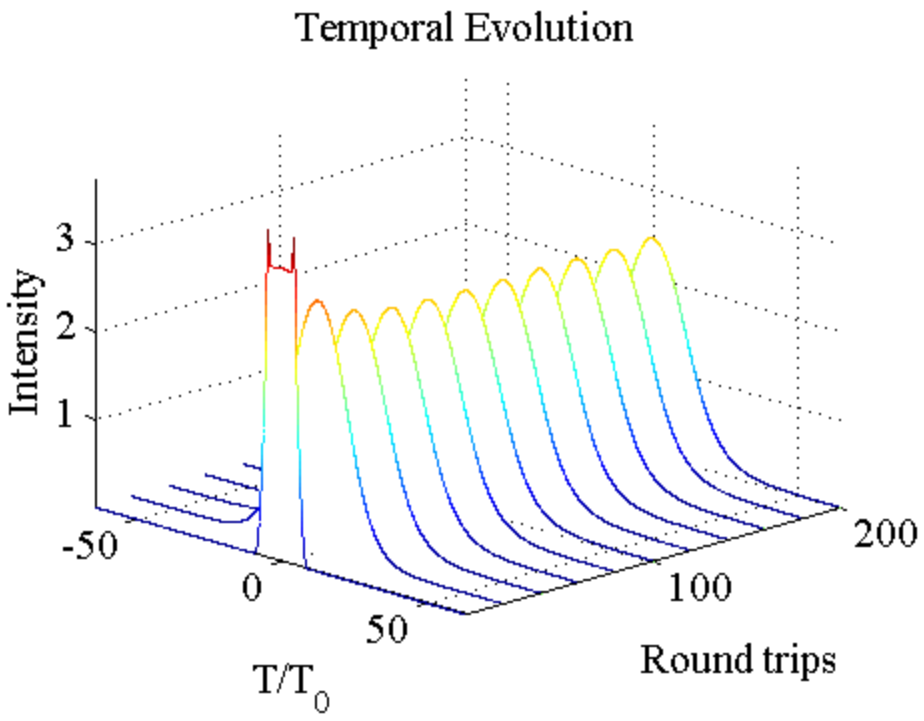

Figure 6.13: Simulated mode-locked dissipative pulse building up from noise over 200 round trips inside a designated fiber ring cavity in time domain.

optical deposition method and UHNA NDF fiber is introduced to create the net normal dispersion in fiber cavity. The pulse energy is boosted by 4 times in comparison to that for the soliton pulse. Numerical model for the designated fiber laser has also been established and successfully resembled mode-locking behaviors in both time and spectral domains.

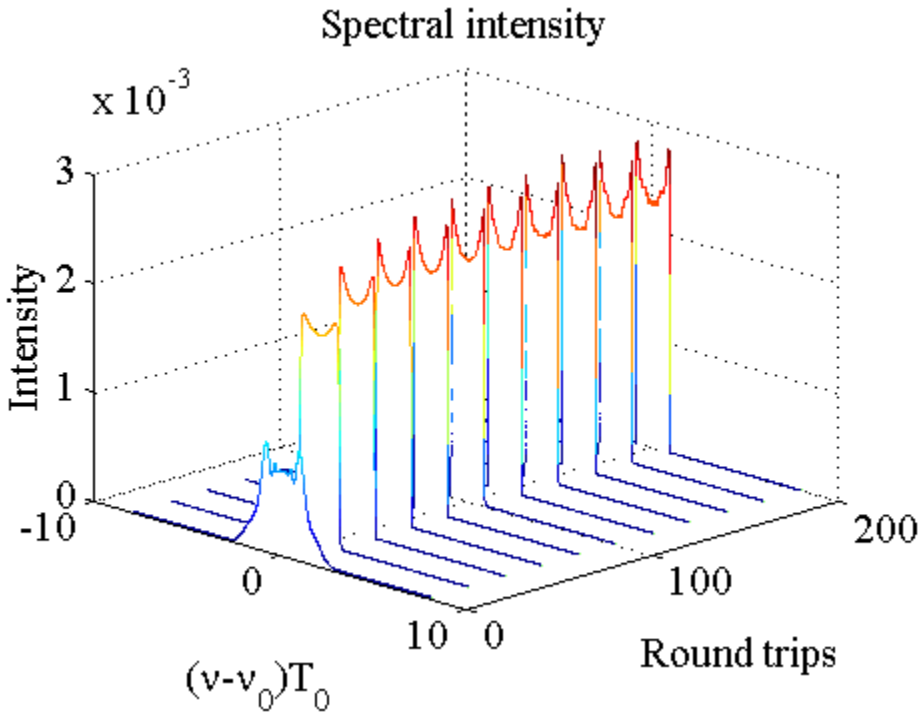

Figure 6.14: Simulated spectral evolution for mode-locked dissipative pulse building up from noise over 200 round trips inside a designated fiber ring cavity.

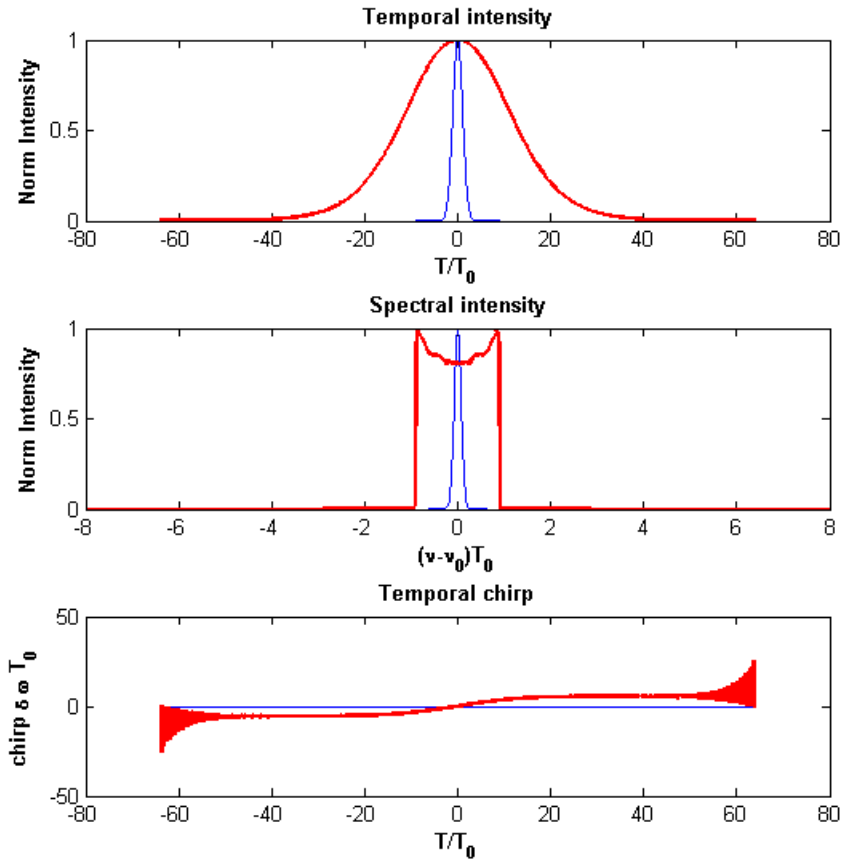

Figure 6.15: Normalized temporal, spectral and chirping profiles for the inial Gaussian shaped pulse(blue) and the finalized converged dissipative pulse(red). $\tau_0 = 2ps, \lambda_0 = 1950nm$

7.0 CONCLUSIONS AND PROPOSED FUTURE WORKS

7.1 SUMMARY AND CONCLUSIONS

In previous chapters, we have demonstrated the realization of all-fiber mode-locked TDF laser at $2\mu m$ by three different configurations, for which different mode-locking mechanisms or materials including NPE, GSAs and SWCNTs SAs are used to passively initialize the mode-locking and produce mode-locked short pulses. Each of them is studied and optimized; numerical simulation codes are also built to resemble our experimental observations.

However, this research field of mode-locked TDF fiber laser at $2\mu m$ still holds many aspects that demands further research efforts, nevertheless the challenges. Based on our preliminary successful work to date, there are several key technical challenges that remain to be solved. The first in we figure out the pulse energy we have achieve is still low. Focusing on the mode-locked oscillators we demonstrated, the highest non-breaking per-pulse energy is $0.45nJ$ which is produced from the dissipative soliton output by SWCNTs. Experiments and inoculations reveal that this limitation is mainly due to the unwanted anomalous GVD of the TDF and the excessive loss and nonlinearity from the UHNA NDF we introduced to control the total dispersion in fiber ring cavity. To solve these issues, it requires fiber manufacturers to redesign the TDF and optimize fiber manufacturing processes in order to control fiber's dispersion and reduce the transmittance loss at $2\mu m$. For example, spirally coupled core fibers with larger core area and weaker nonlinearity have been seen and applied for high energy mode-lock fiber lasers at other wavelengths [117, 118, 119]. Regarding future applications of mode-locked $2\mu m$ TDF lasers, if we get sufficient per-pulse energy out of these fiber lasers after amplification e.g. $> 5nJ$ based on simulation results, they can be used for many applications such as mid-IR supercontinuum generation via nonlinear conversion

processes by utilizing specialty glass or glass fiber e.g. chalcogenide and telluride and these fiber lasers will also be useful for high resolution chemical sensing, laser ablations and many more.

APPENDIX A

LIST OF ACRONYMS

ASE	Amplified Spontaneous Emission
CARS	Coherent anti-Stokes Raman spectroscopy
CGLE	Coupled Ginzburg-Landau Equation
CNLSE	Coupled Nonlinear Schrődinger Equation
CNT	Carbon Nano Tubes
CW	Continuous Wave
dB	Decibel
DMF	N-dimethylformaminde
EDFA	Erbium Doped Fiber Amplifier
FBG	Fiber Bragg Grating
FFT	Fast Fourier Transformation
FUT	Fiber Under Test
FWHM	Full Width at Half Maximum
FWM	Four-Wave Mixing
GLE	Ginzburg-Landau Equation
GSA	Graphene-based Saturable Asbsorber
GVD	Group Velocity Dispersion
HMIF	1-hexyl-3-methyl-imidazolium hexafluorophosphate
IR	Infrared

KLM	Kerr Lens Mode-locking
LIDAR	Light Detection and Ranging
LMA	Large Mode Area
NA	Numerical Aperture
NDF	Normal Dispersion Fiber
NL	Noise Like
NLSE	Nonlinear Schrődinger Equation
NPE	Nonlinear Polarization Evolution
OSA	Optical Spectrum Analyzer
PC	Polarization Controler
RF	Radio Frequency
RK4	Runge-Kutta 4th Order
SA	Saturable Absorber
SESAM	Semiconductor Saturable Absorber Mirror
SMF	Single Mode Fiber
SNR	Signal to Noise Ratio
SWCNT	Single-wall Carbon Nanotube
TBP	Time Bandwidth Product
TOD	Third Order Dispersion
UHNA	Ultra High Numerical Aperture
WDM	Wavelength Division Multiplexing
XPM	Cross Phase Modulation

APPENDIX B

DERIVATION OF NONLINEAR SCHRÖDINGER EQUATION

In general, analytical solutions to the wave propagation equation 3.16 do not exist and it is even extremely difficult or impossible to directly solve 3.16 by any numerical method due to the dimensionality of the problem. To solve that, some assumptions and approximations must be made and in this way an approximate scalar form of 3.16 *i.e.* Nonlinear Schrödinger Equation can be derived and used. These assumptions and approximations include: nonlinear effects are really weak and $\mathbf{P}_{NL}$ is treated as a small perturbation term compared to $\mathbf{P}_{LN}$; the optical field is quasi-monochromatic that is the pulse spectral width $\Delta\omega$ is much much smaller than the center frequency ω_0 ($\Delta\omega \ll \omega_0$) and the light polarization does not alter over a length of fiber in order to apply a scalar approach. The last assumption is actually relaxed in our simulation to model mode-locking fiber laser via NPE by solving CNLSEs.

Adopting a slowly varying envelope approximation, we can separate the rapidly varying part of the electric field by writing it in the form of

$$\mathbf{E}(\mathbf{r},t) = \frac{1}{2}\hat{x}\left[E(\mathbf{r},t)\exp(-\mathrm{i}\omega_0 t) + E^*(\mathbf{r},t)\exp(\mathrm{i}\omega_0 t)\right] \tag{B.1}$$

where $textbf{E}(\mathbf{r},t)$ is the slowly varying pulse envelope.

Linear and nonlinear polarization responses $\mathbf{P}_{LN}$ and $\mathbf{P}_{NL}$ can also be written in a similar form as follows

$$\mathbf{P}_{LN}(\mathbf{r},t) = \frac{1}{2}\hat{x}\left[P_{LN}(\mathbf{r},t)\exp(-\mathrm{i}\omega_0 t) + {P_{LN}}^*(\mathbf{r},t)\exp(\mathrm{i}\omega_0 t)\right] \tag{B.2}$$

$$\mathbf{P}_{NL}(\mathbf{r},t) = \frac{1}{2}\hat{x}\left[P_{NL}(\mathbf{r},t)\exp(-\mathrm{i}\omega_0 t) + {P_{NL}}^*(\mathbf{r},t)\exp(\mathrm{i}\omega_0 t)\right] \tag{B.3}$$

Substituting B.1, B.2 and B.3 into 3.16 and applying Fourier transformation onto its two sides where P_{LN} and P_{NL} are expressed with their relation to E, the aftermath obtained equation will be of a Helmholtz form

$$\nabla^2\tilde{E} + \varepsilon(\omega)k_0^2\tilde{E} = 0 \tag{B.4}$$

where $\tilde{E}$ is the Fourier transform of $E(\mathbf{r},t)$, defined as

$$\tilde{E}(\mathbf{r},\omega-\omega_0) = \int_{-\infty}^{\infty} E(\mathbf{r},t)\exp[\mathrm{i}(\omega-\omega_0)t]dt \tag{B.5}$$

and

$$\varepsilon(\omega) = 1 + \tilde{\chi}_{xx}^{(1)}(\omega) + \varepsilon_{\mathrm{NL}} \tag{B.6}$$

where $\varepsilon_{\mathrm{NL}}$ is treated as a constant under the slowly varying envelope approximation and $\varepsilon_{\mathrm{NL}} = \frac{3}{4}\chi_{xxxx}^{(3)}|E(\mathbf{r},t)|^2$.

Helmholtz equation B.4 can be solved by using variable separation method

$$\tilde{E}(\mathbf{r},\omega-\omega_0) = F(x,y)\tilde{A}(z,\omega-\omega_0)\exp(\mathrm{i}\beta_0 z) \tag{B.7}$$

where $\tilde{A}(z,\omega-\omega_0)$ is a slowly varying function of z and we get two equations

$$\frac{\partial^2 F}{\partial x^2} + \frac{\partial^2 F}{\partial y^2} + [\varepsilon(\omega)k_0^2 - \tilde{\beta}^2]F = 0 \tag{B.8}$$

$$2\mathrm{i}\beta_0\frac{\partial\tilde{A}}{\partial z} + (\tilde{\beta}^2 - \beta_0^2)\tilde{A} = 0 \tag{B.9}$$

and β_0 is the wave number to be determined.

Equation B.8 can be solved by first-order perturbation theory and the eigenvalue $\tilde{\beta}_0$ is found as

$$\tilde{\beta}(\omega) = \beta(\omega) + \Delta\beta(\omega), \tag{B.10}$$

where

$$\Delta\beta(\omega) = \frac{\omega^2 n(\omega)}{c^2\beta(\omega)}\frac{\iint \Delta n(\omega)|F(x,y)|^2 dxdy}{\iint |F(x,y)|^2 dxdy} \tag{B.11}$$

and

$$\Delta n = n_2|E|^2 + \frac{\mathrm{i}\tilde{a}}{2k_0}. \tag{B.12}$$

As a result, Equation B.9 is written as

$$\frac{\partial \tilde{A}}{\partial z} = \mathrm{i}[\beta(\omega) + \Delta\beta(\omega) - \beta_0]\tilde{A} \tag{B.13}$$

where we have approximated $\tilde{\beta}^2 - \beta_0^2$ by $2\beta_0(\tilde{\beta} - \beta_0)$. Expanding $\beta(\omega)$ and $\Delta\beta(\omega)$ around carrier frequency ω_0 in Taylor series as

$$\beta(\omega) = \beta_0 + (\omega - \omega_0)\beta_1 + \frac{1}{2}(\omega - \omega_0)^2\beta_2 + \frac{1}{6}(\omega - \omega_0)^3\beta_3 + \cdots, \tag{B.14}$$

$$\Delta\beta(\omega) = \Delta\beta_0 + (\omega - \omega_0)\Delta\beta_1 + \frac{1}{2}(\omega - \omega_0)^2\Delta\beta_2 + \frac{1}{6}(\omega - \omega_0)^3\Delta\beta_3 + \cdots, \tag{B.15}$$

and omitting some high order terms, Equation B.13 comes to

$$\frac{\partial A}{\partial z} + \beta_1\frac{\partial A}{\partial t} + \frac{\mathrm{i}\beta_2}{2}\frac{\partial^2 A}{\partial t^2} - \frac{\beta_3}{6}\frac{\partial^3 A}{\partial t^3} = \mathrm{i}\Delta\beta_0 A \tag{B.16}$$

after converting back to time domain and

$$\Delta\beta_0 = \frac{\alpha}{2} + \mathrm{i}\gamma(\omega_0)|A|^2. \tag{B.17}$$

Now we derive NLSE of the form

$$\frac{\partial A}{\partial z} + \beta_1\frac{\partial A}{\partial t} + \frac{\mathrm{i}\beta_2}{2}\frac{\partial^2 A}{\partial t^2} - \frac{\beta_3}{6}\frac{\partial^3 A}{\partial t^3} + \frac{\alpha}{2}A = \mathrm{i}\gamma(\omega_0)|A|^2 \tag{B.18}$$

where fiber's nonlinear parameter γ is defined as

$$\gamma(\omega_0) = \frac{n_2(\omega_0)\omega_0}{cA_{\text{eff}}}. \tag{B.19}$$

A_{eff} is referred as the effective mode area and is defined as

$$A_{\text{eff}} = \frac{\left|\iint |F(x,y)|^2 dxdy\right|^2}{\iint |F(x,y)|^4 dxdy}. \tag{B.20}$$

APPENDIX C

MATLAB CODES FOR PULSE PROPAGATION IN SINGLE MODE FIBER BY SPLIT-STEP FOURIER METHOD

The following Matlab codes are written to simulate the pulse propagation in single mode fiber ring cavity by solving the NLS equation using split-step Fourier method. Components simulated to consist of the fiber ring cavity includes passive fiber, active gain fiber, output couplers and artificial saturable absorbers. However this simulation model we have developed here are also very expandable and capable to integrate with new fiber optical components like FBGs, spectral filters, frequency modulators and many more by applying and interacting with pulse signals in either time or frequency domain.

```
%Main loop to simulate pulse propagation inside fiber loop cavity, and codes
   for the GUI control callbacks are hidden.
function varargout = project_GUI_06_06(varargin)
%      PROJECT_GUI_06_06, by itself, creates a new PROJECT_GUI_06_06 or raises
    the existing
%      singleton*.
%
%      H = PROJECT_GUI_06_06 returns the handle to a new PROJECT_GUI_06_06 or
   the handle to
%      the existing singleton*.
%
%      PROJECT_GUI_06_06('CALLBACK',hObject,eventData,handles,...) calls the
   local
%      function named CALLBACK in PROJECT_GUI_06_06.M with the given input
   arguments.
%
%      PROJECT_GUI_06_06('Property','Value',...) creates a new
   PROJECT_GUI_06_06 or raises the
%      existing singleton*.  Starting from the left, property value pairs are
```

```
%      applied to the GUI before project_GUI_06_06_OpeningFcn gets called.  An
%      unrecognized property name or invalid value makes property application
%      stop.  All inputs are passed to project_GUI_06_06_OpeningFcn via
   varargin.
%
%      *See GUI Options on GUIDE's Tools menu.  Choose "GUI allows only one
%      instance to run (singleton)".
%
% See also: GUIDE, GUIDATA, GUIHANDLES
function pushbutton2_Callback(hObject, eventdata, handles)
% hObject    handle to pushbutton2 (see GCBO)
% eventdata  reserved - to be defined in a future version of MATLAB
% handles    structure with handles and user data (see GUIDATA)
fs=str2num(get(handles.fs,'string'));%sampling rate within time scale of T0
windowsize=str2num(get(handles.windowsize,'string'));%window size in term of
   time scale T0
N=fs*windowsize;%number of points
lamda0=str2double(get(handles.lamda0,'string'));%center wavelength in nm
fiberlength=str2double(get(handles.fiberlength,'string'));% fiber length in
   meter
fiberloss=str2double(get(handles.fiberloss,'string'));%fiber loss in dB/m
beta2=str2double(get(handles.beta2,'string'));%fiber second order dispersion
   in picosecond^2/kilometer
beta3=str2double(get(handles.beta3,'string'));%TOD in picosecond^3/kilometer
gamma=str2double(get(handles.gamma,'string'));%nonlinearity in /(W-km)
gfiberlength=str2double(get(handles.gfiberlength,'string'));% fiber length in
   meter
gfiberloss=str2double(get(handles.gfiberloss,'string'));%fiber loss in dB/m
gbeta2=str2double(get(handles.gbeta2,'string'));%fiber second order dispersion
    in picosecond^2/kilometer
gbeta3=str2double(get(handles.gbeta3,'string'));%TOD in picosecond^3/kilometer
ggamma=str2double(get(handles.ggamma,'string'));%nonlinearity in /(W-km)
gainstrength=str2double(get(handles.gainstrength,'string')); %amplification
   gain in dB/m
gainbandwidth=str2double(get(handles.gainbandwidth,'string'));%gainband FWHM
energysat=str2double(get(handles.energysat,'string'));%gain saturated pulse
   energy in nJ
Isa=str2double(get(handles.Isa,'string'));%W
energy_tempstring=num2str(0);
set(handles.energy_temp,'string',energy_tempstring);
tau=(0:1/fs:windowsize-1/fs)-(windowsize)/2;
omega=2*pi*fftshift(([1:N]-1-N/2)*fs/N);
if m~=0
u=1*exp(-0.5*(1+1i*C)*tau.^(2*m));%incidient pulse
else
    u=n*sech(tau).*exp(-.5*1i*C*tau.^2);
end
roundtrips=str2num(get(handles.roundtrips,'string'));
envelope=zeros(roundtrips+1,N);
envelope(1,:)=u;
for jj=1:roundtrips
    u=GAINFIBER(u, gfiberlength, gfiberloss, gbeta2, gbeta3, ggamma, lamda0,
       gainstrength, gainbandwidth, energysat, fs, windowsize);
```

```
    u=PASSIVEFIBER(u, fiberlength/2, fiberloss, beta2, beta3, gamma, lamda0,
        fs, windowsize);
    envelope(jj+1,:)=u;
    u=0.7*SA2(u,Isa);
    u=PASSIVEFIBER(u, fiberlength/2, fiberloss, beta2, beta3, gamma, lamda0,
        fs, windowsize);
    jjstring=num2str(jj);
    set(handles.jj,'string',jjstring);
    pause(0.001);
end



%Passive fiber with loss, GVD, TOD, SPM and Raman response(simplified model).
function envelope=PASSIVEFIBER(u, fiberlength, fiberloss, beta2, beta3, gamma,
    lamda0, fs, windowsize)
% fiberlength in meter fiber loss in dB/m, beta2 fiber second order dispersion
    in picosecond^2/kilometer,  beta3 TOD in picosecond^3/kilometer, gamma
   nonlinearity in /(W-km), lamda0 wavelength in nm.
Ld=T0^2/abs(beta2);%dispersion length in meter
fiberloss=fiberloss*Ld; %fiber loss in /Ld
fiberlength=fiberlength/Ld;%fiber length in dispersion length
signofbeta2=sign(beta2);
Ln=1000/gamma/p0;%nonliear length in meters
NN=Ld/Ln;
step_num=ceil(100*fiberlength*Ld)*ceil(NN+0.001);% step numbers in spacial
   domain, 100*NN steps per meter
ddz=fiberlength/step_num;%step length in term of disperion length
spetra_temp=ifft(u);
energy_temp=spetra_temp*spetra_temp'*windowsize*T0*p0;%pulse energy
N=fs*windowsize;
omega=2*pi*fftshift(([1:N]-1-N/2)*fs/N); %angular frequency
dispersion=exp(1i*0.5*signofbeta2*omega.^2*ddz+1i*beta3/beta2/T0/6*omega.^3*
   ddz);% second order dispersion &third order dispersion induced phase
   change in frequency domain
hhz=1i*NN*ddz;
u=u.*exp(abs(u).^2.*hhz/2);
indexingtriger=0.000;
mark=0.1*fiberlength;%save file for every mark length in Ld
envelope=[];
spectra=[];
energy=[];
dz=ddz;
for flag  = 1:step_num
   dispersion=exp(1i*0.5*signofbeta2*omega.^2*dz+1i*beta3/beta2/T0/6*omega.^3*
      dz);
   lossgain=exp((-fiberloss)/2.*dz);
   spetra_temp=ifft(u).*dispersion.*lossgain;%add dispersion and amplification
       onto frequency domain
   u=fft(spetra_temp);%back to time domain
   hhz=1i*NN*dz;
   k1=hhz*(abs(u).^2);%.*(exp(-1*fiberloss*flag));
   k2=hhz*(abs(u).^2).*(abs(exp(k1./2)).^2);%*exp(-1*fiberloss*(flag+0.5*dz));
```

```
    k3=hhz*(abs(u).^2).*(abs(exp(k2./2)).^2);%*exp(-1*fiberloss*(flag+0.5*dz));
    k4=hhz*(abs(u).^2).*(abs(exp(k3)).^2);%.*exp(-1*fiberloss*(flag+dz));
    u=u.*exp(k1/6+k2/3+k3/3+k4/6);%add nonlinear dispersion by RK4 method
    %energy_temp=spetra_temp*spetra_temp'*windowsize*T0*p0;%pulse energy
    %energy_temp=u*u'*T0/fs*p0;%pulse energy
    %u=u.*exp(abs(u).^2.*hhz);%non-RK
end
 u=u.*exp(-1*abs(u).^2.*hhz/2);
 envelope=[envelope;u];



% Pulse's energy calculation
function y=GETENERGY(u,fs,windowsize)
T0=2000;
p0=5;
y=p0*sum(u.*conj(u),2)*T0/fs/1000000;
end



%Intensity modulation from saturable absorber
function envelope=SA2(u, Isa)
p0=5;
e=0.01;
I=Isa/5;
envelope=u.*((e+(abs(u)).^2/I)./(1+(abs(u)).^2/I)).^0.5;% can be arbitrary
    functions
end
```

BIBLIOGRAPHY

[1] Q Wang, T Chen, B Zhang, AP Heberle, and KP Chen. All-fiber passively mode-locked thulium-doped fiber ring oscillator operated at solitary and noiselike modes. *Optics letters*, 36(19):3750–3752, 2011.

[2] QingQing Wang, Tong Chen, Botao Zhang, Mingshan Li, Yongfeng Lu, and Kevin P Chen. All-fiber passively mode-locked thulium-doped fiber ring laser using optically deposited graphene saturable absorbers. *Applied Physics Letters*, 102(13):131117–131117, 2013.

[3] S. Yamashita. A tutorial on nonlinear photonic applications of carbon nanotube and graphene. *Lightwave Technology, Journal of*, 30(4):427–447, 2012.

[4] QingQing Wang, Tong Chen, Mingshan Li, Botao Zhang, Yongfeng Lu, and Kevin P Chen. All-fiber ultrafast thulium-doped fiber ring laser with dissipative soliton and noise-like output in normal dispersion by single-wall carbon nanotubes. *Applied Physics Letters*, 103(1):011103–011103, 2013.

[5] U.S. Patent 3353115, 1967.

[6] Ahmed H. Zewail. Femtochemistry:recent progress in studies of dynamics and control of reactions and their transition states. *The Journal of Physical Chemistry*, 100(31):12701–12724, 1996.

[7] David J. Jones, Scott A. Diddams, Jinendra K. Ranka, Andrew Stentz, Robert S. Windeler, John L. Hall, and Steven T. Cundiff. Carrier-envelope phase control of femtosecond mode-locked lasers and direct optical frequency synthesis. *Science*, 288(5466):635–639, 2000.

[8] PT Mannion, J Magee, E Coyne, GM OConnor, and TJ Glynn. The effect of damage accumulation behaviour on ablation thresholds and damage morphology in ultrafast laser micro-machining of common metals in air. *Applied surface science*, 233(1):275–287, 2004.

[9] J Meijer, K Du, A Gillner, D Hoffmann, VS Kovalenko, T Masuzawa, A Ostendorf, R Poprawe, and W Schulz. Laser machining by short and ultrashort pulses, state of

the art and new opportunities in the age of the photons. *CIRP Annals-Manufacturing Technology*, 51(2):531–550, 2002.

[10] Christopher Smelser, Stephen Mihailov, and Dan Grobnic. Formation of type i-ir and type ii-ir gratings with an ultrafast ir laser and a phase mask. *Optics Express*, 13(14):5377–5386, 2005.

[11] Ji-Xin Cheng and X Sunney Xie. Coherent anti-stokes raman scattering microscopy: instrumentation, theory, and applications. *The Journal of Physical Chemistry B*, 108(3):827–840, 2004.

[12] DA Rusak, BC Castle, BW Smith, and JD Winefordner. Fundamentals and applications of laser-induced breakdown spectroscopy. *Critical Reviews in Analytical Chemistry*, 27(4):257–290, 1997.

[13] Holger Lubatschowski, Alexander Heisterkamp, Fabian Will, Ajoy I Singh, Jesper Serbin, Andreas Ostendorf, Omid Kermani, Ralf Heermann, Herbert Welling, and Wolfgang Ertmer. Medical applications for ultrafast laser pulses. *Riken Review*, pages 113–118, 2003.

[14] Tingye Li. *Optical Fiber Communications: Fiber Fabrication*. Academic Press, 1985.

[15] O. G. Okhotnikov, L. Gomes, N. Xiang, T. Jouhti, and A. B. Grudinin. Mode-locked ytterbium fiber laser tunable in the 980–1070-nm spectral range. *Opt. Lett.*, 28(17):1522–1524, Sep 2003.

[16] J. R. Buckley, F. W. Wise, F. Ö. Ilday, and T. Sosnowski. Femtosecond fiber lasers with pulse energies above 10 nj. *Opt. Lett.*, 30(14):1888–1890, Jul 2005.

[17] W. H. Renninger, A. Chong, and F. W. Wise. Dissipative solitons in normal-dispersion fiber lasers. *Phys. Rev. A*, 77:023814, Feb 2008.

[18] Kin Foong Chan, George J Vassar, T Joshua Pfefer, Joel MH Teichman, Randolph D Glickman, Susan T Weintraub, and Ashley J Welch. Holmium: Yag laser lithotripsy: a dominant photothermal ablative mechanism with chemical decomposition of urinary calculi. *Lasers in surgery and medicine*, 25(1):22–37, 1999.

[19] Nicholas J Scott, Christopher M Cilip, and Nathaniel M Fried. Thulium fiber laser ablation of urinary stones through small-core optical fibers. *Selected Topics in Quantum Electronics, IEEE Journal of*, 15(2):435–440, 2009.

[20] Kenneth L. Schepler, Brian D. Smith, Frank Heine, and Peter A. Budni. Mode-locking of diode-pumped tm,ho:ylf. In *Advanced Solid State Lasers*, page UP9. Optical Society of America, 1994.

[21] Helge Fonnum, Espen Lippert, and Magnus W. Haakestad. 550 mj q-switched cryogenic ho:ylf oscillator pumped with a 100 w tm:fiber laser. *Opt. Lett.*, 38(11):1884–1886, Jun 2013.

[22] Paul JM Suni and Sammy W Henderson. 1-mj/pulse tm: Yag laser pumped by a 3-w diode laser. *Optics letters*, 16(11):817–819, 1991.

[23] Joseph F Pinto, Leon Esterowitz, and Gregg H Rosenblatt. Continuous-wave mode-locked 2-μm tm: Yag laser. *Optics letters*, 17(10):731–732, 1992.

[24] L. E. Nelson, E. P. Ippen, and H. A. Haus. Broadly tunable sub-500 fs pulses from an additive-pulse mode-locked thulium-doped fiber ring laser. *Applied Physics Letters*, 67(1):19–21, 1995.

[25] KC Kao and George A Hockham. Dielectric-fibre surface waveguides for optical frequencies. *Electrical Engineers, Proceedings of the Institution of*, 113(7):1151–1158, 1966.

[26] Gordon A Thomas, Boris I Shraiman, Paul F Glodis, and Michael J Stephen. Towards the clarity limit in optical fibre. *Nature*, 404(6775):262–264, 2000.

[27] Amnon Yariv and Pochi Yeh. *Photonics: Optical Electronics in Modern Communications (The Oxford Series in Electrical and Computer Engineering)*. Oxford University Press, Inc., 2006.

[28] W. Sellmeier. *Ann. Phys. Chem.*, 143:271, 1871.

[29] Bahaa EA Saleh, Malvin Carl Teich, and Bahaa E Saleh. *Fundamentals of photonics*, volume 22. Wiley New York, 1991.

[30] B. Ainslie and C. Day. A review of single-mode fibers with modified dispersion characteristics. *Lightwave Technology, Journal of*, 4(8):967 – 979, aug 1986.

[31] L Cohen. Comparison of single-mode fiber dispersion measurement techniques. *Lightwave Technology, Journal of*, 3(5):958–966, 1985.

[32] S. C. Rashleigh. Measurement of fiber birefringence by wavelength scanning: effect of dispersion. *Opt. Lett.*, 8(6):336–338, Jun 1983.

[33] B Huttner, J Reecht, N Gisin, R Passy, and JP Von der Weid. Local birefringence measurements in single-mode fibers with coherent optical frequency-domain reflectometry. *Photonics Technology Letters, IEEE*, 10(10):1458–1460, 1998.

[34] Xiaojun Fang and Richard O Claus. Polarization-independent all-fiber wavelength-division multiplexer based on a sagnac interferometer. *Optics letters*, 20(20):2146–2148, 1995.

[35] Hyun-Min Kim, Tae-Hun Kim, Bongkyun Kim, and Youngjoo Chung. Enhanced transverse load sensitivity by using a highly birefringent photonic crystal fiber with larger air holes on one axis. *Applied optics*, 49(20):3841–3845, 2010.

[36] Rei Kitamura, Laurent Pilon, and Miroslaw Jonasz. Optical constants of silica glass from extreme ultraviolet to far infrared at near room temperature. *Applied optics*, 46(33):8118–8133, 2007.

[37] Philippe M Becker, Anders A Olsson, and Jay R Simpson. *Erbium-doped fiber amplifiers: fundamentals and technology*. Access Online via Elsevier, 1999.

[38] Wilfried Blanc, Pavel Peterka, Basile Faure, Bernard Dussardier, Gérard Monnom, Ivan Kašík, Jiří Kaňka, David Simpson, and Greg Baxter. Characterization of a thulium-doped silica-based optical fibre for s-band amplification. In *Photonics, Devices, and Systems III*, pages 61800V–61800V. International Society for Optics and Photonics, 2006.

[39] Peter F Moulton, Glen A Rines, Evgueni V Slobodtchikov, Kevin F Wall, Gavin Frith, Bryce Samson, and Adrian LG Carter. Tm-doped fiber lasers: fundamentals and power scaling. *Selected Topics in Quantum Electronics, IEEE Journal of*, 15(1):85–92, 2009.

[40] John David Jackson and Ronald F Fox. Classical electrodynamics. *American Journal of Physics*, 67:841, 1999.

[41] Andrew R Chraplyvy, Fabrizio Forghieri, Alan H Gnauck, and Robert W Tkach. Dispersion compensation in optical fiber communications, September 24 1996. US Patent 5,559,920.

[42] Finlay M Knox, Wladek Forysiak, and Nicholas J Doran. 10-gbt/s soliton communication systems over standard fiber at 1.55 μm and the use of dispersion compensation. *Lightwave Technology, Journal of*, 13(10):1955–1962, 1995.

[43] David Milam. Review and assessment of measured values of the nonlinear refractive-index coefficient of fused silica. *Applied optics*, 37(3):546–550, 1998.

[44] Govind P Agrawal. *Nonlinear fiber optics*. Springer, 2000.

[45] Roger H Stolen, James P Gordon, WJ Tomlinson, and Hermann A Haus. Raman response function of silica-core fibers. *JOSA B*, 6(6):1159–1166, 1989.

[46] J. Russell. Report on waves. in report of the 14th meeting of the british association for the advancement of science. Plates XLIIILVII:311390, 1845.

[47] Clifford S. Gardner, John M. Greene, Martin D. Kruskal, and Robert M. Miura. Method for solving the korteweg-devries equation. *Phys. Rev. Lett.*, 19:1095–1097, Nov 1967.

[48] James Roy Taylor. *Optical solitons: theory and experiment*, volume 10. Cambridge University Press, 1992.

[49] Govind P Agrawal. Optical pulse propagation in doped fiber amplifiers. *Physical Review A*, 44(11):7493, 1991.

[50] Leslie C Allen. *Optical Resonance and Two-Level Atoms.* Dover publications, 1975.

[51] Akira Hasegawa and Frederick Tappert. Transmission of stationary nonlinear optical pulses in dispersive dielectric fibers. i. anomalous dispersion. *Applied Physics Letters*, 23(3):142–144, 1973.

[52] Robert A Fisher and William K Bischel. Numerical studies of the interplay between self-phase modulation and dispersion for intense plane-wave laser pulses. *Journal of Applied Physics*, 46(11):4921–4934, 1975.

[53] Thiab R Taha and Mark I Ablowitz. Analytical and numerical aspects of certain nonlinear evolution equations. ii. numerical, nonlinear schrödinger equation. *Journal of Computational Physics*, 55(2):203–230, 1984.

[54] Qianshun Chang, Erhui Jia, and W Sun. Difference schemes for solving the generalized nonlinear schrödinger equation. *Journal of Computational Physics*, 148(2):397–415, 1999.

[55] Vladimir Evgen'evich Zakharov and Alexey Borisovich Shabat. A scheme for integrating the nonlinear equations of mathematical physics by the method of the inverse scattering problem. i. *Functional analysis and its applications*, 8(3):226–235, 1974.

[56] R. C. Sharp, D. E. Spock, N. Pan, and J. Elliot. 190-fs passively mode-locked thulium fiber laser with a low threshold. *Opt. Lett.*, 21(12):881–883, Jun 1996.

[57] M. A. Solodyankin, E. D. Obraztsova, A. S. Lobach, A. I. Chernov, A. V. Tausenev, V. I. Konov, and E. M. Dianov. Mode-locked 1.93μm thulium fiber laser with a carbon nanotube absorber. *Optics Letters*, 33:1336–1338, 2008.

[58] K. Kieu and F. W. Wise. Soliton thulium-doped fiber laser with carbon nanotube saturable absorber. *IEEE Photonics Technology Letters*, 21:128–130, 2009.

[59] K. Tamura, E. P. Ippen, H. A. Haus, and L. E. Nelson. 77-fs pulse generation from a stretched-pulse mode-locked all-fiberring laser. *Opt. Lett.*, 18(13):1080–1082, Jul 1993.

[60] Axel Ruehl, Vincent Kuhn, Dieter Wandt, and Dietmar Kracht. Normal dispersion erbium-doped fiber laser with pulse energies above 10 nj. *Optics Express*, 16(5):3130–3135, 2008.

[61] H Lim, FÖ Ilday, and FW Wise. Generation of 2-nj pulses from a femtosecond ytterbium fiber laser. *Optics letters*, 28(8):660–662, 2003.

[62] Andy Chong, Joel Buckley, Will Renninger, and Frank Wise. All-normal-dispersion femtosecond fiber laser. *Opt. Express*, 14(21):10095–10100, 2006.

[63] R Mossadegh, JS Sanghera, D Schaafsma, BJ Cole, VQ Nguyen, RE Miklos, and ID Aggarwal. Fabrication of single-mode chalcogenide optical fiber. *Lightwave Technology, Journal of*, 16(2):214–217, 1998.

[64] Scott Diddams and Jean-Claude Diels. Dispersion measurements with white-light interferometry. *JOSA B*, 13(6):1120–1129, 1996.

[65] Qinghao Ye, Chris Xu, Xiang Liu, Wayne H. Knox, Man F. Yan, Robert S. Windeler, and Benjamin Eggleton. Dispersion measurement of tapered air-silica microstructure fiber by white-light interferometry. *Appl. Opt.*, 41(22):4467–4470, Aug 2002.

[66] SMJ Kelly. Characteristic sideband instability of periodically amplified average soliton. *Electronics Letters*, 28(8):806–807, 1992.

[67] H. Haus, J.G. Fujimoto, and E.P. Ippen. Analytic theory of additive pulse and kerr lens mode locking. *Quantum Electronics, IEEE Journal of*, 28(10):2086–2096, 1992.

[68] M. Horowitz, Y. Barad, and Y. Silberberg. Noiselike pulses with a broadband spectrum generated from an erbium-doped fiber laser. *Opt. Lett.*, 22(11):799–801, Jun 1997.

[69] D. Tang, L. Zhao, and B. Zhao. Soliton collapse and bunched noise-like pulse generation in a passively mode-locked fiber ring laser. *Opt. Express*, 13(7):2289–2294, Apr 2005.

[70] LE Nelson, DJ Jones, K Tamura, HA Haus, and EP Ippen. Ultrashort-pulse fiber ring lasers. *Applied Physics B: Lasers and Optics*, 65(2):277–294, 1997.

[71] M. Hofer, M. E. Fermann, F. Haberl, M. H. Ober, and A. J. Schmidt. Mode locking with cross-phase and self-phase modulation. *Opt. Lett.*, 16(7):502–504, Apr 1991.

[72] Eugene Hecht. Optics 4th edition. *Optics 4th edition by Eugene Hecht Reading, MA: Addison-Wesley Publishing Company, 2001*, 1, 2001.

[73] U. Keller, K.J. Weingarten, F.X. Kartner, D. Kopf, B. Braun, I.D. Jung, R. Fluck, C. Honninger, N. Matuschek, and J. Aus der Au. Semiconductor saturable absorber mirrors (sesam's) for femtosecond to nanosecond pulse generation in solid-state lasers. *Selected Topics in Quantum Electronics, IEEE Journal of*, 2(3):435–453, 1996.

[74] S.Y. Set, H. Yaguchi, Y. Tanaka, and M. Jablonski. Laser mode locking using a saturable absorber incorporating carbon nanotubes. *Lightwave Technology, Journal of*, 22(1):51 – 56, jan. 2004.

[75] MN Cizmeciyan, JW Kim, S Bae, BH Hong, F Rotermund, and A Sennaroglu. Graphene mode-locked femtosecond cr: Znse laser at 2500 nm. *Optics letters*, 38(3):341–343, 2013.

[76] Samuli Kivistö, Tommi Hakulinen, Antti Kaskela, Brad Aitchison, David P Brown, Albert G Nasibulin, Esko I Kauppinen, Antti Härkönen, and Oleg G Okhotnikov. Carbon nanotube films for ultrafast broadband technology. *Opt. Express*, 17(4):2358–2363, 2009.

[77] Zhipei Sun, Tawfique Hasan, Felice Torrisi, Daniel Popa, Giulia Privitera, Fengqiu Wang, Francesco Bonaccorso, Denis M Basko, and Andrea C Ferrari. Graphene mode-locked ultrafast laser. *Acs Nano*, 4(2):803–810, 2010.

[78] Jaroslaw Sotor, Grzegorz Sobon, Iwona Pasternak, Aleksandra Krajewska, Wlodek Strupinski, and Krzysztof M Abramski. Simultaneous mode-locking at 1565 nm and 1944 nm in fiber laser based on common graphene saturable absorber. *Optics express*, 21(16):18994–19002, 2013.

[79] Riichiro Saito Gene Dresselhaus Ado Jorio, Mildred S. Dresselhaus. *Raman Spectroscopy in Graphene Related Systems*. Wiley-VCH, 2011.

[80] P. R. Wallace. The band theory of graphite. *Phys. Rev.*, 71:622–634, May 1947.

[81] Gordon W Semenoff. Condensed-matter simulation of a three-dimensional anomaly. *Physical Review Letters*, 53(26):2449–2452, 1984.

[82] David Carey. Carbon based electronic. *Journal of Materials Science: Materials in Electronics*, 17(6):397–398, 2006.

[83] K. S. Novoselov, A. K. Geim, S. V. Morozov, D. Jiang, Y. Zhang, S. V. Dubonos, I. V. Grigorieva, and A. A. Firsov. Electric field effect in atomically thin carbon films. *Science*, 306(5696):666–669, 2004.

[84] Guichuan Xing, Hongchen Guo, Xinhai Zhang, Tze Chien Sum, and Cheng Hon Alfred Huan. The physics of ultrafast saturable absorption in graphene. *Opt. Express*, 18(5):4564–4573, 2010.

[85] Francesco Bonaccorso, Z Sun, T Hasan, and AC Ferrari. Graphene photonics and optoelectronics. *Nature Photonics*, 4(9):611–622, 2010.

[86] R. R. Nair, P. Blake, A. N. Grigorenko, K. S. Novoselov, T. J. Booth, T. Stauber, N. M. R. Peres, and A. K. Geim. Fine structure constant defines visual transparency of graphene. *Science*, 320(5881):1308, 2008.

[87] Yu Wang Zhenhua Ni Yongli Yan Ze Xiang Shen Kian Ping Loh Ding Yuan Tang Qiaoliang Bao, Han Zhang. Atomic-layer graphene as a saturable absorber for ultrafast pulsed lasers. *Advanced Functional Materials*, 19:30773083, 2009.

[88] Gunnar Moos, Cornelius Gahl, Roman Fasel, Martin Wolf, and Tobias Hertel. Anisotropy of quasiparticle lifetimes and the role of disorder in graphite from ultrafast time-resolved photoemission spectroscopy. *Phys. Rev. Lett.*, 87:267402, Dec 2001.

[89] Tobias Kampfrath, Luca Perfetti, Florian Schapper, Christian Frischkorn, and Martin Wolf. Strongly coupled optical phonons in the ultrafast dynamics of the electronic energy and current relaxation in graphite. *Phys. Rev. Lett.*, 95:187403, Oct 2005.

[90] Paul A. George, Jared Strait, Jahan Dawlaty, Shriram Shivaraman, Mvs Chandrashekhar, Farhan Rana, and Michael G. Spencer. Ultrafast optical-pump terahertz-probe spectroscopy of the carrier relaxation and recombination dynamics in epitaxial graphene. *Nano Letters*, 8(12):4248–4251, 2008.

[91] Dong Sun, Zong-Kwei Wu, Charles Divin, Xuebin Li, Claire Berger, Walt A. de Heer, Phillip N. First, and Theodore B. Norris. Ultrafast relaxation of excited dirac fermions in epitaxial graphene using optical differential transmission spectroscopy. *Phys. Rev. Lett.*, 101:157402, Oct 2008.

[92] Jahan M. Dawlaty, Shriram Shivaraman, Mvs Chandrashekhar, Farhan Rana, and Michael G. Spencer. Measurement of ultrafast carrier dynamics in epitaxial graphene. *Applied Physics Letters*, 92(4):042116, 2008.

[93] Robert N. Zitter. Saturated optical absorption through band filling in semiconductors. *Appl. Phys. Lett.*, 14:73, 1969.

[94] Prakash R. Somani, Savita P. Somani, and Masayoshi Umeno. Planer nano-graphenes from camphor by CVD. *Chemical Physics Letters*, 430(1):56 – 59, 2006.

[95] Mustafa Lotya, Paul J King, Umar Khan, Sukanta De, and Jonathan N Coleman. High-concentration, surfactant-stabilized graphene dispersions. *ACS Nano*, 4(6):3155–3162, 2010.

[96] Amos Martinez, Kazuyuki Fuse, Bo Xu, and Shinji Yamashita. Optical deposition of graphene and carbon nanotubes in a fiber ferrule for passive mode-locked lasing. *Opt. Express*, 18(22):23054–23061, Oct 2010.

[97] Sumio Iijima. Helical microtubules of graphitic carbon. *Nature*, 354:56 – 58, 1991.

[98] Sumio Iijima and Toshinari Ichihashi. Single-shell carbon nanotubes of 1-nm diameter. *Nature*, 363:603 – 605, 1993.

[99] Andreas Schmidt, Simon Rivier, Won Bae Cho, Jong Hyuk Yim, Sun Young Choi, Soonil Lee, Fabian Rotermund, Daniel Rytz, Günter Steinmeyer, Valentin Petrov, et al. Sub-100 fs single-walled carbon nanotube saturable absorber mode-locked yb-laser operation near 1 μm. *Optics Express*, 17(22):20109–20116, 2009.

[100] Aleksey G Rozhin, Youichi Sakakibara, Shu Namiki, Madoka Tokumoto, Hiromichi Kataura, and Yohji Achiba. Sub-200-fs pulsed erbium-doped fiber laser using a carbon nanotube-polyvinylalcohol mode locker. *Applied physics letters*, 88(5):051118–051118, 2006.

[101] Z. Sun, T. Hasan, and A.C. Ferrari. Ultrafast lasers mode-locked by nanotubes and graphene. *Physica E: Low-dimensional Systems and Nanostructures*, 44(6):1082 – 1091, 2012.

[102] Z. Sun, A. G. Rozhin, F. Wang, T. Hasan, D. Popa, W. O'Neill, and A. C. Ferrari. A compact, high power, ultrafast laser mode-locked by carbon nanotubes. *Applied Physics Letters*, 95(25):253102, 2009.

[103] K. Kieu and F. W. Wise. All-fiber normal-dispersion femtosecond laser. *Opt. Express*, 16(15):11453–11458, Jul 2008.

[104] Phaedon Avouris and Jia Chen. Nanotube electronics and optoelectronics. *Materials Today*, 9(10):46 – 54, 2006.

[105] Philip G Collins and Phaedon Avouris. Nanotubes for electronics. *Scientific American*, 283(6):62–69, 2000.

[106] S. Maruyama. Shigeo maruyama's fullerene and carbon nanotube site.

[107] H. Kataura, Y. Kumazawa, Y. Maniwa, I. Umezu, S. Suzuki, Y. Ohtsuka, and Y. Achiba. Optical properties of single-wall carbon nanotubes. *Synthetic Metals*, 103(1):2555 – 2558, 1999. ¡ce:title¿International Conference on Science and Technology of Synthetic Metals¡/ce:title¿.

[108] Yoichi Murakami, Shohei Chiashi, Yuhei Miyauchi, Minghui Hu, Masaru Ogura, Tatsuya Okubo, and Shigeo Maruyama. Growth of vertically aligned single-walled carbon nanotube films on quartz substrates and their optical anisotropy. *Chemical Physics Letters*, 385(3):298–303, 2004.

[109] Jean-Sébastien Lauret, Christophe Voisin, Guillaume Cassabois, Claude Delalande, Ph Roussignol, Oliver Jost, and L Capes. Ultrafast carrier dynamics in single-wall carbon nanotubes. *Physical review letters*, 90(5):057404, 2003.

[110] Regina Gumenyuk, Ismo Vartiainen, Hemmo Tuovinen, and Oleg G. Okhotnikov. Dissipative dispersion-managed soliton 2μm thulium/holmium fiber laser. *Opt. Lett.*, 36(5):609–611, Mar 2011.

[111] Frithjof Haxsen, Dieter Wandt, Uwe Morgner, Jörg Neumann, and Dietmar Kracht. Monotonically chirped pulse evolution in an ultrashort pulse thulium-doped fiber laser. *Opt. Lett.*, 37(6):1014–1016, Mar 2012.

[112] Leiran Wang, Xueming Liu, Yongkang Gong, Dong Mao, and Lina Duan. Observations of four types of pulses in a fiber laser with large net-normal dispersion. *Opt. Express*, 19(8):7616–7624, Apr 2011.

[113] S.Y. Set, Hiroshi Yaguchi, Y. Tanaka, and M. Jablonski. Ultrafast fiber pulsed lasers incorporating carbon nanotubes. *Selected Topics in Quantum Electronics, IEEE Journal of*, 10(1):137–146, 2004.

[114] Y.-C. Chen, N. R. Raravikar, L. S. Schadler, P. M. Ajayan, Y.-P. Zhao, T.-M. Lu, G.-C. Wang, and X.-C. Zhang. Ultrafast optical switching properties of single-wall carbon nanotube polymer composites at 1.55μm. *Applied Physics Letters*, 81(6):975–977, 2002.

[115] Y. Sato I. Iwasa M. Tian H. Mitsu S. Tatsuura, M. Furuki. Semiconductor carbon nanotubes as ultrafast switching materials for optical telecommunications. *Advanced Materials*, 15:534–537, 2003.

[116] E. Garmire. Resonant optical nonlinearities in semiconductors. *Selected Topics in Quantum Electronics, IEEE Journal of*, 6(6):1094–1110, 2000.

[117] Xiuquan Ma, Cheng Zhu, M. Rever, and Shenghong Huang. Large core single-mode chirally-coupled-core fibers for high power fiber lasers. In *Optical Communication, 2009. ECOC '09. 35th European Conference on*, pages 1–1, 2009.

[118] Simon Lefrancois, Chi-Hung Liu, Michelle L. Stock, Thomas S. Sosnowski, Almantas Galvanauskas, and Frank W. Wise. High-energy similariton fiber laser using chirally coupled core fiber. *Opt. Lett.*, 38(1):43–45, Jan 2013.

[119] Simon Lefrancois, Thomas S. Sosnowski, Chi-Hung Liu, Almantas Galvanauskas, and Frank W. Wise. Energy scaling of mode-locked fiber lasers with chirally-coupled core fiber. *Opt. Express*, 19(4):3464–3470, Feb 2011.